Title
Aging Mechanisms of Series-Connected Li-Ion Battery Packs due to Temperature Gradients

Author
Lacap, Joseph Henry

Publication Date
2021

Peer reviewed|Thesis/dissertation

Aging Mechanisms of Series-Connected Li-Ion Battery Packs due to Temperature Gradients

By

JOSEPH HENRY LACAP

DISSERTATION

Submitted in partial satisfaction of the requirements for the degree of

DOCTOR OF PHILOSOPHY

in

Mechanical and Aerospace Engineering

in the

OFFICE OF GRADUATE STUDIES

of the

UNIVERSITY OF CALIFORNIA

DAVIS

Approved:

Jae Wan Park, Chair

Bryan Jenkins

Paul Erickson

Committee in Charge

2021

ACKNOWLEDGMENT

Thanks go to Matt Klein for constructing the original version of the temperature gradient system and to Prof. Jae Wan Park for advising this work and assisting with interpretation of the final data. Of course thanks also go to my family who were incredibly supportive during my time spent working on research. In addition, the California Energy Commission's funding of my work at UC Davis related to second-life batteries was crucial in my ability to continue my studies.

ABSTRACT

The goal of this research was to determine how temperature gradients in series-connected lithium-ion battery packs affect the performance and cycle-life degradation of each of the cells in the battery pack as well as the pack as a whole. This degradation was compared to cells cycled individually and cells subjected only to calendar aging. This allowed attribution of degradation rates to specific usage conditions. Cell performance and capacity degradation was measured by utilizing standard capacity and resistance checks, neutron radiography, and other battery performance metrics. It was found that cells subjected to non-uniform temperatures within the pack degraded faster, and battery pack capacity was reduced relative to an ideal battery pack. It was also determined that the hottest cell in a series connected pack with a temperature gradient will degrade faster than an equivalent cell cycled individually at the same temperature.

Despite the presence of large battery packs in modern electric vehicles, little work has been done to verify pack performance and degradation models, especially when paired with non-uniform pack temperature. This was due to the interwoven degradation stressors and mechanisms at play that need to be separately investigated to gain a full understanding of the combined effect of series packs and temperature gradients. In this work, the effects of calendar aging, cycling aging, temperature, and temperature gradients were all measured and compared. The causes of increased degradation measured on the packs with an applied temperature gradient were determined to be the superimposed effects of varying depths of discharge and non-uniform current distributions within the cells. It was also found that cell degradation did not scale linearly with applied temperature gradient. Rather, the relative rate of aging was found to follow a second order polynomial in temperature and in temperature difference. This meant that depending on the pack average temperature, the hottest or the coldest cell can degrade the most. This behavior was quantified to allow for use in optimizing the design of battery thermal management systems, and an example analysis of thermal management performance was performed on a battery pack from a Nissan Leaf.

CONTENTS

List of Figures

List of Tables

NOMENCLATURE

BMS Battery Management System

C, C-rate Relative of charge or discharge of a battery relative to its capacity in Ah, where 1C discharges the battery in 1 hour.

CAISO California Independent System Operator

DCIR, 0.1s IR Direct Current Internal Resistance, measured after 0.1s current pulse.

DMC Dimethyl Carbonate, $C_3H_6O_3$. Electrolyte solution component.

DoD Depth of Discharge

EC Ethylene Carbonate, $C_3H_4O_3$. Electrolyte solution component.

EIS Electrochemical Impedance Spectroscopy

EV Electric Vehicle

HPPC Hybrid Pulse Power Characterization

IR Internal Resistance

LFP $LiFePO_4$ battery chemistry

LIB Lithium-Ion Battery

NN Neural Network

NMC Lithium-Nickel-Manganese-Cobalt-Oxide battery chemistry

NR Neutron Radiography

OCV Open Circuit Voltage

SEI Solid-Electrolyte Interface

SoC State of Charge, % of cell's capacity that is available for discharge.

SoH State of Health, the cell's current capacity divided by its original capacity.

TG1 / TG2 / TG Pack 1 / TG Pack 2 References to the battery packs with applied temperature distributions.

TGS Temperature Gradient System, the experimental fixture used to generate temperature distributions in battery packs and measure the resulting effects.

Part I

INTRODUCTION

Lithium ion batteries (LIBs) are an increasingly important part of personal devices, cars, and the electrical grid. This is due to their relatively high energy density compared to other energy storage technologies, their continually reducing costs, the push for more renewable sources of electricity, and increasing demand for electric vehicles. World-wide demand for lithium-ion batteries is expected to increase from 100 GWh in 2019 to 1300 GWh by 2030 [21]. The prevalence of LIBs also raises some concerns: They are still expensive compared to energy production, degradation means that they will eventually need to be replaced after an unknown, highly variable, and application-specific period of time, and they are difficult to recycle.

In an attempt to predict the lifetime of products such as electric vehicles, companies invest in extensive modeling and accelerated aging testing of the batteries to be used. This information allows them to create warranty terms, expected maintenance costs, the required number of spare parts to be produced, etc. However, many battery models apply uniform temperatures to an entire battery pack, then model the temperature of each cell but do not model the transfer of heat between adjacent cells [22–24]. Likewise, battery accelerated aging tests are typically conducted at high temperatures and high cycle rates to reduce the time these tests take [25]. While this does age the battery more quickly and can be used to help predict lifetime [26], it may also result in different aging mechanisms than seen during "real" operation.

For example, some electric vehicles lack thermal management systems for their battery packs (such as the Nissan Leaf). Despite the (presumably) extensive testing Nissan conducted to reach the conclusion that Nissan LEAF batteries should last 7 years before losing 30% of their capacity, drivers in Arizona found that the battery degraded that much in just one year. [27] While newer models have an adjusted battery chemistry that better deals with warmer temperatures [28], this incident illustrates the need for improved understanding of lithium-ion battery degradation.

One little-studied aging factor is the non-uniform temperature that develops across a lithium ion battery pack [15,29,30]. Some work has been done on this for cells connected in parallel [17,31,32], but electric vehicle battery packs primarily consist of cells connected in series (with a few notable exceptions such as Tesla) and little work has been done to explore this front [33]. By understanding the effect of non-uniform temperature on degradation, battery pack production and design and testing costs can be reduced, and lifetime extended. Thus, this work aims to address one cause, of two major problems with lithium-ion batteries, cost and lifetime.

1 Background

1.1 Lithium-Ion Batteries

Lithium-ion batteries are electrochemical cells made with carbon (typically graphite) for the anode active material and lithium metal oxide or phosphate for the cathode. The cell electrodes are formed by coating both sides of the current collectors with a slurry containing fine particles of the active material mixed with a binder [34]. Copper is used for the anode current collector, while aluminum is used for the cathode. The thickness of the active material coating on the current collectors varies by cell design, but is on the order of $50\mu m$ [8]. The electrodes are then attached to either side of a polyethylene/polypropylene separator that allows the transfer of Li^+, but not electrons [35]. This forms a single layer of the battery cell, which is then soaked in an electrolyte made of lithium salts dissolved in an organic solvent. A diagram showing the cell structure is shown in Figure 13. This layered assembly is then rolled or cut into the form of the cell and placed in a sealed container to form the final cell assembly.

Lithium-ion batteries come in three primary form factors: there are cylindrical cells, pouch cells, and prismatic cells. LIBs also come in 'watch battery' (coin or button cell) form, but these cells have a much more limited applicability than the other three types of cells. Each form factor is constructed in a slightly different way, but all start with a flat 'sandwich' of cell layers, for example: separator, LFP cathode, aluminum current collector, LFP cathode, separator, carbon anode, copper current collector, carbon anode. For a cylindrical cell, this is then wound in a spiral and inserted into a metal can. For a prismatic cell, the layers are wound similarly to a cylindrical

cell, but then compressed in one direction to flatten out the 'jellyroll'. This is then inserted into a rectangular can. For pouch cells, the cell material can be cut into strips and layered on top of each other, or constructed in the same way as the prismatic cells. The jellyroll is then sealed inside a pouch [36]. Each cell type has its advantages and disadvantages and may be chosen for a specific application for various reasons including price, safety, ease of use, thermal properties, and of course size.

Cylindrical cells are made by taking the layered battery materials and rolling them around a core before inserting the resulting jellyroll into a canister. Similarly, prismatic cells are made by rolling the cell around a flat sheet of (e.g.) nylon [37] to form an elliptical jellyroll that is then encased in the cell can. Pouch cells are constructed by layering multiple stacks of cells, then connecting the layers in parallel and wrapping the assembly in the aluminum foil pouch [38].

While charging the battery, electrons are forced out of the cathode which then frees the Li^+ ion from the reaction sites. The electron travels through the external charger because it cannot penetrate the separator, then into the anode. Simultaneously, the freed Li^+ ions migrate through the electrolyte and diffuses through the separator into the anode. When the Li^+ ion enters the anode, it regains an electron (that passed through the external circuit), reducing it and locking the atomic lithium into the electrode's structure [9]. During discharge, the opposite process occurs, except that the electrons now perform work in the external circuit instead of being forced into the anode [39]. The process of Li^+ ions entering and exiting the latices structures is called intercalation and deintercalation respectively.

The cathode materials of LIBs are made of crystalline structured materials with lattice spacing such that Li^+ ions can be bound in the structure (Figure 12) [40]. The anode has a layered honeycomb structure resulting from the carbon-carbon bonds. The layered carbon structures form crystallites held together by the Van der Waals force. The weak nature of the binding of the layers means the structure of the carbon anodes can be easily adjusted (or damaged) to change the charge/discharge characteristics [41]. For LFP, common particle sizes are 50 to 1000 nm [40], and for the carbon anode particle sizes are 4-20μm [42–44]

The choice of electrolyte is critical to the performance of a LIB. The electrolyte solution must be chosen such that it remains electrochemically stable over the entire operational voltage of the cell, has a long lifetime, high ionic conductivity, and exists as a liquid at temperatures the battery would be exposed to [9]. The electrolyte's decomposition at high temperatures is also a major contributor to thermal runaway of LIBs [45], making electrolyte selection a battery safety consideration as well. The electrolyte is primarily composed of a lithium salt and a mixture of organic solvents, typically with some additives used to adjust the properties such as the viscosity [9]. Some common lithium salts used are $LiAsF_6$, $LiClO_4$, $LiBF_4$, $LiPF_6$, $Li(CF_3SO_3)$, and $LiSO_3CF_3$ [9, 46, 47].

The solvent mixture usually contains a cyclic carbonate (i.e. the molecules have a ring structure), either propylene carbonate (PC, $C_4H_6O_3$) or more commonly ethylene carbonate (EC, $C_3H_4O_3$) [9, 41]. These are used due to their high polarity and dielectric constants which allow them to easily dissolve the lithium salts [9], however they also have a high viscosity which reduces the ionic conductivity of the electrolyte [35]. Therefore, these are mixed with at least one of a number of linear carbonates (i.e. the molecules have a linear structure) such as dimethyl carbonate (DMC, $C_3H_6O_3$), Diethyl carbonate (DEC, $C_5H_10O_3$), or Ethyl-methyl carbonate (EMC, $C_4H_8O_3$). These linear carbonates have lower viscosity, so when mixed with a cyclic carbonate, the result is a balanced electrolyte solvent [9, 35]. In addition to the solvents, various additives can be included in the electrolyte to adjust solid-electrolyte interface layer reactions, improve compatibility with the cathode material, and improve safety among other uses [41, 48].

A critical function of a good electrolyte for a lithium battery is its ability to form a stable solid-electrolyte interface (SEI) layer [8, 35]. This is because the carbon/graphite anode is unstable in direct contact with most electrolyte solutions, resulting in unwanted side reactions and physical damage (exfoliation) to the structure of the anode from co-intercalation of the electrolyte with the Li^+ ions [46]. The SEI is a passivation layer that forms on the surface of the anode as a result of irreversible reduction of the electrolyte [35]. In order to prevent complete conversion of the electrolyte by reduction at the anode, the reduction products should be stable such that they prevent further reactions between the anode and electrolyte. In addition, the SEI must be

as conductive as possible of Li ions to allow the battery to function. Unfortunately, DEC, DMC, and PC do not form stable SEI layers [9, 49], but EC does [35]. Some of the common reactions resulting in the formation of the SEI are [33, 49]:

$$
\begin{gathered}
2EC + 2e^- + 2Li^+ \rightarrow (CH_2OCO_2Li)_2 \downarrow + CH_2 \quad or \quad Li_2CO_3 \downarrow + C_2G_4 \uparrow \\
DMC + e^- + Li^+ \rightarrow CH_3 \cdot CH_3OCO_2L \downarrow \quad or \quad CH_3OLi \downarrow + CH_3OCO \\
DMC + 2e^- + 2Li^+ \rightarrow Li_2CO_3 \downarrow + C_2H_6 \uparrow PF_6^- + ne^- + nLi^+ \rightarrow LiF + 2HF \downarrow + Li_xPF_y \downarrow \\
EMC + e^- + Li^+ \rightarrow LiOCOH_3 + CH_3CH_2OLi \\
PC + 2e^- + 2Li^+ \rightarrow CH_3CH(OCO_2Li)CH_2OCO_2Li + Li_2CO_3 \downarrow + C_3H_6 \uparrow
\end{gathered}
\tag{1}
$$

SEI formation can be easily visualized using Figure 1. The dark green area shows the window of stability of the electrolyte. On the right, the anode's nominal potential is shown and on the left the cathode's. When charging potential is applied to the cell, the anode's potential is lowered, making the electrolyte unstable and causing the reduction reactions [1] shown in Equation 1. Once the initial layer of SEI is formed, further but slower reactions occur that are aggravated by increased temperature and charging at low temperature. These effects are shown in Figure 13 along with the progression of SEI layer growth on the anode and how these changes affect the cell's internal resistance and capacity.

There are many different chemistries of LIBs, and they are designated based on the material used to form the cathode. Some of the more common cathode materials include NMC (Eq. 2) ($LiNi_{1/3}Mn_{1/3}Co_{1/3}O_2$), NCA (Eq. 3) ($LiNiCoAlO_2$), LMO (Eq. 4) ($LiMn_2O_4$), LCO (Eq. 5) ($LiCoO_2$), and LFP (Eq. 6) ($LiFePO_4$) [36, 39, 50]. The redox reaction pairs for each cell chemistry are listed below in the charging direction [9]:

$$
\begin{gathered}
LiNi_{1/3}Mn_{1/3}Co_{1/3}O_2 \rightarrow Ni_{1/3}Mn_{1/3}Co_{1/3}O_2 + Li^+ + e^- \quad (cathode) \\
C_6 + Li^+ + e^- \rightarrow LiC_6 \quad (andoe)
\end{gathered}
\tag{2}
$$

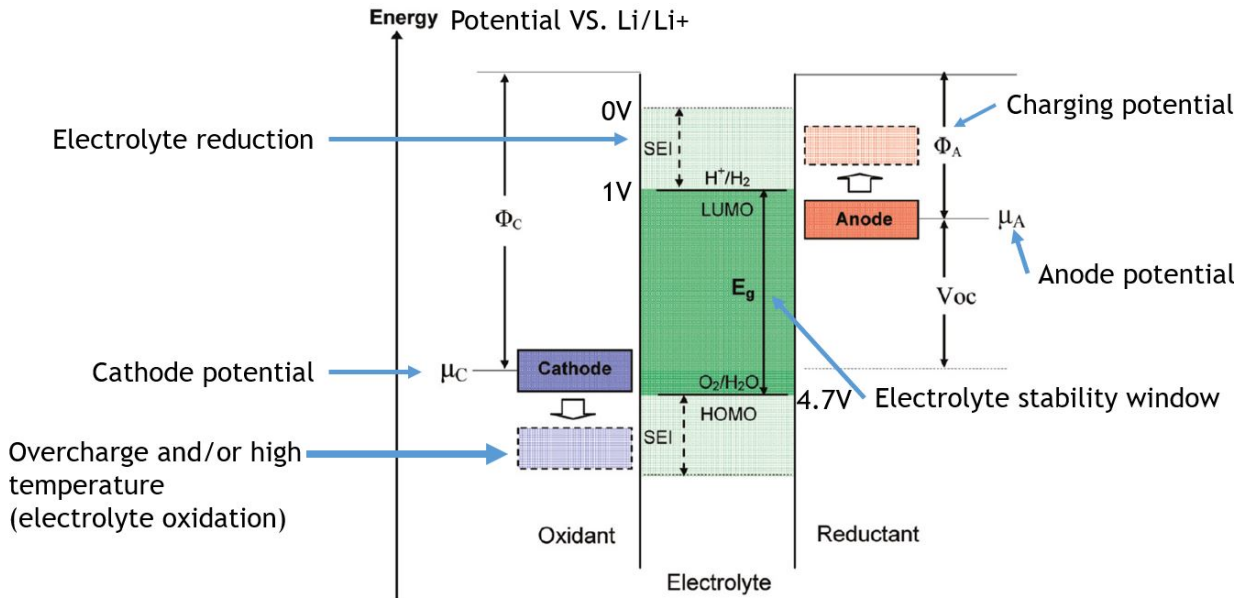

FIGURE 1. Figure showing the potential stability window for the electrolyte and how it changes as a result of applying charging potential to the cell. Adapted from An et. al. [1].

$$\begin{aligned} LiNiCoAlO_2 &\rightarrow NiCoAlO_2 + Li^+ + e^- \quad (cathode) \\ C_6 + Li^+ + e^- &\rightarrow LiC_6 \quad (andoe) \end{aligned} \tag{3}$$

$$\begin{aligned} LiMn_2O_4 &\rightarrow Mn_2O_4 + Li^+ + e^- \quad (cathode) \\ C_6 + Li^+ + e^- &\rightarrow LiC_6 \quad (andoe) \end{aligned} \tag{4}$$

$$\begin{aligned} LiCoO_2 &\rightarrow CoO_2 + Li^+ + e^- \quad (cathode) \\ C_6 + Li^+ + e^- &\rightarrow LiC_6 \quad (andoe) \end{aligned} \tag{5}$$

$$\begin{aligned} LiFePO_4 &\rightarrow FePO_4 + Li^+ + e^- \quad (cathode) \\ C_6 + Li^+ + e^- &\rightarrow LiC_6 \quad (andoe) \end{aligned} \tag{6}$$

Each cell chemistry has its advantages and disadvantages in terms of their cost, energy density, power capability, safety, etc. For this work, cells made with LFP cathodes were considered. While not common in automotive applications [50], it is one of the most common chemistries and often used in stationary storage systems [51–53] due to its higher safety (higher thermal runaway initiation temperature) [54]. LFP cells were also chosen to make data gathered directly comparable to work done by Klein [17, 31] using the same experimental setup.

The voltage of a lithium-ion battery can be calculated by looking at redox reaction potential tables. These potentials are typically measured relative to the standard hydrogen electrode [13], but LIB components are measured against a Li/Li^+ electrode. These potentials can be seen in Table 1. For example, a LIB constructed with a graphite anode and LFP cathode would be expected to have a nominal voltage of $3.45V - 0.1V = 3.35V$. From looking at datasheets for real LFP cells, we can see that the nominal voltage is 3.2V [55, 56]. The difference can be attributed to several factors, first, the data in Table 1 is collected under ideal conditions (i.e. high purity), the data is for specific products sold by Sigma-Aldrich, so slight differences in chemistry between these values and what cell manufactures used likely exist. Additionally, in order to ensure the lifetime and safety of the cells, the manufactures may specify a more limited voltage range than the material is capable of, lowering the cell's average voltage.

A more theoretical method for calculating the maximum voltage of a cell is through the Gibbs free energy, which represents the maximum possible "no loss" voltage the cell could have [13, 57]. For example, consider a LFP cell (Reaction 6). For this reaction, $LiFePO_4$ has $\Delta G_f^\circ = -1481kJ/mol$, $FePO_4$ has $\Delta G_f^\circ = -1110kJ/mol$, [58, 59] and $LiC6$ has $\Delta G_f^\circ = 11kJ/mol$ [60]. The total change in the Gibbs free energy for the reaction is then $\Delta G^\circ = -1481 + 1110 + 11 = -360kJ/mol$. We

Electrode Material	**Potential (V vs. Li/Li^+)**	**Specific Capacity (mAh/g)**	**Use**
$LiCoO_2$	3.9	140	Cathode
$LiNi_{0.8}Co_{0.15}Al_{0.05}O_2$	3.8	180-200	Cathode
$LiNi_{1/3}Mn_{1/3}Co_{1/3}O_2$	3.8	160-170	Cathode
$LiMn_2O_4$	4.1	100-120	Cathode
$LiFePO_4$	3.45	170	Cathode
Graphite	0.1	372	Anode
$Li_4Ti_5O_{12}$	1.5	175	Anode

TABLE 1. Average redox potentials and specific capacity of various anode and cathode materials [12] referenced to the $Li^+ + e^- \rightarrow Li$ reaction which has a standard (vs. $H_2/2H^+$) of -3.05V [13]

also have

$$V^\circ = -\frac{\Delta G^\circ}{nF} \tag{7}$$

Where V is the cell voltage, n is the number of electrons transferred during the reaction (1 in this case), and F is the Faraday Constant $F = 96485C/mol$. Using this equation, the calculated voltage of a LFP cell should be $V_{LiFePO_4} = 3.73V$, compared to a real cell's maximum voltage of $3.70V$ [55]. It can be seen that the theoretical voltage is slightly higher than the real voltage, for which there are a variety of reasons, many of which are affected by temperature.

The first modification to the ideal voltage is related to the change in the Gibbs free energy of a reaction due to temperature and the entropy change of the reaction:

$$\Delta G = \Delta H - T\Delta S \tag{8}$$

Where ΔH is the enthalpy change of the reaction, ΔS is the entropy change of the reaction, and T is the temperature in degrees Kelvin. Since ΔG and ΔH are negative, the effect of higher or lower temperature in terms of increasing or decreasing a cell's voltage depends on the sign of ΔS, which is positive for the SoC range of 25-100% according to [61], but for the cells considered here it was found to be from 35-100% as shown in Figure 2. Thus, increased temperature, over the majority of a LFP cell's voltage range resulted in an increased OCV [61, 62]. Figure 2 was generated from data gathered during the test described in Section 7.3.5, the results of which verified similar tests done by Klein [17] on the same (by model number) cells.

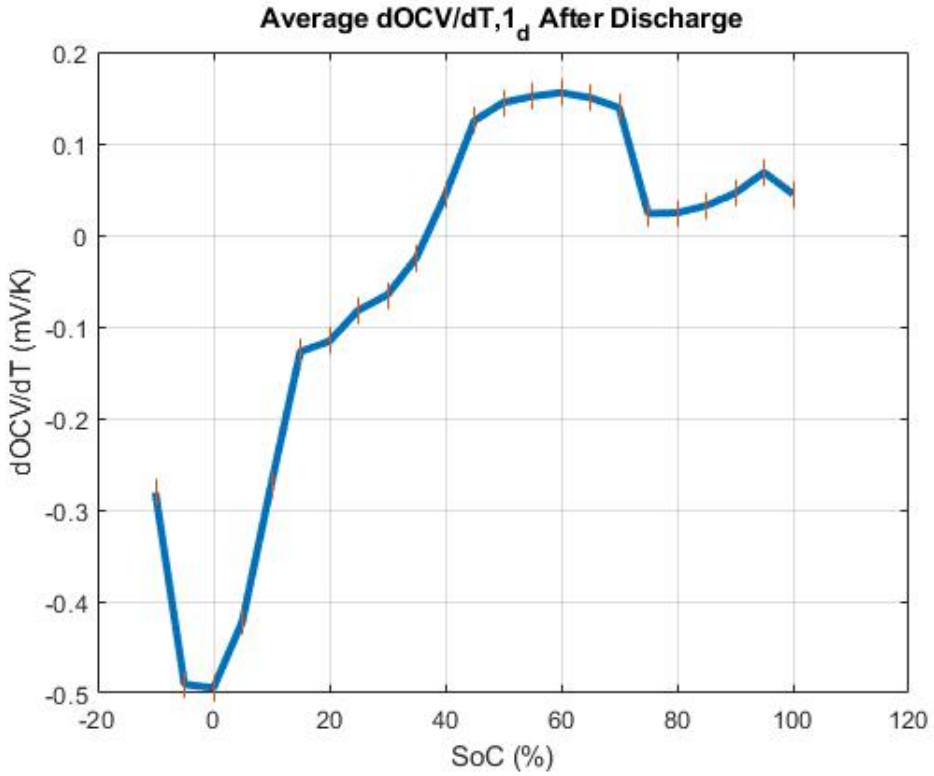

FIGURE 2. Plot showing the change in cell voltage due to temperature vs. SoC. This can be easily converted to cell entropy change using Equation 9

The entropy change of the cell can be expressed in terms of voltage by combining Equations 7 and 8 into

$$V_{OC} = -\frac{\Delta H}{F} + \frac{T\Delta S}{F} \tag{9}$$

Where V_{OC} is the cell open circuit voltage. By differentiating with respect to temperature, we can write the entropy change in terms of the cell's OCV and the temperature change of the cell.

$$\Delta S = F\frac{\partial V_{OC}}{\partial T} \tag{10}$$

The effect of reactant concentration on the Gibbs Free energy is given by

$$\Delta G = \Delta G^{\circ} - RTln(Q) \tag{11}$$

Where Q is the *reaction quotient* which describes the progress of the reaction and is equal to the reaction's equilibrium constant when equilibrium has been reached. It is defined as:

$$Q = \frac{[C]^{\gamma}[D]^{\delta}}{[A]^{\alpha}[B]^{\beta}} \quad for\ reactions\ of\ the\ form: \quad \alpha A + \beta B \leftrightarrows \gamma C + \delta D \tag{12}$$

By writing this in terms of cell voltage using eq 7, we arrive at the Nernst Equation: [13], [63].

$$V_{cell} = V_{standard} - \frac{RTln(Q)}{nF} \quad and \quad Q_{LFP} = \frac{[LiFePO_4]}{[FePO_4][Li^+]} \tag{13}$$

Where $V_{standard}$ is theoretical voltage of the reaction as calculated above, R is the ideal gas constant, T is the temperature in degrees Kelvin. According to the Nernst Equation, the open circuit voltage of the battery should be reduced at higher temperatures, but due to entropy changes, we typically see an increase in cell voltage at higher temperatures. The effect of reactant concentration is much stronger than the effect of temperature in the Nernst equation, and acts to reduce the cell's open circuit voltage especially as the cell is discharged.

The concentration of lithium in the anode or cathode, as used for calculating the reaction quotient, can also be used to calculate the SoC of the cell. This is made simpler by first normalizing the Li concentration by taking $\Theta = \frac{C_s}{C_{s,max}}$ where c_s is the concentration of Li in the electrode at any given time and $c_{s,max}$ is the maximum concentration of Li in the electrode. The SoC can then be calculated as

$$SoC = 100\% \times \frac{\Theta - \Theta_{0\%}}{\Theta_{100\%} - \Theta_{0\%}} \tag{14}$$

Where $\Theta_{0\%}$ and $\Theta_{100\%}$ are the concentrations of Li in the electrode at 0% and 100% SoC, respectively. [64] This means that in the Nernst equation, the SoC can be substituted for the concentration with the addition of a scaling factor.

While the Nernst equation describes reactant concentration losses to the open circuit voltage of a cell, temperature also changes the reaction rate, diffusivity of ion transfer, and resistance to electron flow in the battery which all change the cell's voltage while under load [62]. For this reason (and that the voltage drop can be measured as a resistance by Ohm's Law), it is common to model these effects as an effective resistance that is governed by the Arrhenius equation, [33, 65, 66], but this ignores much of the physical meaning.

$$R_{eff} = R_{ref} \exp\left(\frac{E_a}{R_{gas}}\left(\frac{1}{T} - \frac{1}{T_{ref}}\right)\right) \tag{15}$$

Where R_{ref} is the resistance of the cell at the reference temperature, T_{ref} is the reference temperature in degrees Kelvin, E_a is the activation energy of the reaction, and R_{gas} is the ideal gas constant. As can be seen, as the temperature increases, the resistance of the cell decreases.

Attempts have been made to justify the Arrhenius equation from thermodynamics. These explanations start by noting that in order for a reaction to occur, the reactants must overcome a potential barrier or activation energy (just as suggested in the Arrhenius equation), but not all molecules of the reactants have the same energy. Statistical mechanics provides the means to quantify this by considering the Maxwell Distribution that describes the three dimensional speed distribution of particles in an ideal gas [18].

$$n(\nu)d\nu = \left(\frac{N\lambda_D^3(T)m^3}{2\pi^2\hbar^3}\right)\nu^2 \exp\left(-\frac{m\nu^2}{2K_BT}\right)d\nu \tag{16}$$

Where ν is the speed of a particle, N is the number of particles λ_D is the thermal de Broglie wavelength (Eq. 17), m is the mass of the molecule(s), and T is the temperature in degrees Kelvin.

$$\lambda_D = \sqrt{\frac{2\pi\hbar^2}{mK_BT}} \tag{17}$$

This can be written in terms of the kinetic energy of the particles by substituting the definition of kinetic energy for ν and $d\nu$.

$$n(E)dE = 2N\sqrt{\frac{E}{\pi}}\left(\frac{1}{K_BT}\right)^{3/2} \exp\left(\frac{-E}{K_BT}\right)dE \tag{18}$$

Where E is the kinetic energy. As the temperature increases, the fraction of particles with higher energy increases as can be seen in Figure 3. Now, this can loosely be written as

$$n(E) = A(T) \exp\left(\frac{-E}{K_B T}\right) \tag{19}$$

Which bears a striking resemblance to the modified Arrhenius equation.

$$k = AT^n \exp\left(\frac{-E}{RT}\right) \tag{20}$$

despite the fact that the Arrhenius equation was originally empirically derived,

This is not a mathematical derivation of the Arrhenius equation, but it does illustrate the underlying physics. The Arrhenius equation was empirically derived, yet fits the form that would be expected were it properly arrived at from first principals. Part of the reason this method does not *actually* derive the Arrhenius equation is that it does not consider what fraction of the total energy each particle has is available to the reaction [56]. Additionally, the partition functions used to develop the Maxwell distribution apply to an ideal gas, so a different derivation and distribution would be involved [18].

An electrochemistry-based understanding can be gained by considering the Butler-Volmer Equation (22) which was originally developed based on phenomenological observations [57] but can be linked to physical properties of a cell as well as operating conditions such as reaction rate, temperature, and current:

$$i = \pm\, a i_0 \left(e^{\frac{\alpha n F V}{RT}} - e^{\frac{-(1-\alpha) n F V}{RT}}\right) \tag{21}$$

$$V = \frac{RT}{\alpha n F} ln\left(\frac{i}{2ai_0} + \sqrt{\left(\frac{i}{2ai_0}\right)^2 + 1}\right) \tag{22}$$

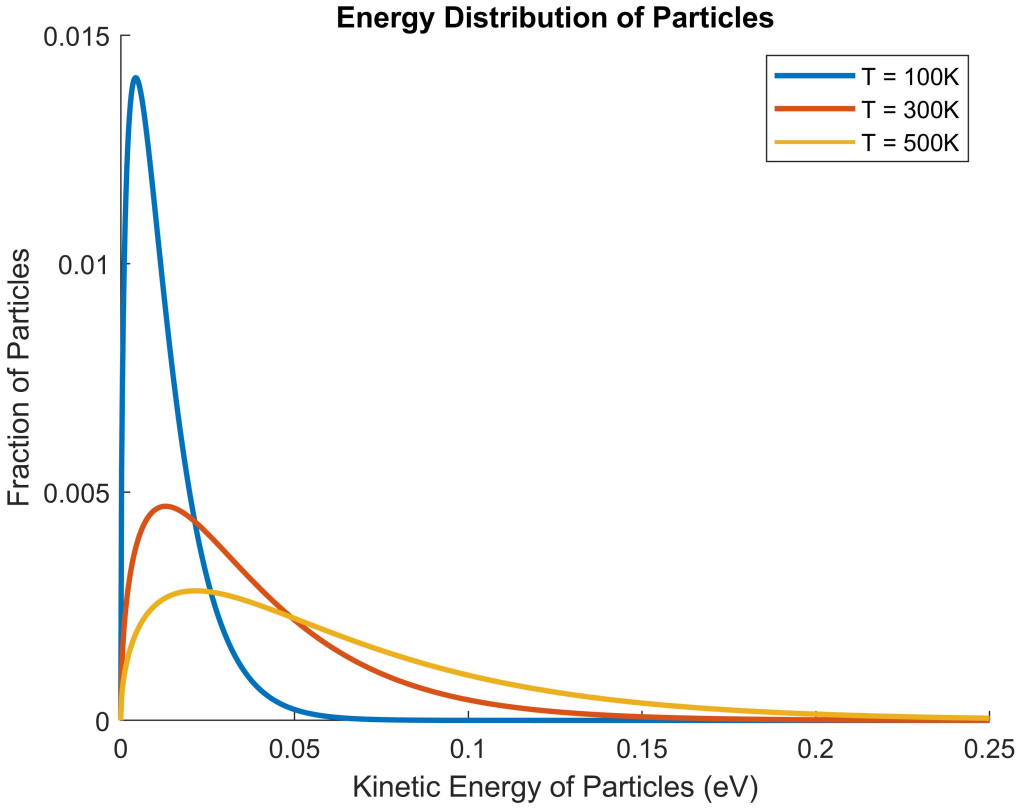

FIGURE 3. Figure showing plots of the Maxwell distribution of molecular kinetic energy at various temperatures.

Where α is the charge transfer coefficient and is $\approx \frac{1}{2}$ for LIBs [64, 67–70], i_0 is the exchange current density which is often considered to strongly depend on temperature by an Arrhenius relation [67, 68], and a is the specific electrode active surface area. It is due to changes in i_0 in the Butler-Volmer equation (22) with temperature that the voltage of a LIB is higher at higher temperatures while the cell is under load. The changes in i_0 are directly related to the reaction rate of the cell, when the reaction is slower than the current draw, the voltage drops, and when the temperature is higher, the cell's reaction rate is higher [67,70]. Some models considered expressions of the following form to describe i_0 [64, 67, 68]

$$i_0 = k_a^{\alpha}(C_{max} - C(T, SoC))^c C_e^{\alpha} C(T, SoC)^{\alpha} \tag{23}$$

The effect the Butler-Volmer equation has on the cell voltage is shown in Figure 4. The larger and more positive the value, the more of a voltage drop is caused on the cell's terminal voltage, except when the cell current is negative, in which case the voltage 'drop' is actually a voltage increase. Figure 4a shows how increasing the temperature affects the voltage when i_0 is a function of temperature but temperature is otherwise considered constant in Eq. 22. Figure 4b shows how the applied current to the cell affects the Butler-Volmer equation. Figure 4c shows how the SoC of the cell affects the Butler-Volmer voltage through i_0. Figure 4d shows how temperature affects the Butler-Volmer voltage if i_0 is not a function of temperature. By comparing Figure 4a and 4d it can be seen that i_0 is more sensitive to changes in temperature than by the temperature term in the numerator of Eq. 22.

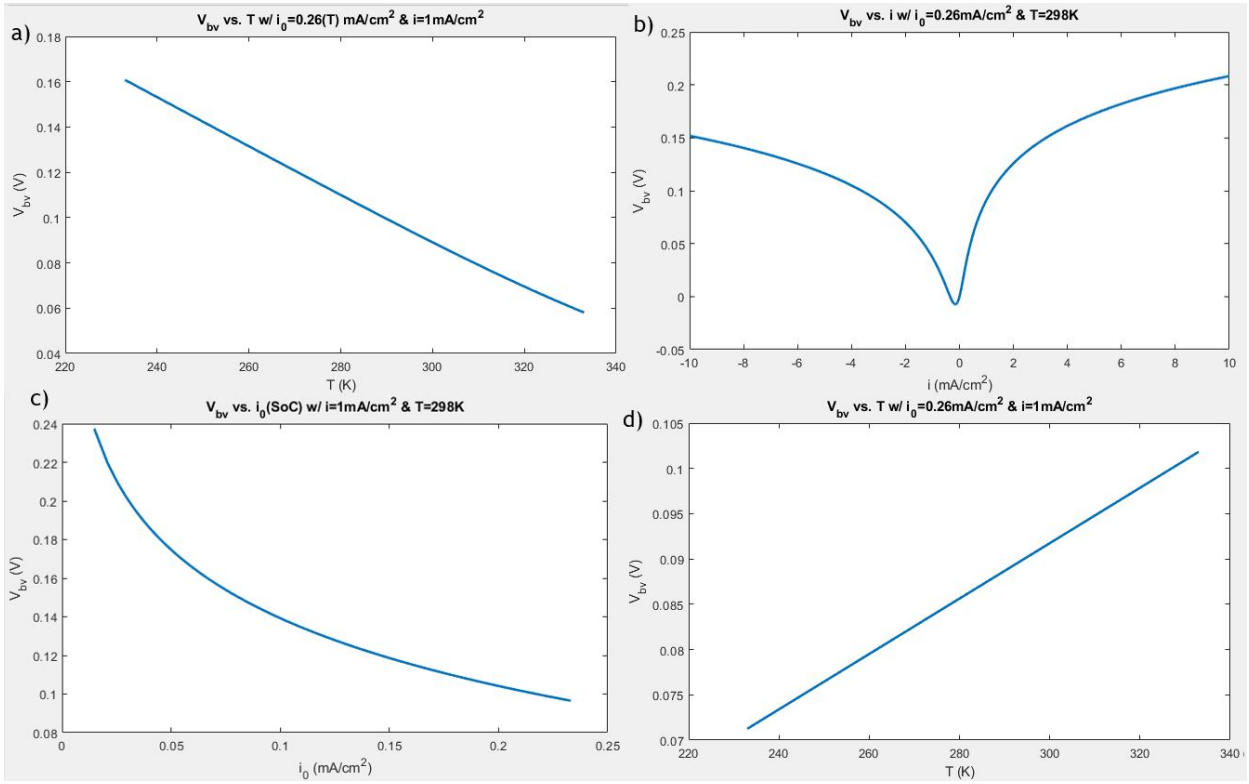

FIGURE 4. Figure showing the effect of various parameters in the Butler-Volmer equation on the potential of cell.

The end result of the effect of temperature on short-term battery performance is shown in Table 2. This table was based on data extracted from the cell datasheet [55] of the LFP cells used in the experimental section. By comparing the plots in Figure 4 to the large drop in cell capacity at low temperature observed in Table 2, it is clear that the performance impact was larger than would be suggested by the Butler-Volmer equation. This is because the Butler-Volmer equation only accounts for the charge transfer portion of the cell's overpotential, while the total overpotential, or voltage drop, is given by the sum of the contributions from the Ohmic, charge transfer, and diffusion resistances [71]

$$\eta = \eta_{\Omega} + \eta_{ct} + \eta_{diff} \tag{24}$$

where η_{Ω} is the voltage drop due to the Ohmic resistance, η_{ct} is the charge transfer overpotential, and η_{diff} is the diffusion-related overpotential.

At low temperatures, the cell becomes diffusion/mass-transfer limited, which is not accounted for in the Butler-Volmer equation [71]. Therefore, porous electrode theory must be invoked to explain these results [72]. Here, the concentration of lithium is modeled within the electrode stack of the cell

$$\epsilon \frac{\partial c_e}{\partial t} - \frac{\partial}{\partial z}\left(D_e^{eff} \frac{\partial C_e}{\partial z}\right) = ai(1 - t_+^0) \tag{25}$$

where ϵ is the volume fraction of the electrolyte, c_e is the concentration of lithium ions in the electrolyte, z is the direction perpendicular to the plane of the electrodes, D_e^{eff} is the diffusion coefficient (itself Arrhenius dependent) of the electrolyte, t_+^0 is the cation transference number, and i is the current calculated from the Butler-Volmer equation [72]. Similar expressions can be found in the literature for diffusion of lithium in the anode and cathode [23, 64, 73, 74]. Together, the

Arrhenius dependency of the diffusion coefficient and transfer resistance of the SEI layer resistance, as verified by EIS [75], accounts for the cell's reduced capacity at low temperatures [76]. It is worth noting that this reduced capacity is not permanently lost, and can be restored simply by heating the battery.

TABLE 2. Cell capacity data as a function of temperature at a C/2 discharge of the AA Power Corp. LFP 18560 cells used in this work. Data was extracted from a figure in the cell datasheet [14].

Temperature $^{\circ}C$	**Capacity (mAh)**
-40	450
-20	750
-10	1000
0	1350
10	1450
30	1550
60	1575

1.2 Vehicle Applications

One of the largest uses for LIBs is in electric vehicles, including hybrids, plug-in hybrids, and fully electric vehicles. The demand for electric vehicle battery packs is set to increase by 15x, from 100 GWh to over 1500 GWh per year, between 2019 and 2030 according to Bloomberg Businessweek [77]. This is driven by the global push to electrify transportation, with some countries such as the Netherlands banning the sale of non-electric vehicles by 2025 [78]. In the U.S. as of August 2019, 12 states have followed California and adopted ZEV (Zero Emissions Vehicle) mandates that require a certain fraction of vehicle sales be electrified vehicles [79]. Then, in September of 2020 California adopted more stringent standards under Executive Order N-79-20, requiring that all new passenger cars and light-duty trucks be electric by 2035 [80]. This trend shows no sign of slowing any time soon, and it is likely that more and more states and countries will adopt similar requirements.

This trend started with smaller vehicles such as the Toyota Prius and the Nissan Leaf as can be seen in Figure 5 which shows the sales of EVs and PHEVs in the U.S. between 2011 and 2017 [2]. The Chevy Volt, Nissan Leaf, and Toyota Prius Prime dominated the US plug-in vehicle until about 2015, when competition started to increase, particularly from Tesla. From 2011 to 2015, the Nissan Leaf accounted for the majority of pure EV sales, at which point it was overtaken by the Tesla Model S, and took a further market share hit in 2016 with the release of the Tesla Model X. Since then, the release of the Tesla Model 3 has resulted in Tesla dominating the US EV market. In 2020, Tesla sold 5 times the number of EVs than all other brands in the US, with Chevy's Bolt EV coming in second [81]. However, all of these vehicles have something in common: they are small (by American standards, at least). Of all EVs and PHEVs sold in the U.S from 2011 to 2017, only 9% of them where SUVs, station wagons, or mini vans. This occurred during a time when SUVs were gaining popularity at the expense of smaller vehicles [82]. The reason for this was simply that larger vehicles require more energy to move, and since batteries were expensive and have lower energy density than gasoline, larger vehicles were commercially impractical. [83].

But more recently, thanks to lowering battery costs that have dropped 80% between 2010 and 2018, producing vehicles with much larger batteries became financially feasible [84]. This, along with advances in battery technology have lead to a slew of larger electric and plug-in SUVs announced or available in 2019 [85]. With the recent release of the electric Ford F-150 Lightning, one of the most popular pickup trucks in the U.S. became an electric vehicle, potentially marking a turning point for the market. Even commercial and industrial vehicles are now beginning to be electrified, including long-haul trucks, transit buses, and even trains [86, 87]. Similar to the light EV market forecasts, the demand for electric buses is likely to significantly increase in the U.S. in the coming years. Several large cities have committed to fully electrifying their transit fleets, including San Francisco [88], Los Angeles [89], Seattle [90], and New York City [91].

The battery packs of electric vehicles have generally been built using a modular design. A module includes multiple cells that may be connected in series and parallel, voltage measurement points for the battery management system, and embedded thermal measurement. Modules often

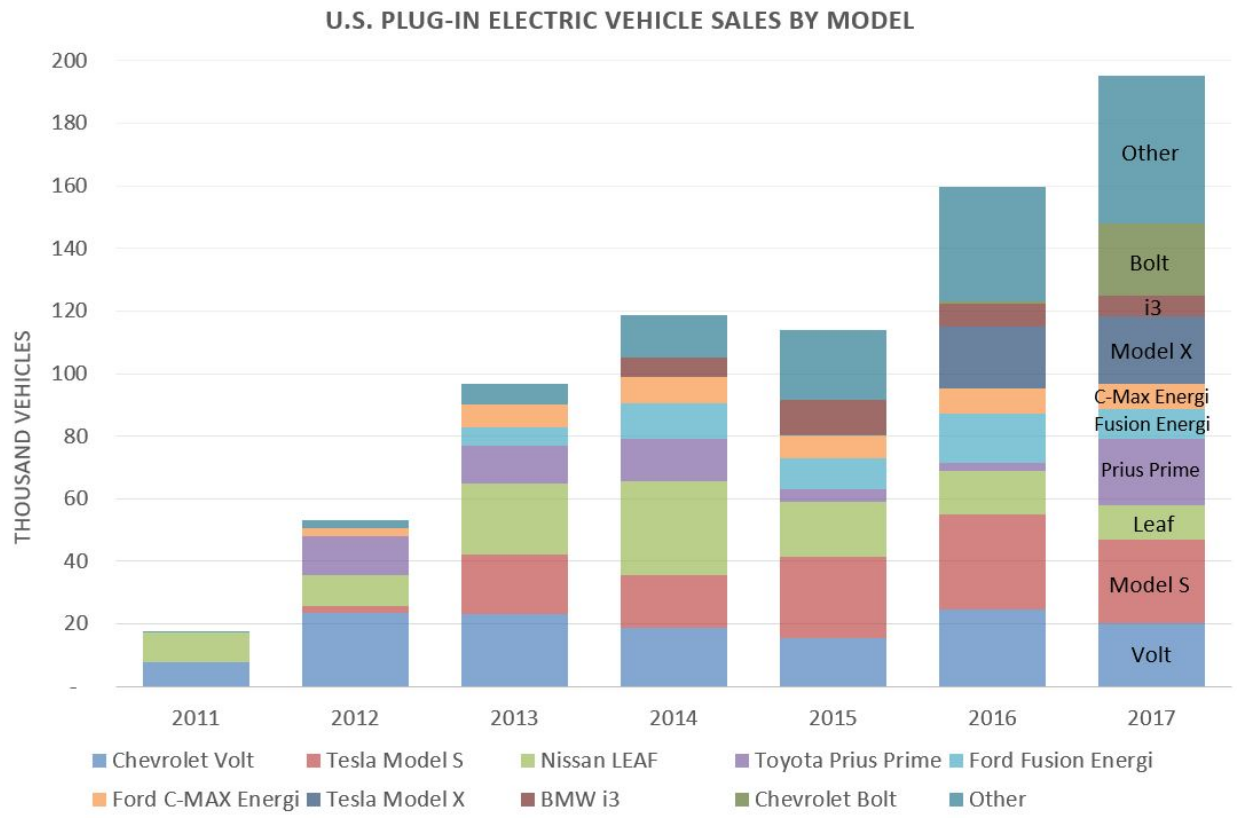

FIGURE 5. Figure showing the sales figures for the most popular models of battery electric and plug-in hybrid vehicles in the U.S. Figure generated with data from [2].

include external casing to reduce the possibility of damage to the cells, their terminals, and reduce the possibility of short circuit. Some modules may include integrated thermal management. Some examples of EV and HEV battery modules are shown in Figure 6. The cooling systems for the batteries can be seen in Figure 6 a) and b). a) shows the Chevy Volt battery module which uses a liquid cooling system with the coolant flow channel being at the bottom right of the image. The voltage and temperature measurement connector can be seen on top of the module. In b), the aluminum heat sinks attached to the modules can be seen. In the complete pack, these heat sinks are enclosed in a plastic duct with a BMS-controlled blower attached to the end. The voltage measurement connectors can be seen hanging off the back of the modules. Module c) shows an external busbar (covered in orange insulating plastic), with the voltage measurement connectors on the front of the module. The modules in d) contain no thermal management or temperature measurement hardware and the connections to measure voltage share the power terminals of the

modules.

As the vehicles powered by LIBs become larger, so to do their capacity and power demands grow, reaching up to 660 kWh/380 kW for electric buses. [92]. This means the battery packs become significantly larger and thus present a challenge in terms of thermal management. As was seen from Figure 6, different manufactures have adopted different strategies to keep their batteries within both a safe operating temperature and ensure maximum lifetime and performance of their batteries. Nissan has been one of the few EV manufactures that includes no (active) thermal management in their battery packs, but most manufacturers have adopted liquid cooling. The specifics of the cooling strategy are different for each cell form factor, and there are several possibilities for each form factor.

FIGURE 6. Figure showing battery modules from different electric and hybrid electric vehicles. a) Chevy Volt battery module. Note the cooling plate can be seen in the bottom of the image, along with the coolant distribution system at the bottom right. b) Hyundai HEV battery modules. The aluminum heat sink that can be seen of the left side of the modules formed a duct within the pack that was attached to a blower fan. c) A different Hyundai HEV battery module with a smaller heat sink assembly. d) Second gen Nissan Leaf battery modules, which had no integrated thermal management system.

For cylindrical cells, Tesla's liquid cooling system provides an example in Figure 8. In this design, a coolant tube is placed between every other row of cells in a battery pack or module [4, 93]. It can be seen that this strategy is likely to not uniformly cool the cells such that one side of the cell is cooled better than the other side of the cell. Cylindrical cells can also be cooled using forced air

cooling as shown in Figure 7. In this method, the cells are aligned similarly to the Tesla design, but instead of a cooling tube, air is blown through the pack or module to directly cool the cells. For air-cooled systems, the battery pack typically shares air with the passenger compartment since the optimal temperature range for LIBs is similar to temperatures most people find comfortable [94].

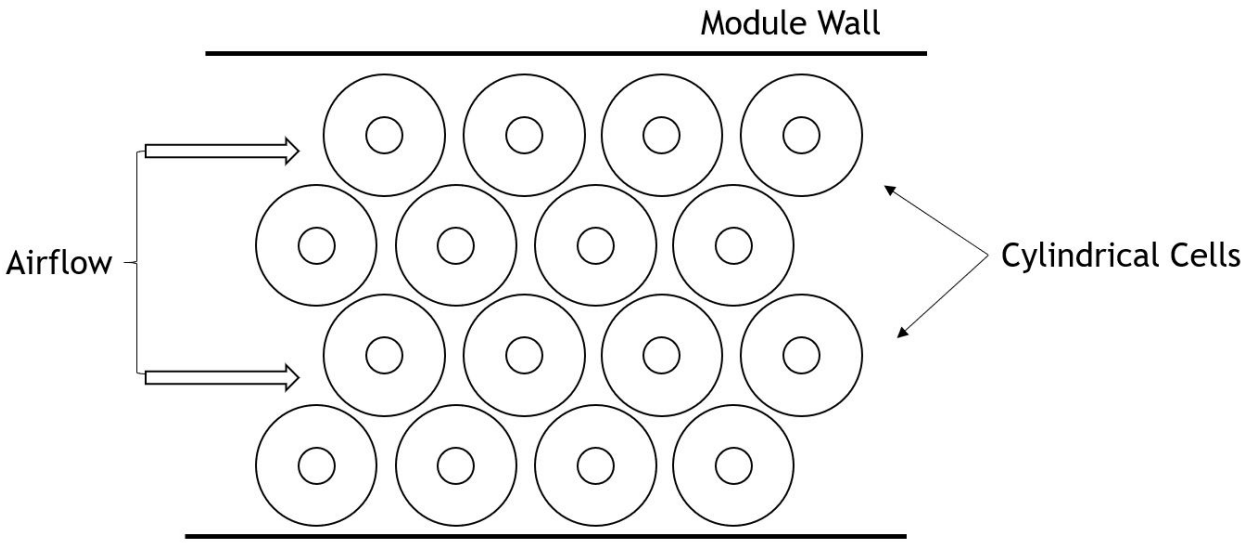

FIGURE 7. Figure showing air cooling method for cylindrical cells. Diagram inspired by Pesaran [3]

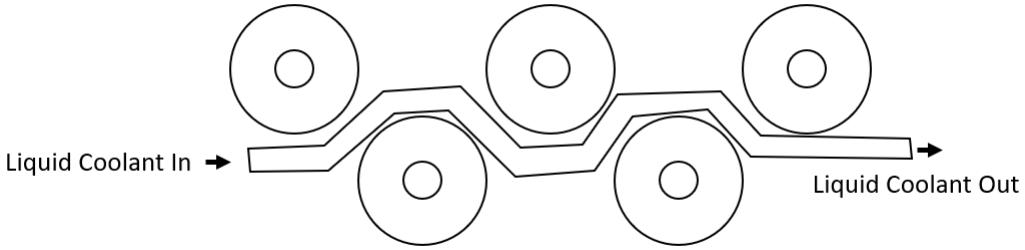

FIGURE 8. Figure showing the thermal management system developed by Tesla for cooling cylindrical cells. The wrapped coolant flow guides increase the contact surface area with the cell, increasing heat transfer efficiency. Figure based on information from Tesla Patent [4]

For pouch or prismatic cells, liquid cooling is exemplified by the Chevy Volt, which places cooling plates with liquid channels between every other cell in a manner similar to that shown for

cooling fins in Figure 9, except with one crucial difference. On one side of the pack, an incoming liquid coolant is distributed to the cooling plates in parallel flow channels etched into each cooling plate/fin. The warm coolant is then collected on the other side of the pack [95]. This is an effective but more complex and expensive method of cooling the battery. The simpler design shown in Figure 9 represents the cooling system in the Chevy Bolt and Hyundai HEVs [95]. For the Bolt with liquid cooling, the liquid coolant flows through the bottom cold plate, while the Hyundai HEVs replace the cold plate with an aluminum heat sink in a plastic duct. On top of the heat sink or cold plate is a layer of thermal interface material (TIM) to improve heat transfer. The cells may be placed directly against this or there maybe heat sink fins extending between the cells in the battery pack (as in the Bolt [96]). Another option for air cooling of prismatic or pouch cells is to replace the cooling fins from Figure 9 with a flow channel for forced air cooling.

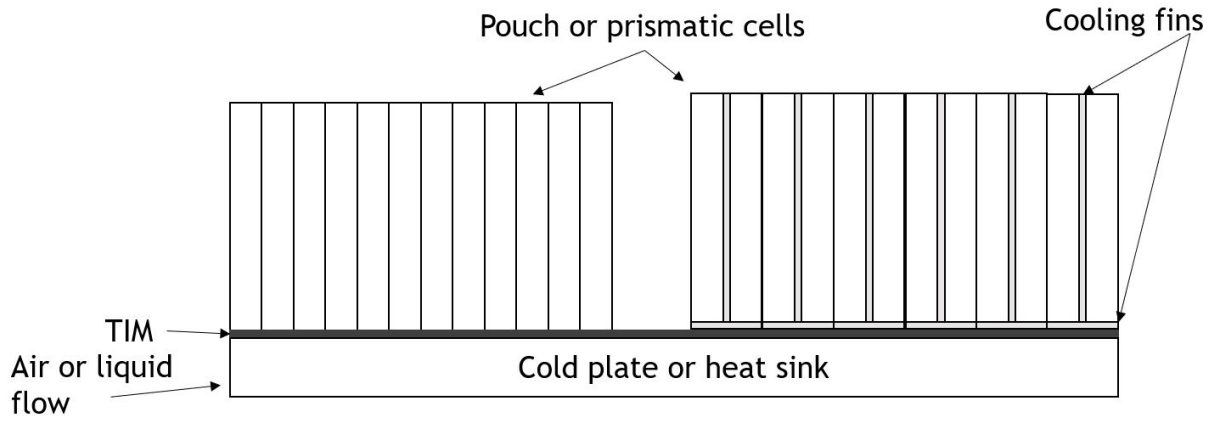

FIGURE 9. Figure showing the other methods of cooling prismatic cells with cold plate or heat sink.

These different approaches offer obvious advantages and disadvantages, for example liquid cooling is significantly more effective and can be directly controlled by the BMS rather than relying on the driver's temperature preference, but also incurs additional costs and complexity. The cooling system chosen also impacts the uniformity of temperature of the battery cells, which is recognized as a critical function of the thermal management system [94].

1.3 Stationary Applications

Another growing use for a large quantity of LIBs is stationary energy storage systems. These systems vary in size and purpose from a few kWh for home use to several MWh for grid scale systems. While the individual systems for stationary storage can be much larger than a vehicle's battery pack, due to the sheer quantity of electrified vehicles forecasted to be sold out to 2030, the stationary storage market is expected to be comparatively tiny. Between 2019 and 2030, stationary energy storage demand is expected to grow from around 10 MWh/year to 150 MWh/year [77]. However, this prediction appears small compared to industry group predictions of total installed stationary energy storage capacity of 110 GWh with annual installations rising from 1.9GW/yr in 2019 to 9.2 GW/year in 2025 [97]. At the end of 2017, the U.S. had installed 708 MW and 867 MWh of energy storage systems [98].

On the East Coast, most energy storage systems were installed to regulate power quality (frequency regulation) and thus have a high output power, but low energy storage capacity. For example, PJM (North East Transmission Operator) in 2017 had 278 MW and 269 MWh of energy storage capacity connected to their network and an average energy storage duration of 45 minutes. However, in California, CAISO (California Independent System Operator) in 2017 had 130 MW and 381 MWh of energy storage for an average duration of 4 hours and average power of 5 MW. The longer energy storage duration in California is due to a California Public Utilities Commission requirement that energy storage systems be able to supply their rated power for 4 hours in order to be counted as reliability reserve capacity [98]. The U.S. Energy Information Agency provides breakdowns of energy storage power and capacity by grid operator. In 2017, CAISO (California) accounted for only 18% of the national energy storage power capacity, but 44% of the energy storage capacity [98].

The demand for stationary storage in California has been driven by state regulations that required utilities to procure at least 1.3 GW of energy storage by 2020 [99]. As of the California Energy Commission's 2018 report [100], PG&E was required to install 310 MW of energy storage capacity, had procured 692.5 MW, none of which was operational. PG&E claimed in 2021 to have

procured 1.4 GW of energy storage capacity, but did not specify their operational status [101]. Thus, PG&E alone exceeded California's targets for installed energy storage. Note that utilities measure energy storage in MW, and it is therefore likely that the installed energy capacity of these systems could be in the range from 1.4-5.6 GWh. In addition to requirements imposed on utilities, California created incentives for private entities to install energy storage. One such incentive program was the Self-Generation Incentive Program (SGIP), which offered up to $378M in funding for customers who installed energy storage when they installed it along with PV generation [102]. SGIP funding was contingent on using renewable energy to charge the battery system, and thus was also a driver towards DC-coupling of solar generation and energy storage systems. The program offered at least $250/kWh towards the procurement price of the energy storage system [103]. The California state government has been pushing energy storage incentives to address peak energy usage (load shifting), defer transmission line and equipment upgrades, reduce greenhouse gas emissions, reduce transmission losses, provide ancillary services (frequency and voltage regulation), improve the performance of solar and wind generators, and reduce the need for natural gas powered peaker power plants [104].

Energy storage is especially well suited for these uses due to its low response time and high efficiency. Peak energy use has become a problem as more solar generation is connected to the grid. Figure 10 shows what is referred to as the *CAISO Duck Curve* [105]. It shows the demand for electricity in California and the net demand which is the demand minus the non-controllable (renewable) generation. Therefore the net demand is the demand that must be met by controllable (traditional) generation plants. It can be seen that during the day, solar generation results in a low net demand, but in the late afternoon, the peak demand coincides with the fall-off of solar generation. As a result, a high ramp-up of traditional generation is required, which is met by the use of inefficient 'peaker' power plants since larger more efficient plants have a slower ramp rate [105]. Energy storage can address this issue by charging from the solar generation during the day which increases the demand during the day, allowing traditional generators to avoid ramping down and for increased deployment of renewable generation onto the grid. Then in the evening, energy storage can discharge to reduce the peak demand and reduce the ramp rate required to

maintain the grid's stability. Peaker power plants are then not required, increasing the efficiency of the grid.

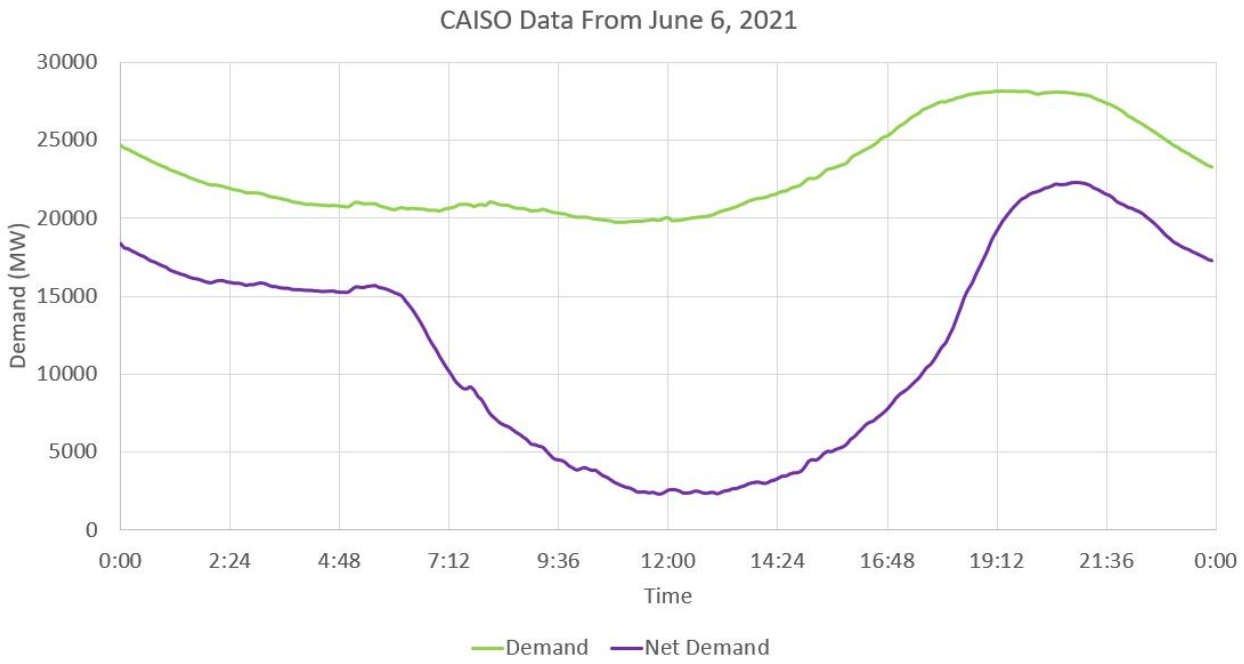

FIGURE 10. Figure showing the electrical demand in CA on June 6, 2021 comparing the total demand to net demand to show the afternoon generation ramp. Figure generated with data obtained from CAISO's website [5].

There is a potential advantage to the fact that stationary storage's market demand has been predicted to be smaller than that for electric vehicles. Since the degradation of LIBs is a function of the usage pattern (see section 4.1) and different applications have varying sensitivities to the health (degradation) of their battery packs, a battery that is considered 'end-of-life' for one application may be perfectly suited for use in another. Stationary storage designed for load shifting charges and discharges the battery more slowly (C/4) and with fewer high current events than driving an electric vehicle. In addition, energy density is not as large a concern for stationary systems as it is for electric vehicles, meaning using degraded cells may be an acceptable trade off for the reduced cost of energy storage achieved by utilizing retired batteries for new purposes [106]. Reused and repurposed batteries are called second-life batteries, and they have the potential to reduce costs for the original owner by increasing the scrap value and the costs for the second owner by nature

of being older.

There are strong environmental and economic reasons to reuse electric vehicle batteries after they have degraded to the point where the driver is no longer happy with the range the battery provides. In 2018, an estimated 50% of retired LIBs were recycled [107], leaving the remaining 50% to be buried, burned, or stored [108]. A major factor contributing to the low rate of recycling has been the high cost of recycling LIBs. Depending on the chemistry of the cell, the value of the recovered materials has been around 1/3 the cost of recycling the battery, even lower for cells with less valuable material such as LFP [109, 110]. If instead of recycling a battery after its first life, it is reused, then the cost of recycling is deferred. Also, since more use is made of the battery, the delivered kWh of the battery is increased, reducing the environmental impact per kWh of manufacturing and recycling of the cell. Further, if stationary energy storage systems are built from used EV batteries, then the need to produce new cells to meet the stationary storage demand is (partially) negated. This could also have a large positive environmental impact as lithium-ion battery production is an energy and mining intensive process [111].

Cooling strategies for stationary storage are just as diverse as they are for vehicle applications. For example, Tesla's Power Pack stationary energy storage system also uses liquid cooling [112], though the details of the internal cooling are not public, a reasonable guess would be that it is similar to the system used in their EVs. Several companies such as Spiers New Technologies and RePurpose Energy, and even Nissan themselves have reused Nissan Leaf batteries in stationary systems, and like Nissan, use passive air cooling for their systems [113,114]. The UC Davis Robert Mondavi Institute's Microgrid Energy Storage System uses climate control for a walk-in container as well as forced air cooling on the battery modules [106,115]. Some stationary storage systems use EV battery packs "as-is" and so keep the same variety in thermal management strategies discussed above. The longer duration 4 hour systems adopted by California utilities may not need advanced cooling beyond a climate controlled room due to the low charge and discharge rate. However the higher power EES designed for frequency regulation may require additional cooling as in EVs since the power demand is much higher then the demand shifting systems.

2 Problem Definition

It is well known that LIB performance and lifetime is a function of temperature, and that this temperature dependency is exponential (see Section 1.1). In the short term, increased temperature results in increased performance due to lowered electrochemical resistance (more favorable reaction kinetics), but in the long term causes accelerated degradation (also due to more favorable reaction kinetics). Additionally, it is known that variances in resistance between cells, especially second-life cells, result in differing heat generation throughout the battery pack [33]. This has been shown to result in a temperature difference of up to $20°C$ [15, 29] within a battery pack. When this occurs, the operating voltages and internal resistances of the cells are affected. This may cause the battery management system (BMS) to believe the cells are out of balance and begin balancing, even if their real SoC was the same. As a result, the cells would be made unbalanced by the BMS and the pack be at a lower overall SoC due to lost energy to balancing [94].

Since degradation is also a function of temperature, when the cells in a pack are at different temperatures, the pack will experience non-uniform aging. Over time, this can result in an overall healthy battery pack becoming unusable due to a small number of degraded cells. While the goal of a thermal management system (TMS) is to prevent the battery from getting too hot or cold ($15 - 45°C$) and to keep the temperature uniform to within $3 - 5°C$ [3, 116], practically the TMS cools the cells closer to the coolant inlet and coolant channels better than it cools the rest of the cells, resulting in non-uniform temperatures. If the battery pack has no TMS (such as the Nissan LEAF), the cells at the center of the pack can be expected to be warmer and degrade faster.

For cells connected in series, the internal resistance differences induced by the non-uniform temperature limit the performance of the battery pack. In this case, since the cells are connected in series, they all experience the same current, but a cold cell has higher internal resistance which results in a larger voltage drop when current is drawn from the pack. This means the cold cell reaches its end of discharge voltage before the warmer cells. When this happens, there are two possible actions, continue to discharge to extract the energy from the warmer cells thus over-discharging the cold cell, or stop discharging and reduce the available energy in the battery pack.

The same problem occurs while charging, except with the upper voltage limit, which reduces the rate at which the battery can be charged.

3 Research Objectives

The objective of this work was to quantify the effects of non-uniform temperatures on series-connected battery cells. This included changes to the degradation rate, degradation mechanisms, cell internal resistance, pack resistance and pack usable energy. By measuring these effects, battery pack designers could use the results combined with the expected operating environment of their battery packs to optimize their TMS to both ensure battery pack design lifetime and minimize costs associated with cooling and heating the pack. In addition, depending on the use-case and duty cycle (the ratio of cycle aging to calendar aging) of the pack, the design requirements of the pack and TMS may be different due to the differing aging mechanisms. This research sought to provide the insights required into the long-term ramifications of non-uniform temperatures, as compared to a battery pack kept at a uniform temperature. Some key questions this work will help address are:

- What proportion of the total degradation in capacity and performance is caused by calendar, cycling, temperature and non-uniform temperatures?
- How do the effects of non-uniform temperature differ between parallel and series connected cells?
- How does non-uniform temperature in a pack affect the rate of aging of the battery pack?
- How does non-uniform temperature affect the performance of a series connected battery pack?
- Is the effect of non-uniform temperature different at different average temperatures?
- What is difference between battery pack power capability and individual cell power capability?
- Which aging mechanisms are made worse by non-uniform battery pack temperature?

In this work, experiments were conducted to answer these questions and generate directions for future research to pursue to develop a comprehensive understanding of the effect of non-uniform temperature on the performance and lifetime of lithium-ion battery packs.

3.1 Motivation

While work has been done on parallel connected cells subjected to non-uniform temperatures, less effort has been directed towards series connected cells. At the same time, EV battery packs are built from many series connected cells [94]. In addition, EV battery packs are used in harsh environments, whether that be the desert in Arizona [27] or winter in Minnesota. These environments are conducive to the formation of temperature differentials within the battery pack. As the demand for large battery packs increases exponentially, so does the need to understand how temperature non-uniformity within these packs affects their lifetime and performance.

For stationary applications, utilizing second-life cells increases the importance of thermal management systems for battery pack design due to the degraded and inconsistent performance of the cells. The varied cell internal resistances can increase the magnitude of temperature differences within the pack, thus a good understanding of how temperature gradients change battery pack performance and lifetime is critical. For example, Pesaran modeled a HEV battery pack under the US06 drive cycle and predicted the formation of an $18°C$ ΔT [117]. Meanwhile, a Nissan Leaf battery pack that was disassembled showed that individual cell health from the same pack can vary up to 14%. The impact of these variances on second-life pack performance could be mitigated by testing each cell before usage, but work designing and building a 320kWh second-life energy storage system for the UC Davis microgrid showed that this is a time-consuming and expensive method of pack construction [106]. Understanding of the magnitude of the effect of non-uniform cell temperature on pack performance and degradation may allow faster but less accurate cell testing methods to be used to reduce pack production time.

A battery pack's BMS is capable of measuring the temperature of the pack in multiple locations, as well as the voltage of each cell (set of cells connected in parallel). This information allows the BMS to estimate the state of health (SoH) of the cells, and over a period of time allows the BMS to

estimate the remaining useful life of the cells. However, the accuracy of these estimations is limited in the case of non-uniform temperature that causes non-uniform cell degradation. Thus, a more complete understanding of the effects of temperature differentials between cells could improve the implementation of second-life battery packs and improve the accuracy of BMS calculations.

3.2 Contribution

Since EV battery packs usually consist of many cells connected in series and only a few in parallel (for example the Nissan Leaf has around 100 cells in series and only 2 in parallel), the effect of temperature gradients on series cells is an important topic for the automotive industry. Additionally, second-life batteries have varying internal resistances which induce temperature gradients in the pack at lower C-rates when compared with new cells. M. Klein [17] has shown that temperature gradients in parallel connected cells cause SoC imbalances between cells. He found that the hotter cells contributed more current to the discharge or charge than the colder cells, causing the hotter cells to become discharged sooner than the colder cells. However, the effect on series connected cells and the aging of the pack is yet unverified especially when long-term degradation is considered.

Since there are multiple degradation mechanisms at play for series-connected cells at non-uniform temperature, multiple experiments with the same cells must be done to quantify the contribution of each mechanism. There has been some simulation work done [33], but with simple degradation assumptions, limited experimental work, and no determination of the magnitude of the effects from different degradation conditions. Additionally, it is difficult to compare between studies to determine the magnitude of degradation for each testing condition because different cells were used. It is well known that the specific cell choice, even of the same general chemistry, influences the rate of degradation [118, 119]. For example, it is unknown how much the DoD imbalance contributes to the aging of the cells compared to the effects from simple storage/cycling at high or low temperatures.

This work was designed to isolate these effects by conducting experiments to quantify the effect of different aging conditions as applied to lithium-ion battery packs consisting of cells connected in series while under a temperature gradient. Additionally, the exact same cell model used by

Klein [17] for studying parallel connected cells were used such that a direct comparison between series and parallel packs could be made. This could improve the state of understanding regarding how battery pack thermal design affects the aging and performance of the battery pack. Just as how [17] determined the maximum acceptable temperature gradient within a battery pack for parallel connected cells, this work determined the corresponding limits for series connected cells while taking into account the effect on aging, not just short-term performance.

This work also provided data useful to second-life battery applications. One of the most important and time-consuming tasks when building second-life packs is matching the cell's properties as closely as possible to maximize pack performance. This work provided guidelines based on the degradation results that could help establish a baseline regarding the difference in capacity and internal resistance that are acceptable in a series-connected pack to minimize aging due to non-uniform temperatures.

Part II

Literature Review and Theoretical Approach

4 Theoretical Background

4.1 Cell Degradation

Aging, or degradation in the usable capacity and available power of a lithium-ion battery can be categorized into three groups: Calendar aging, cycling aging, and abuse. Calendar aging occurs regardless if the cell is used, and acts as a baseline minimum amount of degradation that cell will experience. Cycling aging occurs due to stresses induced by routine use of the cell. Abuse damages the cell by applying excessively high currents, over charging, over discharging, or subjecting the cell to extreme temperatures. These aging types consist of different, but overlapping stress factors such as current, temperature, and time. These *stress factors* each affect a set of *aging mechanisms* such as SEI formation, lithium plating, or gas formation. Each aging mechanism affects the cell's performance through one or more *aging modes* such as loss of active lithium, loss of anode material,

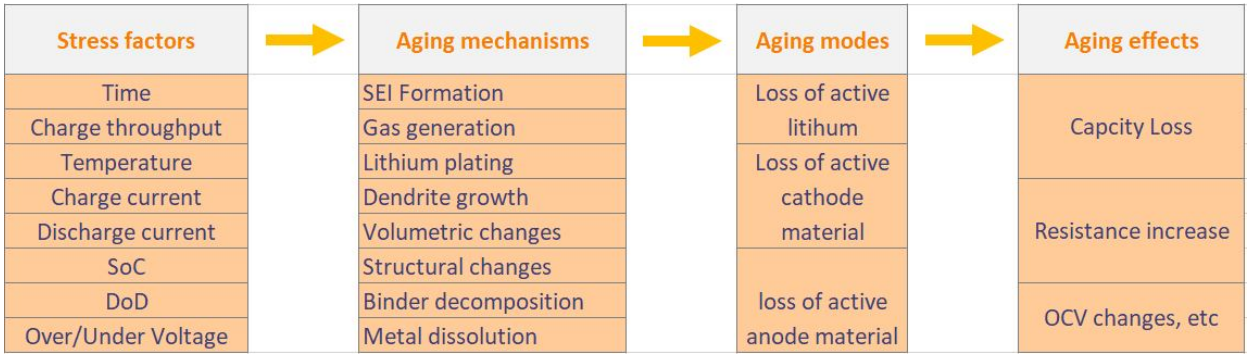

FIGURE 11. Figure illustrating the relationship between degradation stress factors, mechanisms, modes, and effects. Figure generated from information from [6].

or loss of cathode material. Finally, these aging mechanisms and modes have an *aging effect* on the cell, which is the measurable change in the cell's performance such as reduced capacity, increased internal resistance, and the interaction these properties have with the SoC and voltage of the cell [6]. The relationship between these degradation factors is shown in Figure 11. This also illustrates the difficulty in determining the exact relationship between applied stress factors, measured aging effects, and actual aging mechanism. While it is nearly impossible to determine the relationships exactly, various tests have been developed, that in combination with modeling, can quantify some aging mechanisms.

An overview of aging mechanisms is shown in Figure 12. These are the physical mechanisms through which calendar, cycling, and abuse degradation affect the performance and lifetime of a cell [7]. Each of these mechanisms are affected by a different linear combination of the stress factors shown in Figure 11. Below is a review of how calendar and cycling each uniquely contribute to the degradation of lithium ion cells.

Calendar aging's primary mechanism is growth over time of the solid-electrolyte interface (SEI) layer. Calendar aging is primarily a function of the stress factors of time and temperature, but is also affected by storage SoC/voltage [120]. It is commonly modeled in a form similar to:

$$Q_{loss} = A \exp\left(-\frac{E_a(SoC)}{RT}\right)\sqrt{t} \tag{26}$$

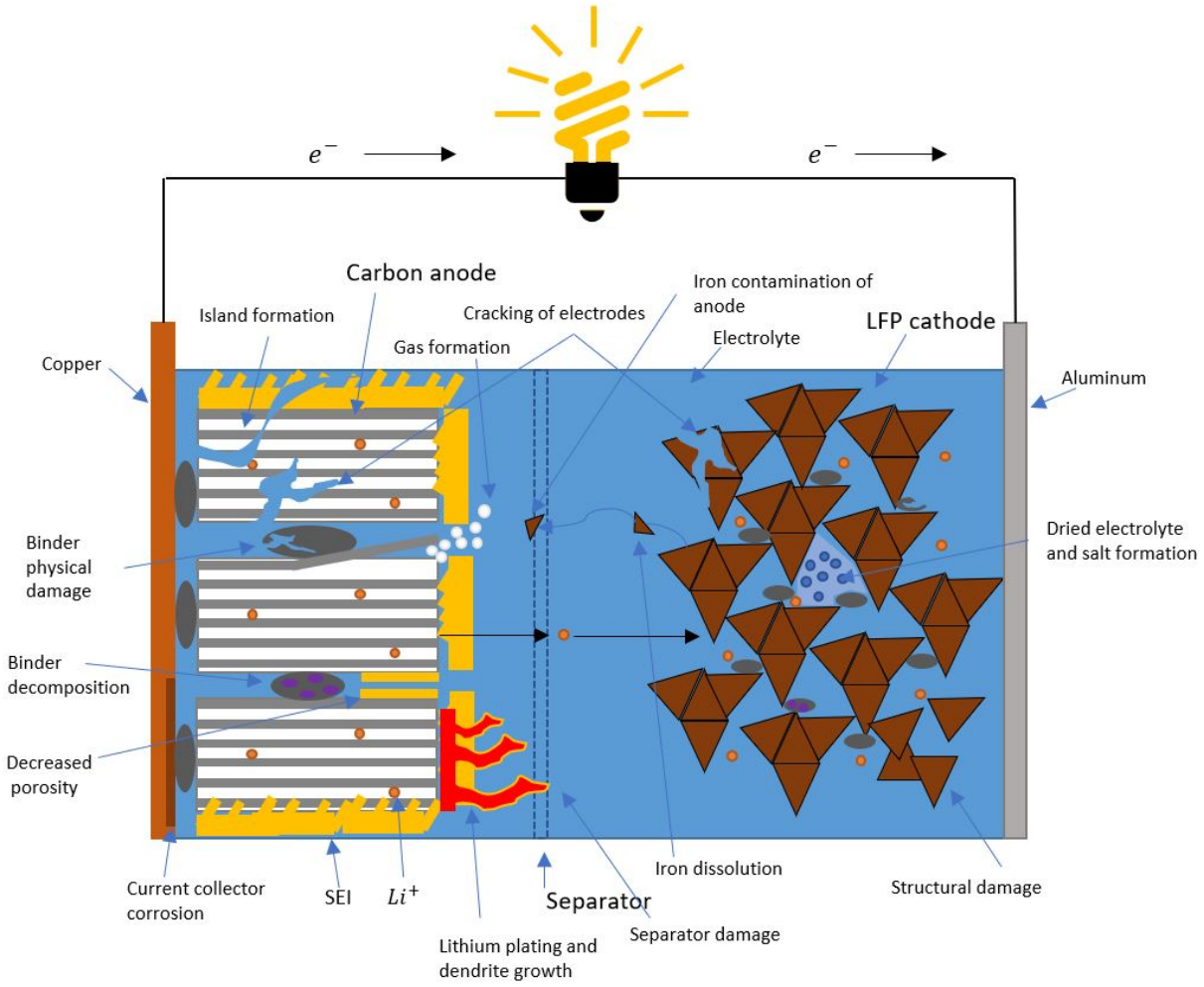

FIGURE 12. Figure showing the operation of a lithium-ion cell discharging as well as the underlying causes of lithium ion battery degradation in addition to those shown in Figure 13. Each of these physical phenomena are influenced differently by cycling, calendar, and abuse aging. Figure created based on information from Merla et. al. [7].

Where Q is the capacity loss, A is an experimentally determined pre-exponential factor to fit the degradation model to a particular chemistry, E_a is the activation energy of the degradation side reactions in Joules per mol, R is the ideal gas constant, T is the temperature in degrees Kelvin, and t is the experimental time. This form shows that the rate of capacity loss slows over time, which can be attributed to the thickening of the SEI layer as illustrated in Figure 13. Since the SEI layer forms when the electrolyte reacts with the anode, as the SEI forms the anode becomes protected by the SEI, slowing the reaction rate and thus the calendar aging.

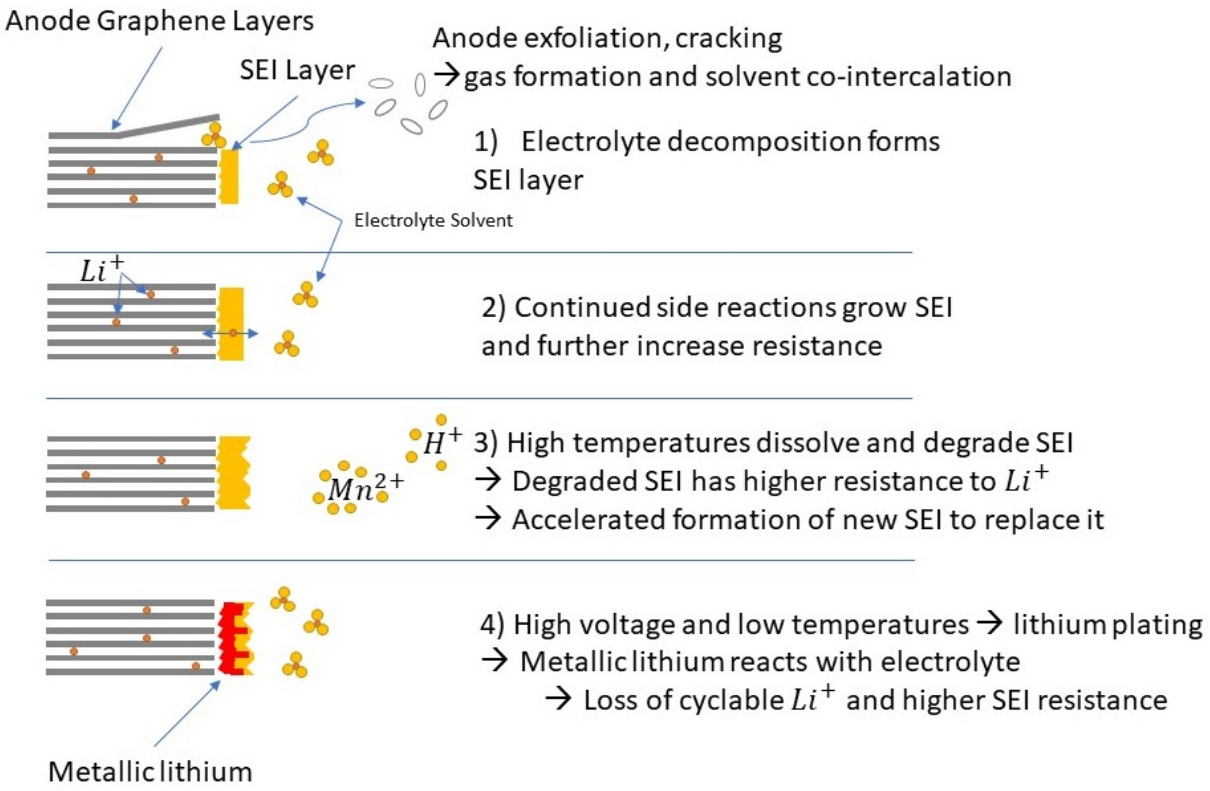

FIGURE 13. Diagram showing the various aging mechanisms associated with the solid-electrolyte interface and how it grows over time. Figure recreated based on information from [8].

If the temperature is increased, the reaction kinetics become more favorable and the side reactions accelerate resulting in faster calendar aging [120]. Kassem et. al. showed that this degradation also resulted in increased battery resistance resulting in a reduction in maximum power output. They determined that temperature was the most significant stressor that caused power fade, but that for any given temperature, cells stored at higher SoCs degraded more, with power fade ranging from 5-15% after 4 weeks of storage between $40 - 70°C$ [121].

Similarly to power fade, the capacity of cells is also degraded by storage at elevated temperatures. Nauymann et. al. showed how storage SoC and temperature affect cell remaining capacity [122]. It was found that the capacity degradation was strongly dependent on cell temperature, and that the effect was non-linear in temperature. They found a linear relationship to capacity fade vs time for temperatures under $60°C$. Storage SoC was also seen to affect the capacity fade, but like power fade, to a much smaller degree than storage temperature. Their cell stored at $0°C$ experienced

approximately 1% capacity degradation over one year, while the cell stored at $40°C$ and 50% SoC degraded by 5%. Further tests of these calendar aged cells showed that the aging mode of capacity loss was loss of cyclable lithium to side reactions at the anode (i.e. SEI formation) [121]. It has been suggested that the impact of storage voltage is due to an increased rate of cathode metal dissolution into the electrolyte, which then reacts with the lithium in the electrolyte which both increases SEI resistance and capacity fade [123].

Calendar aging also affects the internal resistance of LIBs, which in turn reduces the maximum power the cell can deliver. Amine et. al. showed this in their paper in which they constructed custom cells to examine the changes to the electrode and the SEI caused by degradation. This revealed that cells stored at higher temperature exhibited a much higher rate of internal resistance increase than cells stored at cooler temperatures. [124] The effect of storage voltage/SoC can also be seen, but it is smaller than the effect of temperature. It was also found in [124] that the internal resistance at the cathode was increased during calendar aging resulting in significant power fade. This is likely caused by high storage potential resulting in dissolution of some cathode material [123]. The decomposition of the electrolyte following $LiPF_6 \rightarrow LiF + PF_5$ also has the effect of increasing the resistance of the cell by reducing the ability of the electrolyte to transport lithium ions.

Cycling aging includes the stress factors of cumulative charge/discharge capacity, temperature, current magnitude, depth of discharge, and average SoC [6, 125–127]. These result in volumetric changes, cell delamination, dendrite growth, binder decomposition, SEI formation, and metal dissolution aging mechanisms. This leads to all three of the aging modes listed in Figure 11, loss of active lithium, and loss of active material at the anode and the cathode. The aging effects of cycling are reduced capacity and increased internal resistance, both Ohmic and electrochemical.

The primary mechanism of cycling aging is, as with calendar aging, due to SEI formation [127]. However, cycling aging further grows the SEI due to volume changes at the anode and due to co-intercalation of the electrolyte into the anode. Damage to the anode and the cathode is expected during cycling, as they both experience a volume change when lithium is (de)intercalated. For

LFP cells, the volume change is up to 6.8% [40]. This volume change results in the SEI cracking, re-exposing the anode to the electrolyte, resulting in additional SEI formation which consumes more active lithium and contributes to the SEI thickening over time, increasing the cell's internal resistance [8]. This phenomenon was verified by Waldmann et. al. [125] by using x-ray computer tomography and scanning electron microscopy to view the internal structure of cylindrical cells cycled at different C-rates and cells kept at rest. They found that higher C-rates resulted in significant deformation of the cell's jelly roll and caused delamination of the separator from the active material of the cell along with extensive cracking of the anode and cathode. This process both increases the Ohmic resistance of the cell through lowered conductivity of the anode and cathode, but also increased the electrochemical resistance by increasing the SEI thickness. It has been observed using scanning electron microscopy that the SEI thickness can increase by around 10x ($\tilde{4}$0nm to 4$\tilde{0}$0nm) from storage at elevated temperature or from as little as 12.5% capacity fade from cycling [128, 129]. When the SEI in one area of the cell becomes thicker, it clogs the pores in the anode where lithium ions (de)intercalate, which decreases the reaction kinetics of (especially) charging and discharging [130]. Anode porosity has been observed to reduce by 50%, from 0.25 to 0.12 due to this phenomenon [131]. This causes the current density at other sites to increase which leads to locally high lithium concentration. When enough intercalation sites are blocked by the SEI, the lithium concentration becomes high enough to result in lithium plating while charging, even at normal rates and temperatures [132, 133]. Once this occurs, the degradation rate becomes non-linear again and degradation accelerates exponentially [130, 134].

Capacity loss from cycling is generally modeled as linear for constant C-rate, temperature, and DoD [127, 130, 135, 136], but with different slopes for each different battery type. The first several cycles typically result in more rapid aging, which then levels off for most of the life of the cell [134]. The relationship between the slopes for different C-rates is exponential, and a function of total current throughput, as described by Wang et. al. [127].

$$Q_{loss,\%} = A_1 \cdot exp(A_2 \cdot C_{rate}) \cdot \int_{t=0}^{t_{end}} |I| dt \tag{27}$$

where A_1 and A_2 are fitting constants for the particular cell type. This model contains no explicit reference to temperature, but if the cell is cycled at constant temperature, the effect will be baked into the fitting constants. Then, by observing how the fitting constants change with cells cycled at different temperatures, the relationship can be adapted to include the effect of (constant) temperature on cell lifetime:

$$Q_{loss,\%} = (a \cdot T^2 + b \cdot T + c) exp\left((d \cdot T + e) \cdot C_{rate}\right) \cdot \int_{t=0}^{t_{end}} |I| dt \tag{28}$$

where the fitting constants have units of $a = (Ah \cdot K^2)^{-1}$, $b = (Ah \cdot K)^{-1}$, $c = Ah^{-1}$, $d = (K \cdot C_{rate})^{-1}$, $e = {C_{rate}}^{-1}$, and $f = day^{-\frac{1}{2}}$.

The non-linear portion of cycling degradation for the first few cycles is generally considered to be due to initial formation of the SEI. An empirical method similar to the one proposed by Wang et. al. above, but with more physical meaning ascribed to the fitting constants was proposed by Bolun et. al. [134]. This method of modeling the capacity loss per cycle due to SEI formation (α_{SEI}) is to assume (or measure) the portion of the total capacity that is lost during the first cycles. This portion is highly dependent on the physical construction of the cell's anode, and can vary from 3% to 16% of the cell's nominal capacity. This value is then used in the simple exponential degradation function

$$Q_{loss,\%} = 1 - \alpha_{SEI} \cdot e^{-f_{SEI}} \cdot 100\% \tag{29}$$

to model the initial high rate of degradation. Where f_{SEI} is a linearized degradation rate which must be obtained through fitting the model to measured degradation data for the particular cell (i.e. cell of the same model number).

Similarly, the non-linear portion of the degradation curve that occurs at the end of the cell's life is modeled by scaling the exponential degradation factor based on the current SoH of the cell. Considering Equation 27, the scaling based on SoH can be implemented as

$$Q_{loss,\%} = A_1 \cdot exp\left(A_2 \cdot (1 - SoH) \cdot C_{rate}\right) \cdot \int_{t=0}^{t_{end}} |I| dt \tag{30}$$

This approach to battery degradation modeling is extremely empirical, but is also very common in the literature due to a lack of comprehensive battery degradation modeling theory [137].

4.2 Degradation Identification

4.2.1 Aging Effects

Aging effects are the easiest to identify because they are directly measurable. They include cell internal resistance, maximum power capability, efficiency, available capacity, time to full charge, and self-heating rate. All of these effects are representative of the real "SoH" of the cell, and many are functions of charge/discharge rate or SoC. Measuring each of these effects for each degradation state of a cell is time consuming. Therefore, SoH is typically summarized either by available capacity or by internal resistance, depending on cell application as an energy battery or a power battery [94]. In some cases, SoH is normalized to a pre-defined end of life condition of the cell, for example 80% remaining capacity. Then the SoH = 0% occurs when the cell's capacity is 80% of its original capacity. In this work, SoH is defined as the capacity of the cell compared to its new capacity with no normalization for a defined end of life.

Internal resistance is typically measured using a test similar to that shown in Figure 14. A high current pulse is applied to the cell and the voltage change of the cell is recorded over a period of 10 seconds. The Ohmic resistance is measured as the 'instantaneous' (smallest measurable time step) voltage drop (or rise) of the cell (also referred to as 0.1s resistance after the time step used to measure it). The electrochemical, or diffusion, resistance of the cell is measured by the change in voltage over the 10 second current pulse, not including the initial Ohmic voltage

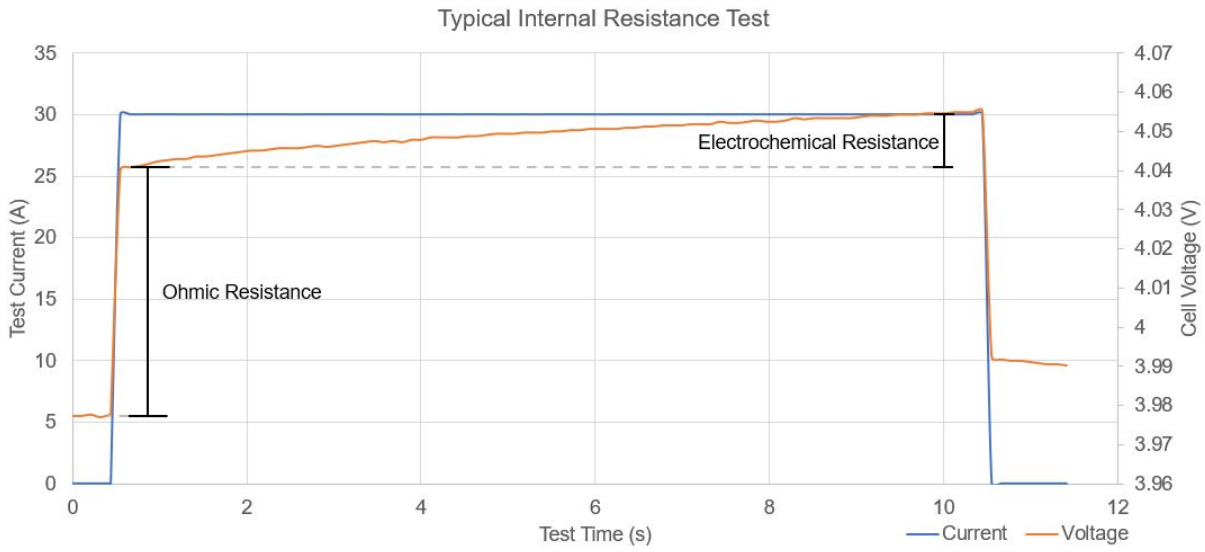

FIGURE 14. Figure showing an example cell test measuring the internal resistance of a Nissan LEAF battery cell. The time resolution of the measurement is 0.1 seconds. This cell has an Ohmic resistance of 2.09mOhm and an electrochemical resistance of 0.50 mOhm.

drop. Alternatively, the 10s internal resistance is the sum of the Ohmic (0.1s) resistance and the electrochemical resistance and measures the resistance over the total voltage change over the entire current pulse. Ohms Law is used to calculate the resistance from the applied pulse current and the measured voltage response. Lithium-ion cells do not have just one pair of Ohmic and electrochemical resistances. The resistances are functions SoC and temperature, as discussed in Section 1.1. An example of the dependence on SoC and temperature of the same cell type as shown in Figure 14 is shown in Figure 15. As cells age, both their Ohmic and electrochemical resistances increase.

The maximum power capability of a cell is strongly dependent on the internal resistance of the cell. The maximum power the cell can deliver is set by the highest current that can be drawn from the cell without the voltage dropping below the cell's discharge cutoff voltage. When the internal resistance of the cell is higher, the voltage drop from current draw is larger, which reduces the maximum power the cell can deliver. The maximum power is also a function of SoC of the cell, as higher SoCs (i.e. higher cell voltages) result in a larger available maximum current.

Cell efficiency can also be measured directly, and decreases over time as the cell ages. There are two efficiencies that are considered in terms of LIBs. The first is the standard definition of efficiency, energy output/energy input or discharge energy / charge energy. For LIBs, this is measured as

$$\eta_{energy} = \frac{\int_{SoC=100\%}^{SoC=0\%} I(t)V(t)dt}{\int_{SoC=0\%}^{SoC=100\%} I(t)V(t)dt} \tag{31}$$

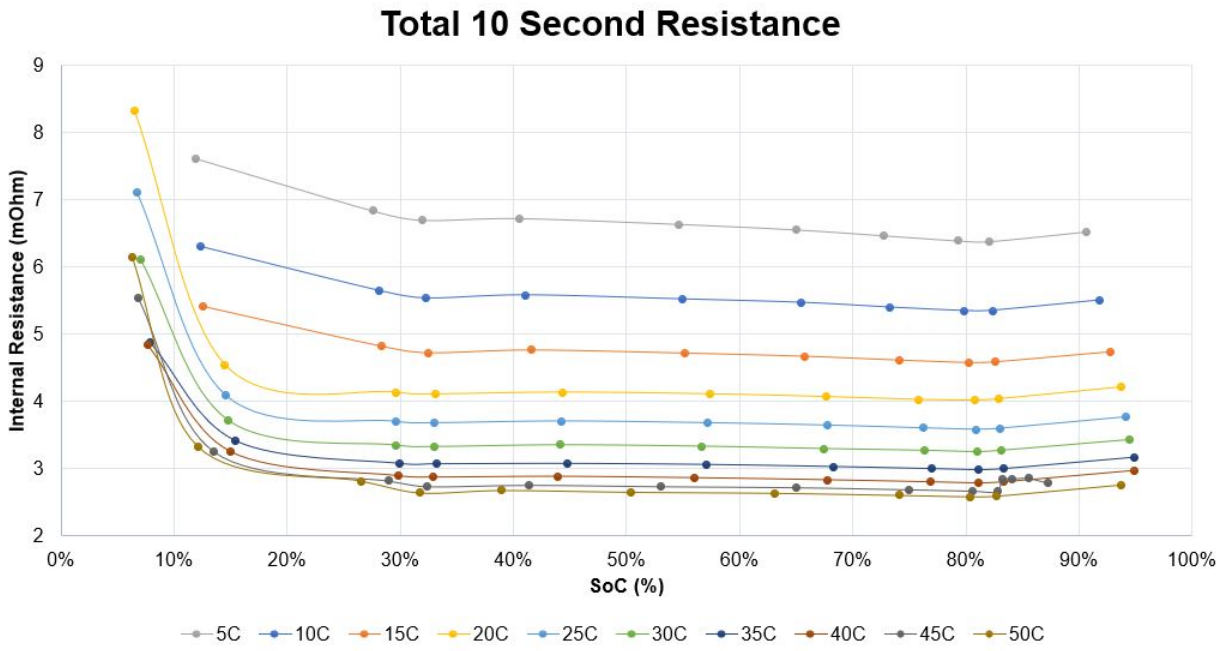

FIGURE 15. Figure showing an example module test measuring the internal resistance of a Nissan LEAF battery module at different SoCs and temperatures. The values for resistance shown here are the sum of the Ohmic and the electrochemical resistances.

The second is Coulombic efficiency, which considers the amount of current discharged/charged into the battery.

$$\eta_{Coulomb} = \frac{\int_{SoC=100\%}^{SoC=0\%} I(t)dt}{\int_{SoC=0\%}^{SoC=100\%} I(t)dt} \tag{32}$$

The energy efficiency of the battery takes into account the effect of voltage drop due to the internal resistance of the cell, while the Coulombic efficiency measures the effect of irreversible side-reactions within the cell that consume active lithium and electrons. As such, the Coulombic efficiency is a measure of the degradation rate of the cell, which is typically slow, so $\eta_{Coulomb}$ is typically very near 1 ($> 99.8\%$) [138, 139]. As cells age, the Ohmic resistance steadily increases (hence the energy efficiency of the cell decreases) [94] as the SEI layer thickens and the anode and cathode become damaged. Meanwhile, the Coulombic efficiency exhibits more complicated trajectories. For LFP cells, it tends to be lower during the first several cycles as the SEI forms, but then increases and remains steady for the majority of the life of the cell, reflecting the rate of degradation of the cell [138]. The efficiency of a cell is dependent on cycling temperature and cycling rate. A higher temperature means lower resistance, so a higher energy efficiency [17]. However, higher temperature also increases the rate of side reactions and thus decreases the Coulombic efficiency of the cell [139]. Higher cycling rates result in lower efficiencies [140, 141]

Available capacity can be measured in terms of Ah or Wh, as calculated in Equations 31 and 32. Measuring cell capacity in Ah is most common in the battery literature because it is more representative of the amount of available reactants within the cells. The measured capacity is dependent on temperature and cycling rate. The end of discharge cutoff voltage of a cell is reached sooner when the current is higher due to increased voltage drop due to internal resistance, thus lowering the extractable energy. Likewise, when the cell temperature is lower, internal resistance is increased, leading to the cutoff voltage being reached sooner. When charging, a constant current constant voltage charge is typically used. When the cell's maximum voltage is reached, the charger switches to constant voltage mode and the charging current gradually decays towards zero. High charging currents and lower cell temperatures result in the constant voltage phase of charging to start sooner, extending the charging time. Reported values of cell capacity should therefore always include the temperature and C-rate at which the cell was tested.

The cell's self-heating rate is a function of its internal resistance, applied current, and entropy generation. The cells' entropy generation is a function of SoC and SoH of the cell, specifically, of

the entropy of the crystal structures in the anode and cathode of the cell. As the cell ages and the structure of the crystal degrades, the cycling entropy profile of the cell changes [141–144]. The entropy change can be calculated as shown in Equation 9. Wu et. al. [145] have shown a linear relationship between the cell's SoH and the time from beginning of charge to the minimum of dT/dt, showing that the cell's entropy change is a good measure of SoH. Therefore, by measuring a change in the rate at which a cell's temperature changes during operation, information about the degradation of the cell can be obtained.

4.2.2 Aging Modes

Aging modes are the effects on the cell caused by aging mechanisms. Each aging mechanism causes cell performance degradation through a linear combination of the aging modes shown in Figure 11. Aging modes are more difficult to identify, as for example, a loss of lithium inventory and loss of active material both result in reduced cell capacity. A loss of lithium inventory (LLI) occurs when the lithium-ions in the cell participate in irreversible side reactions or become trapped in unreachable sections of the anode or cathode [146]. LLI can be detected using incremental capacity analysis, which measures $\Delta Q/\Delta V$ (Ah/V) to generate a plot showing which operational voltage ranges of the cell contain the most usable charge. This is important to understanding the cell's health because it represents each of the lithinination phases of the cell (i.e. $LiC_{12} \rightarrow LiC_6$ in the anode). Each of these phases has a different capacity, and degrades uniquely as the cell ages. Since these phase transitions happen at constant cell voltages, dQ/dV is able to detect the different aging of each of these phases, and thus the degradation of the cell [147–149].

Loss of active material (LAM) occurs when the anode or cathode become damaged. This can be caused by island formation (loss of contact of active material particles with the bulk of the material), cracking of the electrodes, dissolution of cathode metals into the electrolyte, or loss of electrical contact of parts of the electrodes, among other modes [7, 149], as shown in Figure 12. This can be detected using high resolution X-ray computed tomography as done by Waldmann et. al. [150]. It has also been shown that careful analysis of incremental capacity and differential voltage curves can qualitatively identify LAM, and from which electrode the material was lost [149].

4.2.3 Aging Mechanisms

Aging mechanisms are the physical and chemical changes within the cell that occur as it degrades, acting through the aging modes described above. Aging mechanisms are invoked through the operation and storage conditions of the cell. As previously mentioned, SEI formation is the primary degradation mechanism under normal operating conditions, as it occurs during calendar and cycling aging [120, 127]. The SEI, introduced in Section 1.1, is a function of cell age, storage/cycling temperature, average voltage/storage SoC, and cell cycling rate [120,151,152]. Despite the importance of the SEI to the performance and degradation of LIBs, quantitative descriptions of its formation from first principles that can be applied to test measurements of real cells are still lacking in the literature due to the large number of factors affecting it's formation [153]. For example, consider the model proposed by Ploehn et. al. [154]

$$L(t) = 2\lambda\sqrt{D_S^0 \exp\left(-\frac{E_a}{RT}\right) t} \tag{33}$$

where L is the thickness of the SEI, D_S^0 is the Arrhenius diffusion constant, E_a is the activation energy of the diffusion process of the electrolyte through the SEI, and λ is

$$\lambda = \frac{c_{eq}}{\sqrt{\pi} c_P} \frac{\exp\left(-\lambda^2\right)}{erf(\lambda)} \tag{34}$$

where c_{eq} is the concentration of the solvent at the SEI/electrolyte boundary, and c_P is the concentration of the irreversible reaction products in the SEI (i.e. the concentration of the SEI). The use of concentrations makes this difficult to apply to arbitrary commerical cells, however we can note the similarity of the SEI formation model to the experimental calendar aging model given in Equation 26, which is more practical to apply.

Elevated temperature increases the rate of SEI formation through improved reaction kinetics of the irreversible side reactions within the cell [151]. Temperatures above 40C lower the oxidation potential of the electrolyte below the cathode voltage in many cell chemistries to 4V, and at 60C, to 3.8V. This results in an SEI layer forming on the cathode as well as the anode [153]. SEI formation primarily results in LLI, and causes reduced cell capacity and increased resistance. Cycling of the cell increases SEI formation rate by providing electron and Lithium-ion flux through the SEI, increasing the chances for co-intercalation of electrolyte and concentration of reactants for side reactions [152]. High average voltage increases the SEI formation rate by reducing the activation energy of the side reactions [1]. EIS has been shown to be able to detect the increase in resistance of the SEI, and hence the growth of the SEI layer [155, 156]. By fitting the EIS results to a circuit model similar to that shown in Figure 16, with several RC pairs in series it has been determined that the SEI resistance can be measured by considering the mid-range frequencies from about 10-1000 Hz [156, 157].

Gases can develop within a LIB due to undesirable side reactions and due to the initial formation of the SEI as seen in Equation 1, after which the gas formation rate drops significantly [158]. It has been shown that under typical cycling conditions, internal gas formation is a negligible degradation mechanism [158, 159]. Gas formation occurs in LFP cells primarily due to abuse, application of high temperatures in the range of 42-69C, depending on cell composition [160], and severe over discharge (down to 0V). The gases formed in the cell due to these conditions are mainly H_2, CH_4, and C_2H_5. The gas formation was attributed to extensive side reactions occurring at low cell voltages [161]. For cells containing cobalt in their cathode, overcharging has been shown to result in significant gas production due to migration of Co to the anode SEI where it participates in additional side reactions which can generate oxygen, leading to additional safety concerns [162]. Formation of gases within the cell can result in damage to the anode and cathode (LAM), leading to reduced cell capacity [8].

During charging, the low potential of the anode, $< 0V$ vs. Li/Li^+ results in Li metal precipitating out of the electrolyte and plating onto the anode, and higher charging currents and voltages

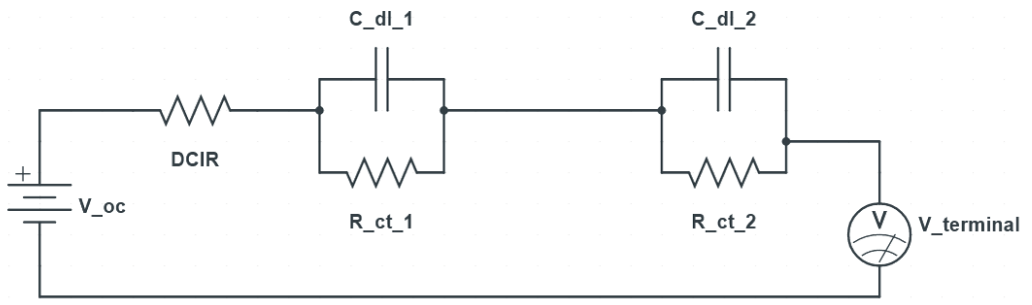

FIGURE 16. Diagram of a typical equivalent circuit model of a LIB. ECMs consist of a voltage source that produces the OCV curve of the battery as a function of the state of charge. The resistor *DCIR* represents the Ohmic resistance of the cell, while the resistor-capacity pairs represent the electrochemical resistance of the cells through modeling of the double layer capacitance and charge transfer resistance. [9, 10]

increase the rate at which lithium plates [7, 126, 163–166]. Reduced temperature lowers the potential of the anode, further inciting lithium plating. Lower temperatures also reduce diffusion of Li into the anode, resulting in larger concentration gradients of Li ions at the anode's surface leading to more lithium plating [126, 166, 167]. Eventually, lithium plating can lead lithium dendrites growing on the surface of the anode. Left unchecked, these dendrites can penetrate the separator and cause an internal short-circuit in the cell [45, 168]. The plated lithium also reacts with the electrolyte to form a second SEI, which is added to each time additional lithium is plated. This leads to a significant increase in SEI thickness, internal resistance, LLI, and lowered Coulombic efficiency [8, 169, 170]. However, if the cell is discharged soon, the plated lithium can dissolve back into the electrolyte and the capacity of the cell can be restored. The ratio of reversible lithium plating to irreversible lithium plating is SoC dependent. At low SoC ($SoC < 90\%$), lithium plating is primarily reversible, but lithium plating occurring above 90% SoC is primarily irreversible and results in cell capacity loss. Lithium plating can be detected using differential voltage (DV)

analysis iff the plating occurred on the previous charge step. This is achieved by observing the discharge voltage plateau caused by stripping the lithium off the anode, which occurs before normal deintercalation of lithium ions from the anode [170]. Lithium plating can also be detected using neutron radiography, but due to the low resolution of measurements and the requirement for a nuclear reactor, this is not a practical detection method for real-world applications [168].

When cycling a cell, the volume of the electrodes changes due to the intercalation and deintercalation of lithium ions into them. This results in a measurable change in the thickness of the cell on the order of 0.1-0.2mm per cell [171]. Considering the Nissan Leaf battery pack with 192 cells, this amounts to a thickness change of 19.2-38.4mm, which is not insignificant. To mitigate this expansion, pack manufactures apply pressure to the ends of the cell stacks, which reduces delamination of the anode/separator/cathode stacks within the cells due to volume changes [172]. X-ray diffraction measurements have shown that a fully charged anode has around a 10% larger volume than a fully depleted anode [173]. Lee et. al. [171] observed a typical volume change of 4% on the first cycle, and 2% on subsequent cycles. This at first does not seem consistent with a 10% volume increase of the anode and a 6.5% decrease in the volume of the cathode of LFP cells [40] when going from 0-100% SoC. However, when considering that the anode is over sized in most cells as to help avoid overcharge of the anode [174], that the largest increase in anode size occurs at the last stage of graphite intercalation [173], and the variations between different cell construction, these results can be considered to agree. The volume change of the electrodes during cycling results in increased cell degradation due to cracking of the electrodes, SEI, and folding of the jelly roll, and is enhanced at high cycle rates [150]. This results in an increase in the cell's resistance, a loss of active material, and loss of active lithium to the additional SEI formation [8]. For pouch cells, the volume change can be detected directly by measuring the thickness of the cell [171], however this is not possible with cylindrical cells contained within a rigid metal can.

The binder in a LIB is what holds the electrode particles together and attaches the electrode to the current collectors. As such, it is a critical component of a well-functioning cell, but is also prone to degradation [7]. The main degradation mechanism of the binder is a reaction with the

fully charged anode that forms LiF [8, 175].

$$-CH_2 - CF_2 - + Li \rightarrow LiF + -CH = CF - + \frac{1}{2} H_2 \tag{35}$$

Binder decomposition takes place along with SEI formation reactions in the anode, leading to reduced cell capacity [176]. Eventually, a lack of binder strength can result in delamination of the electrode from the current collector, which increases the resistance of the cell [177]. Just as with SEI formation, these reactions are accelerated at high temperatures and high cell voltages (low anode potential) [8]. Waldmann et. al. [125] also found that physical deformation caused by high cycling rates also resulted binder decomposition due to cracking of the anode and exposure to the electrolyte. Detection of binder decomposition is limited to X-ray diffraction, scanning electron microscopy, and comparing custom cells with different binder compositions [125, 176].

Metal dissolution can occur from the cathode material or from the cell current collectors. Current collector dissolution only occurs under extreme overcharge or over discharge [178, 179], and is thus out of scope. Dissolution of the positive electrode metal oxides is strongly dependent on the cell chemistry, with cathodes containing manganese being particularly vulnerable. At low voltage and elevated temperature, Mn dissolves into the electrolyte resulting in a loss of active material at the cathode [8]. For LFP cells, iron ions from the cathode can dissolve into the electrolyte and migrate to the anode, where they are reduced. The iron at the anode then catalyzes SEI formation reactions, increasing the cell's resistance and consuming active lithium. This is enhanced at temperatures of 55C. However, this is not a major degradation mechanism for LFP cells under normal operating conditions due to the general stability of LFP [180, 181]. Detection of this effect was achieved through X-ray diffraction, energy-dispersive X-ray analysis, Raman spectroscopy, and scanning electron microscopy.

4.3 Effect of Temperature Summary

Before investigating non-uniform temperature distributions in battery systems, the effects of uniform temperature distributions must be understood and then applied to the more advanced problem. The effect of elevated and reduced temperatures on the aging [33, 182–184] and performance [7, 15, 20, 65, 66, 69, 183–187] of LIBs is well documented in the literature and the effect on performance was discussed in Section 1.1 while the effect on aging mechanisms was discussed in Section 4.2.3. In general, higher temperature improve the performance of LIBs by reducing their electrochemical resistance, but also reduces the service life of the battery by promoting degradation mechanisms as discussed in Section 4.2.3. Conversely, lower temperatures may extend the lifetime of the battery, but reduce its performance. A summary of the effects of temperature on cell behavior and lifetime is provided in Table 3.

TABLE 3. The effect of increasing or decreasing temperature relative to $25°C$ on various battery parameters. References: a [15], b [16], c [17], d [18], e [19], f [20].

Parameter	High Temp	Low Temp	Refs
SoC	No Change	No Change	
SoH	SoH decreases faster	SoH decreases slower	a
OCV	Increases or decreases based on SoC	Increases or decreases based on SoC	b
Usable Capacity	Increased	Decreased	
IR	Decreased	increased	c
dS	Increases or decreases based on SoC	Increases or decreases based on SoC	b
dH	dH = dU + VdP. Since U and P increase, H increases	dH = dU + VdP. Since U and P decrease, H decreases	d
dG	Depends on sign of dS: dG = dH - TdS	Depends on sign of dS: dG = dH - TdS	
Diffusivity	Increases by Arrhenius relation	Decreases by Arrhenius relation	e
SEI	Increased SEI growth	reduced SEI growth	a
Lithium Plating	reduced Li-plating	increased Li-plating	f
Side Reactions	Increased side reaction rate	decreased side reaction rate	a

4.4 Formation of Non-Uniform Temperature Distributions

It is well established that temperature distributions naturally arise within both Li-ion cells and battery packs [15, 29, 65, 150, 182, 186–197]. For cells, the manner in which they form is dependent both on the cell geometry and the specific design of the components within the cell. For battery packs, it is dependent on the included cell, the battery module design, the battery cooling system

design, battery management system settings and packaging material conductivity. In practice, factors such as operating environment and usage pattern are also important.

4.4.1 Cell Internal Temperature Distributions

Temperature gradients have been observed to form in pouch and cylindrical cells. In pouch cells, the hotspot is located half way between the terminal tabs of the cell, and slightly above the center of the cell [22, 29, 189]. This distribution can be explained by the internal construction of the cell. Since the current must pass between the terminals, reactants nearer the terminals will be utilized first. Additionally, a longer distance from the terminals also implies higher impedance along the current collectors leading to an increased resistance and an effectively lower potential of the cell, resulting in lower localized current density and utilization of reactants [15, 20, 32, 65, 183–186, 195]. On the surface of a pouch cell, the change in temperature from this is in the range of $7°C$ [22], $10°C$ [29] to $14°C$ [189] depending on the C-rate. The temperature gradient through a pouch cell is even more extreme by a factor of 4.5 than the gradient along its surface since LIB cells are more thermally conductive in the plane of their electrodes than through them [22]. This leads to a high temperature at the center of the cell (in the through-plane direction) that spreads planarly within the cell more than to the surface of the cell, making it difficult to detect. For the temperature gradient measured by [189] of $14°C$ on the surface of the cell, [22] suggests that this implies a temperature gradient of $63°C$ through the plane of the cell from a 6C discharge.

For cylindrical cells, Fleckenstein et. al. [15] considered 18650 LFP cells cycled at high rates which measures the effect of the thermal conductivity of the cell on the formation of thermal distributions within the cell. They emulated the effect of non-uniform temperature within a cell by considering three parallel connected cells at different temperatures, and validated this setup using thermal modeling. Due to the internal heat generation of the cell, the center of the cell was found to be $19.5°C$ hotter than the outer edge on the cell after cycling at 8C for 2 hours. The non-uniform temperature resulted in current density distributions within the cell due to the lowered resistance of regions with higher temperature. The non-uniform current resulted in a non-uniform SoC distribution within the cell, which was determined to only equalize by 33% after allowing the

cell to rest. This result was ascribed to electrochemical hysteresis. They proposed that these issues would result in additional aging of the cells, but did not investigate further.

Waldmann et. al. [29] investigated the effect of cell design on the formation of temperature distributions within cells. They compared cylindrical and pouch cells, with models designed for high power applications and other models designed for high energy density applications. Temperature was monitored by thermal imaging cameras as well as thermocouples built into the cells. Cells were cycled at rates from 1 to 8C. Their results confirmed the radial temperature distribution for 18650 cells found by Fleckenstein et. al. [15], and indicated that a temperature difference of up to $10°C$ is formed in cells when discharged at the rates specified on their datasheets. Cells designed for high energy density were found to accumulate temperature differences three times higher than cells deigned for high power applications. This was ascribed to the thicker electrodes which allow for more active material to fit in the cell, but the increased resistance leads to more heat generation [198]. When the maximum temperature rise of the cells at a specified C-rate is considered as a function of their capacity, both high power and high energy cells followed the same trend. The following expression was developed to estimate the internal temperature of the cell based on surface temperature measurements

$$\Delta T = T_{Surf} - T_{center} \approx \frac{R \times c \times I}{C} \tag{36}$$

where C is the heat capacity of the cell, R is the resistance of the cell, I is the cell current, and c is a fitting constant. They also speculated on the effect on aging but did not investigate.

For cylindrical cells containing protective elements in one of their terminals, Robinson et. al. [190] observed that the additional resistance induced by these components resulted in a significant temperature increase at the terminal of the cell (cathode in their case) where the multi-component cell tab was located for discharge rates above $0.75°C$. This caused an axial temperature gradient in the cell that increased in magnitude both with discharge rate and discharge time up to $10°C$. On the other hand, for cylindrical cells that do not contain complex cell caps, the maximum

temperature gradient is experienced radially [29, 150, 199] due to the greater thermal conductivity and dissipation along the cell and at the metal cell terminals [22]. These temperature gradients can reach up to $36°C$ [150].

Osswald et. al. [20] demonstrated more thoroughly through experiment the non-uniformity of current within cylindrical cells by using EIS (100 mHz - 10 kHz) on modified cells with multiple current tabs along the length of the cell current collectors. They observed a strong dependence on signal transmissions though the cell with signal frequency, with lower frequency signals having lower attenuation. By performing the experiments at different temperatures, they found lower attenuation at higher temperatures. The attenuation can be related to the current distribution during different operational conditions of the cell and indicates that cell construction results in inherent current non-uniformity within the cell which in turn can lead to locally increased temperatures.

Brand et. al. [32] investigated the current distributions between parallel connected cells of differing capacity and resistance. However, as demonstrated by Fleckenstein et. al. [15] and Klein [17], these results are indicative of internal cell variations. The theoretical analysis presented demonstrates that when cells of the same capacity but different resistance are connected in parallel, the current distribution follows the standard current divider equation

$$I_n = I_{tot} \frac{R_{tot}}{R_n + R_{tot}} \tag{37}$$

until the unequal currents result in the OCV of the cells becoming unequal, which cancels out the effect in the long term. However, this results in a non-uniform SoC distribution between the cells (or within the cell), lowering overall energy density. This scenario corresponds to different regions of a cell being at different temperatures, distances from a current collector, or different states of degradation. When considering differences in capacity, initially the current between the cells is equal, but as the charge or discharge continues, the cell with lower capacity changes voltage more

quickly, resulting in a non-uniform current between the cells that can be described by

$$I_1 = I_{tot}\frac{C_1}{C_1 + C_2} \tag{38}$$

for a two cell system with capacities C_1 and C_2. This corresponds to regions of a cell being non-uniformly degraded. They also demonstrated that these scenarios are not unreasonable by testing the capacity and resistance of 172 brand-new cells of the same model and observing that the relative coefficient of variation (standard deviation divided by mean) of 0.72% capacity and 1.83% for internal resistance.

Erhard et. al. [69] developed a custom NMC pouch cell with 44 voltage measurement tabs at different locations around the cell to measure the voltage, SoC, and current distributions that arise within a cell. By cycling the cell between 0.1C and 2C and at $5°C$, $25°C$, and $40°C$, they found increased cell temperature resulted in decreased uniformity of current distribution and SoC distribution. This was attributed to the increased current collector resistance with increased temperature and to the reduced electrochemical resistance at higher temperature combining to increase the favorability of the reactions closest to the cell terminals. This resulted in an SoC difference of 1.3% across the cell. The temperature of the cell was kept constant by nature of it being a single-layered cell, but the non-uniform current observed would result in non-uniform temperature distributions in a standard cell. No conclusions about degradation of the cell were made.

In another work, Osswald et. al. [183] measured how cell temperature affected the current distribution within standard 18650 cells by the same method used in their previous paper [20]. Cells were cycled at 0.1, 0.5, 1, and 2C rates at 10, 20, 30, and $40°C$ to observe how the current distribution was affected by these conditions. During phase transitions of the graphite electrode (for example, transitioning from LiC_{12} to LiC_6, which causes a characteristic kink in the cell's voltage profile [34]), they observed a voltage difference between the two ends of the electrode of up to 16 mV (4.3% SoC) (at $40°C$, 0.1C) indicating that the local SoC along the electrode was not uniform. At $10°C$, this difference was reduced to 12 mV (1.1% SoC). The proposed explanation

for the increased SoC gradient in the cell at higher temperatures was the same as their previous paper, that as the electrochmeical resistance is decreased, the positive temperature coefficients of the current collectors has a larger effect on the performance of the cell. They also determined that C rates above 0.5C resulted in internal temperature gradients within the cell, but did not comment on the magnitude or effect of such phenomenon. Additionally, the cells were discharged in 5% SoC steps at a 1C rate with 150 minutes of rest between each discharge pulse. During the rest, the voltage along the electrodes was measured to determine how distance from the cell terminals affected relaxation of SoC inhomogeneities. This was repeated for ambient temperatures of 10, 20, 30, and $40°C$. It was found that for SoCs where the voltage curve is not flat, the SoC/voltage difference along the electrode equalized within minutes, but for flat regions of the SoC curve, equalization can take between 45-90 minutes.

Troxler et. al. [66] investigated the effect of temperature gradients on the short-term performance of pouch cells. A thermal gradient of up to $40°C$ was applied through the cell's face using Peltier elements. Under these conditions, EIS spectra of the cell were taken in the range from 0.1 Hz-10 kHz. The observed, as with many others, that the cell's internal resistance decreased with increased temperature as described by the Arrhenius equation, noting the ionic conductivity of the electrolyte as a major factor for this dependence. When a temperature gradient was applied to the cells, the EIS data showed a decrease in the cell's resistance compared to the tests performed at the cell's average temperature. Further investigation showed that the reduction in the diffusion resistance was larger than the reduction in the Ohmic resistance. The explanation for the lower total cell resistance when non-uniform temperature is applied to the cell follows from the parallel resistor equation where the effective resistance is lower than the lowest parallel resistor. Considering the layers of the lithium-ion cell as individual resistors, with the hotter layers have lower resistance, the observed results should be expected. As a result of this, following Equation 37, it is clear that internal current non-uniformities must also exist within the cell. However, testing was only done on cells under no load other than EIS.

The non-uniformities detected in above works indicate inherent non-uniform currents throughout lithium-ion cells, which are influenced by temperature, local cell potential, applied current, and cell design. These result in a non-uniform internal temperature profile of the cell, which in turn influence the internal current distributions. Since many aging processes are, as discussed in Section 4.2.3 are dependent on current and temperature, an investigation on the long-term effects of such distributions is required, and has been partially completed for the case of parallel connected cells, as discussed in Section 4.4.2.

4.4.2 Battery Pack Temperature Distributions

Electric vehicle batteries have become a focus in the literature in recent years, and one of the important areas of research is thermal management. Bruen and Marco [186] investigated how parallel connections between cells, when taking into account inherent cell inconsistency, in battery packs affect the performance of the battery system for electric vehicles. This was investigated through a combination of a novel equivalent circuit model that took into account parallel cell variations as well as cell interconnection resistance, and an experimental setup consisting of 4 18650 cells connected in parallel through shunt resistors to measure the individual current. The cell chemistry was unspecified, but based on the cutoff voltages listed, they were likely NMC cells. The cells were each aged to a different SoH in order to generate non-uniformity between the cells of up to 12.5% SoH, which is substantially larger than manufacturing differences [32], but is potentially illustrative of the effect on a degraded battery pack. Relative cell performance was characterized by the maximum current experienced by each cell as well as the total charge throughput of each cell as compared to if all cells were perfectly matched. For a HEV style cycle, it was found that the difference in cell resistance was the determining factor for each cell's contribution, whereas for deep cycling (or EV-style) usage, the change difference in cell capacity was the determining factor. For the HEV cycle, the least aged cell contributed 28.6% of all charge while the most aged cell contributed only 21.9%. Meanwhile, the peak current of the least aged cell 114.4% of the nominal value while the peak current of the most aged cell was only 91.5% of the nominal value. Together, these differences are likely to further increase the rate of aging of the battery pack. For EV-style

cycling, the charge throughput is more even, but the peak current was more erratic, with all cells at some (but different points) contributing to more than 100% of the nominal current. The most and least aged cells had the highest peak currents of 159.1% and 149.2% respectively. The fact that the most aged cell experiences the highest current is concerning for long-term battery health as this effect may serve to worsen the imbalance of cell SoH. This paper did not investigate the effect of temperature on these current distributions or vise-versa, but it is known that high currents affect cell temperature, so this can be expected to lead to non-uniform temperatures in battery packs.

Non-uniform temperature in a similar experimental setup was investigated by Yang et. al. [184]. They developed an electrochemical model to investigate how non-uniform temperature affected the degradation of parallel connected cells. This model was compared to experimental results from two 18650 LFP cells which were connected in parallel. The pack was cycled at a constant rate, similar to the "EV-like" case in [186], with similar results. However, here the non-uniform temperature applied to the cells ($\Delta T = 0°C$ to $12°C$) was the cause of the current distribution rather than different cell SoH. They also observed that the ambient temperature had an effect on the magnitude of the effect from the non-uniform temperature. When the ambient temperature was $5°C$ and $\Delta T = 12°C$, the two cells had an effective difference in capacity of 20%, where as when the ambient temperature was $25°C$, the effective capacity difference was reduced to 4%. Based on their simulation results, they determined that increasing ΔT results in increasing pack aging, with the pack aging nearly twice as fast with a ΔT of $12°C$ than with no ΔT. This was true for both an average temperature of the 5 and $25°C$, but the absolute degradation was three times higher at $25°C$ than at $5°C$. This lead the authors to conclude that battery thermal management systems should be designed to keep the temperature difference within battery packs below $\Delta T \leq 5°C$. However, their experimental investigation was primarily limited to parametrization of their electrochemical model, long-term experimental validation of the effect of thermal inhomogeneity is still required.

Additional modeling of non-uniform thermal performance in battery packs was provided by Wu et. al. [70]. They investigated the effect of interconnection resistance on non-uniform current

distributions and the effect on the thermal behavior of the battery pack. This was done through electrochemical modeling of a battery pack consisting of up to 12 cell connected in parallel while taking the interconnection resistance into account. They found that even for packs with uniform interconnection resistances between each cell, the cells closest to the pack terminals contribute the most current, and the effect scales linearly with the number of cells connected in parallel. The current mismatch was found to scale logarithmically with the ratio of interconnection resistance/cell resistance. For example, a pack with 8 cells in parallel and the interconnection resistance being 10% of the cell resistance, the cell closest to the terminals was found to contribute 220% more current than the cell farthest from the terminals. This situation is clearly not sustainable over an entire discharge, and was found to 'flip' as the cells closest to the terminals became discharged faster than the cells farther away. This suggests that real battery packs will almost always have significant current imbalances between parallel connected cells, and that the magnitude of these imbalances is strongly dependent on the physical construction of the pack. The thermal implications of this were also investigated, and it was found that the load profile was also a critical factor. For a load-profile consisting of narrow SoC discharge/charge windows or current pulses as might be expected from a hybrid vehicle, the current distribution always favored the cells closest to the pack terminals. This was sustainable because during the rest periods, the parallel cells self-equalized. As a result, the temperature of the favored cells increased much faster than the unfavored cells, achieving a ΔT of $5°C$ in only 16 minutes (1000 s). It should be noted that the rate of ΔT increase was still significant after 16 minutes, but their simulation did not continue for longer. A simulation using a real EV's dynamic drive cycle found that one cell with an unspecified "increased resistance" caused nonuniform heating of the pack of $\Delta T = 30°C$, with the maximum temperature of $70°C$, which was above the maximum operating temperature of the cell. The long-term degradation implications of this was not explored, but accelerated aging should be expected if the cells closest to the pack terminals experience over twice the current of cells farther away.

Karimi and Li [200] investigated how cooling system design affected the temperature distribution in EV battery packs consisting of pouch cells. Battery packs were modeled, with internal heat generation at the cell level based on current draw (Ohmic heating) and entropy effects. The

battery pack they considered consisted of 20 battery modules of 10 cells each. When natural convection air cooling ducts were placed between the modules, the pack temperature increased by $19°C$ in 24 minutes, with the cells directly adjacent to the cooling ducts about $1°C$ cooler than the cells at the center of the modules. Forced air, liquid cooling, and phase-change material (PCM) cooling were also considered. PCM was found to be most effective, followed by liquid cooling then forced air cooling. However, with increasing cooling effectiveness, an increase in ΔT in the battery pack was observed. A temperature difference of $15°C$ was found for PCM, $9°C$ for liquid cooling, and 2-$5°C$ for forced air. The center of the battery modules were not effectively cooled by any cooling strategy. Their results suggest that in order to maintain a $\Delta T \leq 5°C$ with liquid cooling, there should be cooling plates every 4 cells.

Pesaran [117] used NREL's ADVISOR vehicle simulator [201] to simulate EV battery pack thermal performance. A battery pack consisting of modules of 6 cylindrical cells each was modeled with forced air cooling. Cooling channels were considered in the spaces between each of the cells. A 'series' cooling system was evaluated where the intake air passed over each set of cells sequentially, as well as a 'parallel' cooling system where intake air was directed such that each cell received fresh intake air. The series cooling arrangement predictably resulted in a larger temperature difference within the pack of $18°C$ whereas the parallel cooling system saw a temperature difference of $8°C$, mostly from internal cell temperature differences. This result shows that cooling system design can induce large temperature differences within a battery pack.

Yang et. al. [37] investigated how the arrangement of cells in a battery pack can affect the temperature distribution and cooling system effectiveness. A thermal model was developed based on a standard single particle diffusion model with an integrated thermal model considering reaction heat, electrochemical + SEI resistance heat and Ohmic heat. This model was validated by performing experiments on a single cell. Battery packs/modules consisting of 60 cells were considered, arranged in 6x10 arrays. The two layouts considered were a grid of cells where the center of each cell was aligned with its neighboring cells in both the x and y directions and a staggered array where every other row of cells was shifted by half the distance between cell centers. For

the simulations, coolant air was forced into the pack along the long side of the pack. The grid array of cells allowed for a straight path for cooling air to flow through the pack between the cells, while the staggered array forced the air to flow around each cell. When discharging the pack at a 2C rate, it was found that the grid layout provided better thermal uniformity and lower cooling power requirement, while suffering from slightly higher maximum temperatures. For the grid array, the coolest cell (at the inlet) was $1°C$ cooler than the rest of the cells, which had a uniform temperature. For the staggered array, the second row of cells was the coolest, and the maximum ΔT was $2°C$. These temperature differences are small, but the design of the battery pack, with spacing between cells of 12mm, or 2/3 of the diameter of each cell, is extremely space inefficient and unrealistic in a real application. However, their results imply that at reasonable cell spacing, the arrangement of cells has a large impact on the thermal distribution within in the pack, and that no matter what layout is chosen, a temperature difference between cells will exist.

4.4.3 Effect of Non-Uniform Temperature on Battery Packs

In the works that inspired this, Klein et. al. [17, 31] investigated the effect of non-uniform temperature on cylindrical cells connected in parallel. A temperature gradient was applied to 5 cells using the device described in Section 7.4.4, and the current through each cell was measured using a shunt resistor. Current distributions were observed between the cells that became more pronounced at higher ΔT and, lower C-rate, and lower average temperature. Significant differences in cell behavior between pulse charge/discharge and prolonged charge/discharge were found. At different times during prolonged discharge, different cells contributed more current, and the points at which they switched were dictated by the graphite intercalation potentials. When applying a current pulse, the current distribution followed the cell resistance's dependency on temperature such that the hottest cell contributed the most current while the coldest cell contributed the least. The maximum current resulting from a ΔT of $20°C$ was 1.4 times the nominal current. At the end of discharge, the cells were found to have a non-uniform SoC of up to 13%. Despite this, a reduction of only 3% in usable energy from the pack was found. The results from their work suggest that in order to observe the largest effect, the average temperature should be low and ΔT should

be high. While they observed that a lower C-rate resulted in more current variations due to the more pronounced effect of graphite compared to the electrochemical resistance, for cells connected in series that do not have the chance to equalize their voltage, a higher current is expected to increase the difference. The non-uniformities observed can be expected to reduce the lifetime of the battery pack, both due to accelerated aging at higher temperatures and larger than expected current through each of the cells.

In the most relevant work, Chiu et. al. [33] developed a modified single particle model for simulating series connected cells with non-uniform temperatures that took into account SEI layer growth through reduced availability of Li, which was modeled by a time integral of an Arrhenius equation. The model was developed using data from 2 cells cycled at different temperatures. The model was run at 0.5C for 2000 cycles with ΔT of 0, 9, and 18° C and average temperatures of $34°C$ and $60°C$. The pack performance at the 2000th cycle was evaluated. They found a 3% lower capacity with a ΔT of $18°C$ than with no temperature difference when the average temperature was $34°C$, and 7% lower capacity with a ΔT of $18°C$ compared to no ΔT when the average temperature was $60°C$. However, given the presented method for modeling degradation, this is the difference that could be expected if the cells had been stored at different temperatures, then connected in series and cycled. Despite this, it shows the importance of fully understanding the effects of non-uniform temperatures on series-connected battery packs. Their experimental results consisted of cycling two cells, one at $25°C$ and the other at $55°C$ while connected in series. The degradation rate of this pack was compared to manufacturer data from the cells datasheet for cycling at $25°C$. An increased rate of degradation was measured compared to the case of $25°C$, but was not compared to the case uniform cycling or storage at $55°C$. This makes it unclear if the results indicate increased aging due to non-uniform temperature or simply the battery pack being limited by the weakest cell which in this case was the hotter cell due to its higher degradation rate. They did note that their experiment had to adjust for cell degradation, changing the voltage limits of the charge/discharge cycle. Improvements to this testing methodology are presented in Section 7.4.4. Other limitations of this study that will be addressed in this work include the testing of only 2 cells connected in series, lack of evolution of individual cell performance data over time, lack of

control cases, and attribution of degradation to different stressors and mechanisms.

5 Research Background and Relevance

5.1 Machine Learning

Much of the motivation for this work revolved around improving battery state estimation for battery packs. One of the most important states of a cell to track is the SoC. To this end, a neural network (NN) was developed to estimate the SoC of a cell under dynamic loading conditions (HPPC and US06 drive cycles) [202]. In this work, it was demonstrated that input pre-processing, specifically, classification of charge/discharge can improve neural network performance for battery state estimation [195]. By further studying the effect of temperature gradients on battery packs, the additional data could be used to improve the training methodology for the NN, improving the 'real-world' performance of the determination of individual cell SoCs in the battery pack with a temperature gradient applied to it. This improved training is highly important to make this technology viable in various applications, as the NN was only trained on data from cells tested at the same temperature. Meanwhile, it is rare for any battery to actually operate at a constant temperature, and therefore including temperature data as an input to the NN is critical future work that must be done to achieve practicality.

5.2 Second-Life Energy Storage

With the increasing market share of EVs, it is only a matter of time until a large number of batteries from these vehicles reach their retirement. Either from totalled vehicles, battery replacements, or after the vehicle is scrapped. Many of these batteries are still in usable condition when they are removed from the EV, and could serve to offset the demand for new battery production, which itself is not a 'green' process. Therefore, the California Energy Commission (CEC) provided UC Davis a grant to develop a prototype stationary energy storage system using batteries that had been retired from electric vehicles. This project involved the design, construction, and operation of a 274 kWh second-life energy storage system from used Nissan Leaf battery modules. To achieve this, over 1000 battery modules were tested for their SoH to determine which were usable, and an algorithm was developed to determine which cells could be connected together into modules.

During testing, it was found that the assumption made in most literature that cells are retired from their first life when their SoH reaches 70-80% was optimistic, and 60-70% is a more realistic expectation.

After the battery system was produced, it was installed at the Robert-Mondavi Winery at UC Davis as part of the winery microgrid research project [106]. This system was an early demonstration of large scale deployment of second-life electric vehicle batteries for energy storage in a commercial-type building and microgrid system [203–218]. At the time of publication, the system had been in operation for 2 years, but only the first year of operational data was analyzed. The system was shown to reduce peak time energy use by an average of 39% and achieved an average reduction in maximum peak-time demand of 60%. The system demonstrated the viability of using second-life EV batteries for microgrid, commercial, and industrial energy storage systems in terms of their performance. However, the system had not been operating for a sufficient amount of time to comment on battery degradation.

Most relevant to this work, due to the fact that this battery was second-life, and that it was installed in a shipping container with the HVAC unit on one end, temperature differences formed between the modules of the battery pack. These were measured by the 56 thermistors installed on each of the two strings of the battery. While not granular to the cell level, this was sufficient to measure temperature differences across the pack. At the low (C/5) charging and discharging rates of this climate-controlled system, the temperature between modules varied by $3-5°C$. Future work plans for this system involve dissembling it and re-testing the cells in the lab. This work will allow the temperature data to be compared to the degradation. This will provide real-world verification of the lab-scale research in this work. This research will also be valuable for future second-life battery systems by linking the internal resistance inhomogeneity to thermal inhomogeneity within the battery system and thus lifetime and degradation estimations can be made more accurate.

5.3 Parallel Cell Aging with Temperature Gradients

As an extension of [17], the available experimental setup was operated for an additional 500 cycles to observe the aging behavior induced by the non-uniform current distributions along with

non-uniform temperature of the cells. It was found that the shape of the current distributions while charging and discharging were both significantly altered over the set of cycles. The pack was cycled at temperatures equivalent to TG Pack 2 with temperatures from $26°C$ to $44°C$ After 500 cycles, the hottest cell still contributed more to the bulk of the discharge, while the coldest cell continuously contributed the least current to the pack. The absolute spread in current became greater, as might be expected due to uneven cell aging. After 500 cycles, the hottest cell initially contributed more current, but quickly fell off to allow other cells to accommodate the load compared to the first cycles where the hottest cell *increased* its share of the load until near the end of discharge.

5.4 Neutron Imaging of Electrically Abused Cells

For this work, a selection of NMC cells were neutron imaged before and after electrical abuse testing. Other testing performed on the cells included electrochemical impedance spectroscopy (EIS), cell disassembly, and X-ray computed tomography. A selection of cells was each chosen to be discharged to 100%, 110%, and 150% of their rated capacity. After the over discharge testing, cells were again subjected to the full array of testing that was done before over discharging. First, EIS showed very little increase in Ohmic resistance of the cells regardless of their over discharge status. However, the diffusion resistances of the cell discharged to 150% had increased by over 100x its original value. Neutron radiography showed that the absorption intensity of the over discharged cell had reduced by 13% compared to the cell discharged to 100% of its capacity. While the X-ray imaging showed no large deformation of the internal structure of the cell, it did reveal damage to the structure of the cathode. After disassembling the cell it was found that metallic copper had been removed from the current collector and deposited on the surface of the cathode. It was also determined that the thickness of the electrodes had increased by 21-26%. This lowering of the density of the internal cell structure may have been one of the causes of reduced neutron absorption, along with loss of active lithium to side reactions. Note that by over discharging the cells, lithium plating on the anode was avoided, as this would increase the neutron absorption even with lowered cell capacity and active lithium [219].

Part III

Research Methodology

The overall goal of the this work was to define how temperature gradients in battery packs affect their life-expectancy and performance over time. Since battery packs consist of cells connected in series and parallel, and the effect of temperature gradients on these two topologies of pack are different, both need to be investigated and compared. It is widely believed that temperature gradients will have a negative impact on the lifetime and performance of LIB packs, but few studies have been done to quantify them [15, 29, 65, 150, 182, 186–197]. Those that have do not study the evolution of the current dynamics and cell health over the lifetime of the pack [33, 66, 69, 183, 185, 190]. There are also multiple mechanisms by which applying a temperature gradient to a battery pack can degrade it, and these are again a function of whether the cells are in series or parallel. Some of these mechanisms have been individually studied, but some only as an aggregate, and almost always with different types of cells, which makes comparison and determining the influence of each aging mechanism difficult to isolate. Because more work has been done on cells connected in parallel, this contribution will focus on cells in series.

6 Cells in Series

The primary questions under investigation are how a battery pack consisting of cells in series that is exposed to a temperature gradient ages in capacity, performance, and how it is different from single cells and constant temperature battery packs. To answer these, the possible aging mechanisms must first be discussed in the context of series cells at various temperatures and the question broken down into more specific terms. Different aging mechanisms and magnitude of aging is expected to be induced across the battery pack. Aging results in lower overall pack capacity and power capability since cut-off voltages are reached sooner due to the weakest cell in the pack [33]. Some additional questions are: is aging of series cells with a temperature gradient the same as aging cells at different temperatures independently, and how different is the aging resulting from temperature gradients compared to series cells that have naturally mis-matched internal resistance?

To assess whether temperature gradients in a series battery pack are indeed distinguishable from the effect of temperature on individual cells, we consider the behavior of cells when in a series battery pack. When in series, the capacity of the battery pack is limited by the weakest cell, since when the cutoff voltage of that cell is reached, all cells must stop discharging. This can occur either because the cell has a high resistance, or because the capacity of the cell is lower than other cells. When cycling cells independently at different temperatures, the full usable capacity of each cell is used. For new cells in series, the performance of the battery pack will be limited by the coldest cell as it will have the highest resistance and the fastest lithium plating. This means that the warmer cells have a lower effective DoD because their usable capacity is higher, which aids in preserving their lifetime. On the other hand, the warmer cells have a higher rate of side-reactions that consume their active Li, which acts to shorten their life and increase internal resistance. Therefore, cells connected in series should have different aging behavior as a result of temperature gradients than simply cycling them independently at different temperatures.

Due to different aging mechanisms at the coldest and the warmest cells, both the magnitude of the temperature gradient and the average temperature of the battery pack were expected to change the aging behavior of the cells and the pack. At very low average temperatures, the coldest cell is likely to age more quickly than any other cell due to lithium plating and being cycled through its full DoD, while the other cells are warmer (but not hot), and not cycled as intensely. At intermediate average temperatures, the aging of the hottest and coldest cells may be similar, while the aging of the central cells could be reduced due to operation at optimal temperatures and low DoD. Finally, higher average temperatures will likely result in the hottest cell aging fastest, but providing the best short-term performance. The cycle at which the hottest cell begins to perform worse than the average temperature cell marks the point at which the degradation due to temperature has reduced the pack's performance compared to a homogenous temperature pack. When this will occur is unknown and likely differs between magnitudes of temperature gradient, average temperature, and cell chemistry [33, 126].

To determine how detrimental temperature gradients are to the lifetime of a series-connected battery pack, it should be compared to common cases of uniform temperature. The control pack is a pack of series cells that have (nearly) identical resistance and capacity, which is the ideal case for a series connected battery pack. Since temperature gradients modify the internal resistance of the battery pack, they should be compared with a battery pack that naturally has different internal resistances, as well as cells individually cycled at different temperatures.

The ideal control battery pack should have the longest life time and the best performance owing to its well matched cells that are exposed to the same conditions. The case of homogenous temperatures but inhomogeneous internal resistance is likely to generate natural temperature gradients which will result in an equalizing of internal resistance of the pack. However, these temperature gradients will then modify the aging behavior of the pack compared to the control case in addition to having lower maximum power output due to higher resistance. The cells with the lowest resistance in the battery pack are likely to age slower than the high resistance cells, since the high resistance cells will reach the minimum and maximum voltages sooner, reducing the cycling DoD range of the lower resistance cells.

SoC imbalance is an important factor in series connected cells as it causes the total battery pack capacity to be limited by the weakest or lowest SoC cell. This is expected to be induced by temperature gradients due to uneven aging of the cells in the pack. For second-life cells, this exacerbated due to initially different capacities. To counteract this, the BMS must perform additional balancing. However, traditional balancing methods do not enable the use of the full capacity of the battery. To do that, active balancing techniques will be required, which adds cost to the BMS. However, if it is known that a battery pack will be regularly subjected to temperature gradients, the additional cost of the BMS to implement active balancing may be offset by the extended useful life of the battery pack.

Station	Number of Channels	Max Voltage (V)	Max Current (I)
Station 1	12	10	30
Station 2	2	5	100
Station 3	2	5	50
Station 4	2	5	20
Station 5	3	20	5
Station 6	2	20	20

TABLE 4. List of battery test station capabilities used during the experiment. All test stations were from Arbin Instruments.

7 Experimental Methods and Setup

7.1 Cell Specifications

The cells studied were LFP cells (AA Portable Power Corp model LFP-18650HT) [14], with a rated capacity of 1500mAh at 0.5C. These were the same as the cells used by Klein [31]. These cells were rated for 2.5-3.65V, with a nominal voltage of 3.2V. The rated maximum continuous charge current was 1C, but the recommended charge was 0.5C with a charge cutoff current of 0.01C, and the max rated continuous discharge current was 3C, with a pulse discharge rating of 10A (6.6C) for 10 seconds. The nominal internal resistance was $45m\Omega$ and the cycle life was quoted at 2000 cycles at 100% DoD. The operational temperature range of the cells was 0-55° C for charge, and -20-60° C for discharge. Table 2 shows the rated capacity change of the cells at different temperatures [14].

7.2 Battery Tester Specifications

Cells were tested using several variations of Arbin BT2000 battery test stations. The differences between the test stations being their rated voltage range and maximum testing current. For the experiments performed in this work, the current of the test stations was not a limiting factor. But due to the increased voltage of series connected cells, care had to be taken to stay within the safety limits of each test station and only one station was capable of testing the series packs. The critical specifications of each tester are listed in Table 4.

7.3 Characterization Testing

Characterization tests of the cells were performed in order to identify each cell's internal resistance, capacity, and voltage as a function of SoC and temperature. The purpose of these tests was to gain a full understanding of the cells when new, to gather data about cell consistency, and to allow for monitoring of changes in cell performance parameters throughout the course of the study. It also provided the data needed to match cells together into groups that were as similar as possible such that any differences in resistance or capacity during the following experiments could be attributed to the conditions of the experiment. Not every test was run on every cell to reduce experimental time. Instead, a representative sample of five cells was selected for each test based on their capacity or total 10-second internal resistance. After the cycling and degradation tests, the tested cells were compared to the fully characterized cell that was the closest match for its initial state.

7.3.1 Custom Single-Cell Holder

In order to ensure consistency of measurements, a cell holder assembly was constructed for single cell testing that applied a replicable pressure to the cell terminals. It has been shown that connection quality to the cells can greatly affect resistance measurements and hurt cell characterization accuracy [32]. The holder, shown in Figure 17 utilized a spring to maintain a controlled contact pressure. The compression distance of the spring was set by an M6 x 12mm screw and a set of three washers. The fixture was designed to only allow the screw to be tightened to the correct position, thus preventing over or under compression of the spring, even if the torque applied to the screw was inconsistent. The spring used was McMaster-Carr part number 9657K325, which had a length of 1", a maximum compression length of 0.6", and a spring constant of 36.78 kN/m (210 lbs-force/in). The screw and washers were calibrated to compress the spring by 1.7 mm, with $F = 36.78N/mm \times 1.7mm = 62.5N = 14.1lbs - force.$

Connections to the battery test stations were made by inserting approximately 1.5 in long, 1/16 in thick, and 3/4 in wide busbars into the fixture at each end of the battery as shown in Figure 17. Copper foil was then placed between the cell terminals and the busbars. The spring compression

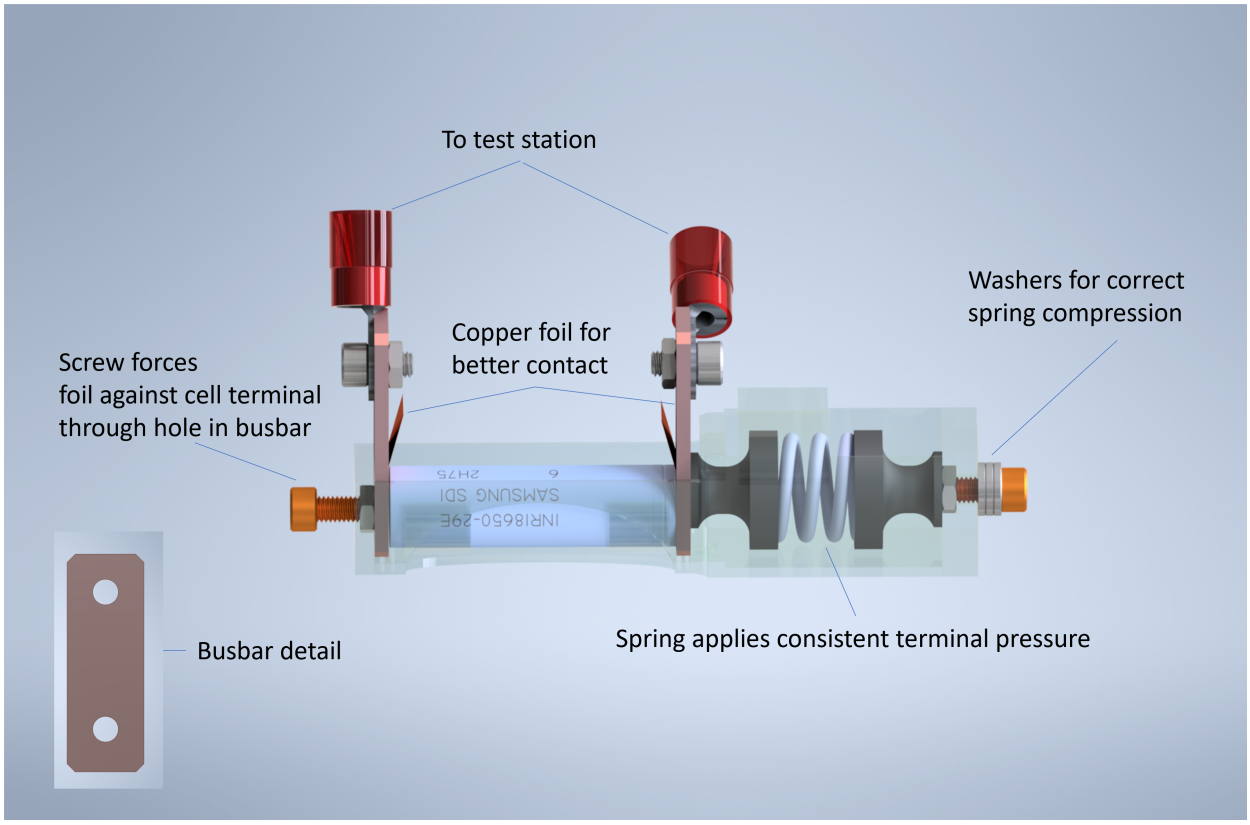

FIGURE 17. A rendering of the single cell holder using spring for terminal compression with callouts for important features.

screw (right side in Figure 17) was then tightened to compress the spring to the desired force. The screw on the left side of Figure 17 was finger tightened just enough to press the copper foil against the cell terminal by passing through one of the holes in the busbar. The battery test station ring terminal connectors were than attached to the exposed portion of the busbars.

The effectiveness of the cell holder was verified by repeating the same internal resistance measurement 5 times on 10 cells, removing and replacing each cell between each test. A precision of $\pm 0.2 m\Omega$ was obtained, compared to the measured resistance values of $\approx 57 m\Omega$. In addition, these measurements can be compared to those obtained by Klein [17] for the same cells, showing that the cell holder reduced the measured resistance for the same cells by $\approx 40\%$.

7.3.2 Cell Capacity Test

The cell capacity test was designed to be a simple check of a cell's basic capacity and internal resistance to serve as a comparison between each cell. This test was used for choosing which cells to group together, and served as the benchmark test for cell degradation. The test assumed that the cells start at 50% SoC, as all test schedules ended by charging or discharge the cells to 50%. The test schedule consisted of the following sequence:

1. Rest for 1 minute.
2. A charging current pulse of 3A for 10 seconds with a data collection resolution of 0.05 seconds. This measures the charging internal resistance of the cell.
3. Rest for 5 minutes.
4. Discharge at 3A for 10 seconds with a data collection resolution of 0.05 seconds. This measures the discharge internal resistance.
5. Rest for 10 seconds
6. CCCV charge as specified by datasheet (see Section 7.1).
7. Rest for 1 hour.
8. Discharge at C/2 down to 2.5V. This is the rate at which the datasheet provided the most information.
9. Rest for 30 minutes
10. Charge as recommended by datasheet (Section 7.1).
11. Rest for 1 minute
12. Discharge to 50% SoC.

A sample capacity test is shown in Figure 18. The initial charging and discharge pulses are used to measure the resistance of the cell at around 50% SoC (steps 1-5). The initial charge (step 6) is used to get the cell to a known 100% SoC to allow for accurate measurement of the cell's capacity. During the one hour rest (step 7), the voltage reduces even though the current is 0 A. This is caused by the cell relaxing back to OCV after charging. Steps 8-10 are the full discharge-charge cycle and are used to get the measurement of capacity to calculate the SoH of the cell. Finally, step 12 simply discharges the cell to approximately 50% SoC. From this test data, each cell's Coulombic efficiency (Equation 32), energy efficiency (Equation 31), charge capacity, discharge capacity, 50%

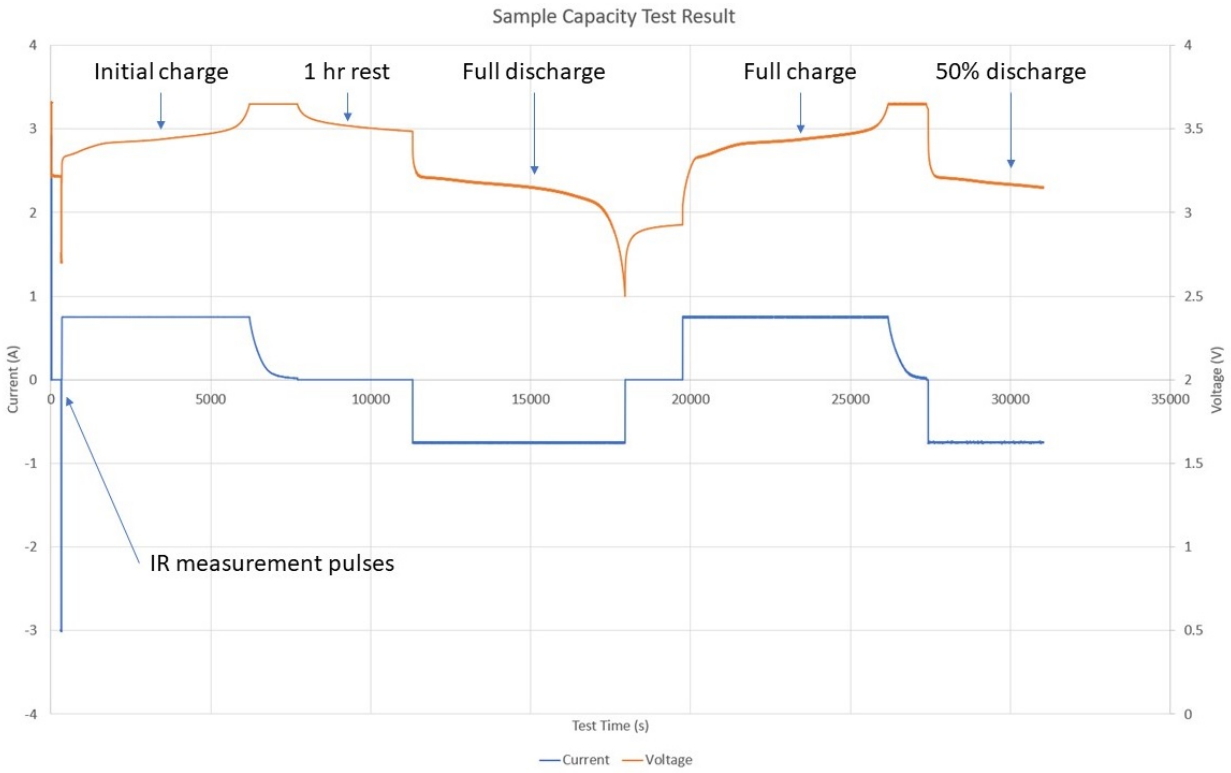

FIGURE 18. Example capacity test showing the current and voltage of the cell during the test. Each section of the test is called out.

SoC charge and discharge internal resistance, 100% SoC discharge resistance, and 0% SoC charge resistance was measured. This test was performed on all cycled cells after every 200 cycles to track their capacity as they aged.

7.3.3 Cell Capacity Characterization Test

This test was used to measure the capacity of the cells across different C-rates. It performed cell capacity measurements at C/60, C/10, C/5, C/2, 1C, 1.5C, and 2C. The capacity test performed at C/60 was used to define the 'true' OCV curve of the cells by taking the average of the charge and discharge voltage at each SoC. The test consisted of the following:

1. Rest for 1 minute
2. Charge to 100% SoC as recommended by the datasheet (Section 7.1)
3. Rest for 1 hour

4. Discharge at specified C-rate to 2.5V.
5. Rest for 1 hour
6. Charge at specified C-rate, with CV charge as specified by datahsheet.
7. Repeat steps 3 to 6 for each C-rate.
8. Discharge cell to 50% SoC.

This test allowed for a complete capacity map of the cell at different C-rates to be generated, and the change in this map to be tracked as the cells degraded.

7.3.4 Cell Internal Resistance Characterization Test

This test was used to measure the internal resistance across SoC and temperature of the cells. The charge and discharge resistance was measured every 10% SoC and repeated at $5°C$, $10°C$, $20°C$, $30°C$, and 50 $°C$. The test was performed as follows:

1. Rest for 1 minute
2. Charge to full according to datasheet specifications (Section 7.1).
3. Rest for 5 hours (as suggested by [40]).
4. Apply discharge pulse of C/5 for 10 seconds, with data recorded every 0.05 seconds. C/5 was chosen to be consistent with Klein's methodology [17].
5. Rest for 5 minutes
6. Apply charge pulse of C/5 for 10 seconds, with data recorded every 0.05 seconds.
7. Rest for 5 minutes.
8. Discharge 150mAh (10% SoC) at C/5. This step was corrected for the measured SoH of each cell as the cells aged to maintain 10% SoC increments.
9. Rest for 10 minutes.
10. Repeat steps 3-9 until SoC = 0%.
11. Charge to 50% SoC.

This test was repeated at each temperature specified above. The result was a map similar to the capacity characterization test, except the internal resistance was mapped against temperature and

SoC and allowed for another degradation effect to be tracked in detail.

7.3.5 Cell dOCV-dT Test

This test followed the methodology of [16, 17, 40, 220] to measure temperature effects on the OCV of the cells. In this test, the cell was brought to a specified SoC, allowed to rest until it reached equilibrium, then the following temperature profile was applied: $45°C$, $25°C$, $5°C$, $25°C$, $45°C$, resting at each temperature for 2 hours. The SoC was then incremented by 5% and the process repeated. The purpose of this test was to characterize the entropy of the cells and provide corrections to the voltages for changes in the OCV measured during other tests and is not intended to measure degradation, though some changes due to aging were expected [7]. The test followed the protocol:

1. Rest for 5 minutes at $25°C$.
2. Charge cell to full using datasheet specified method at 25 $°C$.
3. Rest for 5 hours at $25°C$.
4. Rest for 2 hours at $45°C$.
5. Rest for 2 hours at $25°C$.
6. Rest for 2 hours at $5°C$.
7. Rest for 2 hours at $25°C$.
8. Rest for 2 hours at $45°C$.
9. Rest for 30 minutes at $25°C$.
10. Discharge 5% SoC at $25°C$ by removing 75mAh. This step was adjusted based on the SoH of the cell to maintain 5% SoC increments.
11. Repeat steps 3-10 until SoC == 0%.
12. Charge to 50% SoC at 25 $°C$.

7.3.6 Neutron Radiography Imaging

Neutron Radiography (NR) uses a beam of neutrons generated by a nuclear reactor to image a sample. The sample is placed in the neutron beam in front of an imaging plate as shown in

Figure 19. As different materials in the sample absorb different amounts of neutrons, the intensity of the transmitted neutron beam on the imaging plate produces a 2D monochromatic image of the sample. The intensity of the transmitted neutron beam is given by the Lambert-Beer attenuation law

$$I = I_0 e^{\mu t} \tag{39}$$

where I_0 is the intensity of the beam incident on the sample in $\frac{neutrons}{s \cdot cm^2}$, μ is the neutron absorption cross-section of the material in cm^2, and t is the thickness of the material in cm. [11].

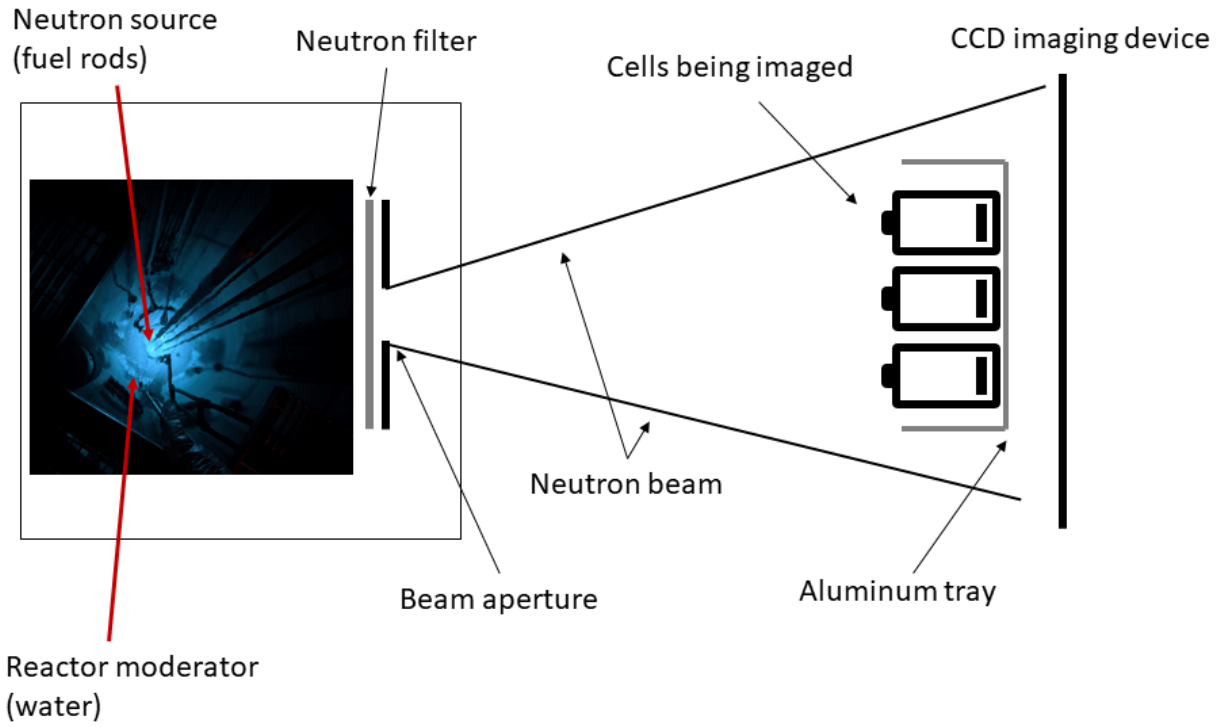

FIGURE 19. Figure showing the reactor core and a diagram of a typical neutron imaging experimental setup. Diagram based on figure from [11].

NR is especially well suited for imaging lithium ion batteries due to the high neutron capture cross section of Lithium compared to other cell components such as aluminum and copper. The

neutron beam attenuation coefficient for lithium is $6cm^2/g$ while for copper and aluminum it is 0.03 and 1 cm^2/g respectively [221]. This made it especially valuable to inspect cells that were cycled at low temperature as they were expected to exhibit increased lithium plating and lithium dendrite formation. Same et. al. clearly showed that the increased attenuation due to lithium plating can be seen in in neutron images, especially after the cell was over charged [168]. Since NR is non-destructive, it can be performed on a cell multiple times after various experiments have been conducted on the cell to observe otherwise unobservable changes to the cell. These include, in order of the magnitude of their effect on neutron beam attenuation, detecting Li dendrite growth [168], quantification of remaining active lithium in the cell electrodes [222], detection of lithium consumed by the SEI [219], finally electrolyte consumption, distribution, and gas formation [221, 223]. It has also been found that cell SoC produces visible changes in the imaged intensity in NR images [224].

For this work, NR was performed in Bay 3 of the UC Davis McClellan Nuclear Research Center (MNRC) in Sacramento, CA [225]. This facility is equipped with the highest power Training, Research, and Isotope Production General Atomics (TRIGA) reactor in the United States, at 2MW continuous operation. These reactors use uranium-zirconium hydride fuel rods [226], which have a self-cooling property that prevents nuclear meltdown. The beam intensity in Bay 3 of the MNRC is $10^7 N/cm^2 s$, and has a spacial imaging resolution of $100\mu m$, which unfortunately was insufficient to distinguish the layers inside the cell, which were on the order of $50 - 100\mu m$ thick [227]. The images produced by the detector provided a total resolution of 3520x4280 pixels. Cells were placed in an aluminum tray 3.175mm (1/8in) thick, with dividers also made of 3.175mm thick aluminum plates. The direction of the beam was always through the tray which was oriented to account for the 20° beam angle such that the beam was normal to the cells. The cells were initially imaged both laying down in the tray as shown in Figure 20 and vertically along the cell axis as shown in Figure 41. The cell terminals were tapped with paper masking tape to prevent shorting through the aluminum tray. This tape is highly transparent to neutrons as can (or rather, can't) be seen in Figure 38, where it is only visible when neutrons pass through the length of the tape. To avoid the effect of SoC on the NR images, all cells were CCCV charged to 3.29V for 2 hours before imaging. NR imaging was performed before cycling testing, but after initial

characterization testing, and after all cycling at the conclusion of the experimental phase.

FIGURE 20. Image showing a sample of the cells in an NR imaging tray. For through-axis images, cells were taped to the divider to be held vertically in the tray.

7.4 Cycling, Aging, and Degradation Testing

7.4.1 Control Tests

To determine the effect on pack and cell lifetime caused by non-uniform temperatures, a selection of cells was aged under various conditions. These included the packs subjected to non-uniform temperatures, a control pack, individually cycled cells, and calendar aged cells. To account for the amount of time taken up during the experiment, the effect of calendar aging on the cells had to be accounted for. Calendar aging for storage at 65% SoC occurs at a rate of $\approx 0\%$ per year at a storage

temperature of $30°C$ and 15% per year for storage at $45°C$ for LFP cells. [121]. These degradation rates suggested that, especially for the higher temperature cells, calendar aging would play a part in the overall capacity loss during this experiment. Thus, the first control group consisted of 9 cells, 3 each stored at temperatures of $5°C$, $20°C$, and $45°C$. These cells will be periodically tested using the cell capacity test to determine their aging behavior. Their storage SoC was 50%. These cells were used to determine the base aging expected from the cells degraded in other ways.

Another set of cells were cycled individually to act as a control against which the series-connected packs could be compared. This consisted of two groups of cells cycled independently at $20°C$ and $45°C$. It was initially planned to also cycle 3 cells individually at $5°C$, however this was not possible due to availability of lab equipment. A comparison of the collected data with literature was used to extrapolate the results to $5°C$. The three cells for each temperature were chosen based on their capacity and internal resistance, with one each of: high resistance with low capacity, average resistance with average capacity, and low resistance with high capacity. This test's goal was to isolate the difference between the basic effect of temperature on cycling aging of LIBs compared to the effect of being connected in series while exposed to a temperature gradient. While these experiments were not novel, (e.g. [123]), each cell make and model behaves slightly differently. However, they obey the same patterns, which allowed for the lack of $5°C$ testing to be easily compensated for.

The second control group was a series-connected pack of 5 cells, equivalent to the packs with non-uniform temperatures. This pack, referred to as the *ideal pack* represented an 'ideal' battery pack by having internal resistance and capacity within 1 standard deviation of the distribution measured by the characterization tests. The ideal pack was cycled with no temperature gradient, and an average temperature of $20°C$. It was cycled using the same cycle test (described below) as the packs with non-uniform temperatures. A separate fixture was designed for this pack as there was no need for the complex heat transfer and control system associated with the non-uniform temperature packs. This fixture is shown in Figure 21. It consisted of 3D printed brackets that held a copper busbar surrounded by copper foil. The copper foil, as with the single cell holder,

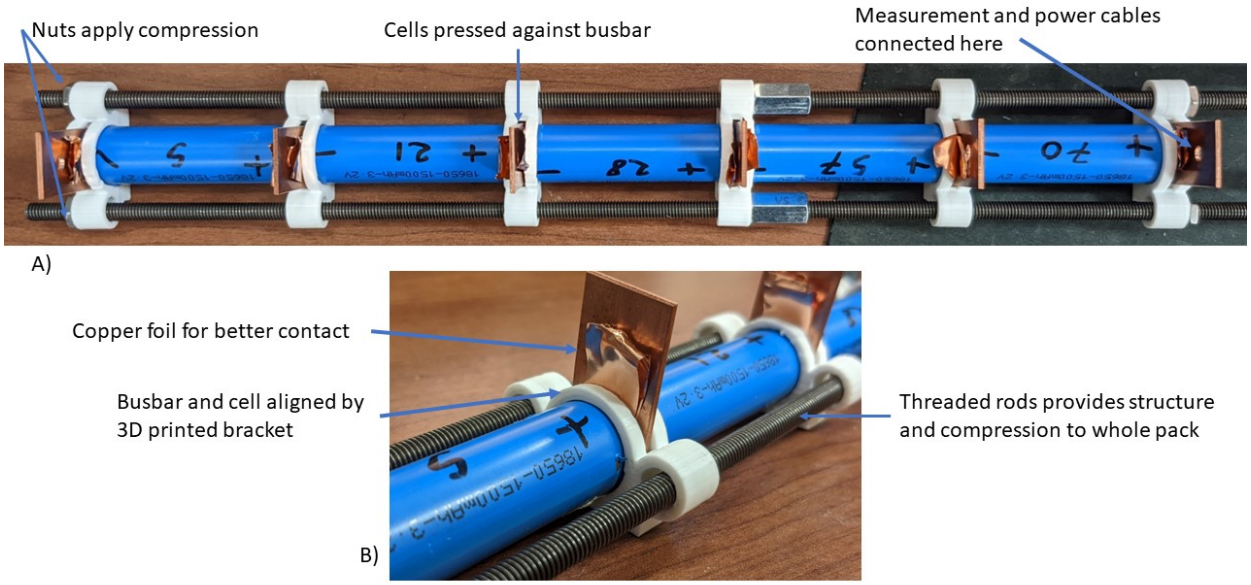

FIGURE 21. Picture of ideal pack fixture. A) Overview of fixture. B) Detail of fixture bracket.

was required to enhance contact between the busbar and the cell. The bracket was held in place by a threaded rod, which was also used to compress the pack to maintain its structure and force the cells into contact with the copper foil. Voltage measurement wires were then connected to each busbar to allow for measuring of every cell's voltage using the same system as that described below for the temperature gradient packs. The two busbars at the positive and negative terminals of the pack were also connected to the Arbin test station to cycle the pack. The goal of this pack was to provide the baseline for how a typical series battery pack would be expected to age while cycling in ideal conditions. By comparing to the packs with temperature gradients applied, the magnitude of the effect of the temperature gradient, compensated for by calendar aging, was determined.

7.4.2 Packs with Temperature Gradient

The main experiment was performed on two packs of 5 series-connected cells, collectively referred to as *TG packs*. These packs were subjected to a $17°C$ temperature gradient with average temperatures of $12°C$ and $35°C$. The first pack, referred to as *TG1* was cycled with an average

temperature of $12°C$, with the minimum and maximum temperatures being $3.5°C$ and $20.5°C$ respectively. The second pack, *TG2*, was tested with an average temperature of $35°C$, minimum of $26°C$, and maximum of $43.5°C$. These temperatures were chosen as they cover the majority of conditions under which LIBs are cycled 'in real life'. While not reaching the extremes ($0°C$ and $65°C$) for safety reasons, these temperatures should provide useful reference for most realistic conditions. The goal of these experiments was to measure the effect of temperature gradients on series connected battery packs, and investigate the effect of different average temperatures on the performance of the pack and the aging mechanisms of the warmest and coldest cells of each of the packs as described in section 6. While a ΔT of $17°C$ may appear large, experiments have shown that even a modest C/2 rate can result in ΔT's of up to $10°C$, therefore it was considered reasonable that a higher rate pack may experience larger temperature differences given that heat generation is proportional to the current squared [228].

7.4.3 Cell Matching Methodology

The cells that were used in each of the TG packs were selected based on data from the characterization tests (see Table 5). The objective was to match them together with cells that were as similar as possible such that any differences in resistance or capacity during the experiments could be attributed to the conditions of the experiment. This was done by first calculating the z-score for both the capacity and resistance of all the cells.

$$Q_{norm} = (Q_i - \bar{Q})/\sigma_Q \tag{40}$$

where Q_{norm} is the z-score of capacity, Q_i is the capacity of the i'th cell, and σ_Q is the standard deviation of the capacity. The same calculation was performed on the internal resistance. Next, every possible combination of 5 cells was found. For each group of cells, the mean (normalized) value of capacity and internal 0.1 second resistance at 50% SoC was calculated. Then the mean squared error of the group's capacity and resistance z-scores from their mean values was taken.

Specifically,

$$MSE_{capacity} = \frac{1}{5}\sum_{n=1}^{5}(\bar{Q} - Q_n)^2 \tag{41}$$

where $\bar{Q}$ is the mean capacity z-score of the group of 5 cells, and Q_n is the capacity z-score of cell n. The internal resistance MSE was calculated similarly. Then, the MSE of the internal resistance and of the capacity were summed together. The normalization by z-score meant that each cell in these groups had resistance and capacity as close as possible to the mean values of each, and by minimizing the MSE of the cell group, the groups with the most similar cells were chosen. Therefore, the cell groups with the lowest total MSE were taken to be the ideal pack, and TG packs 1 and 2.

7.4.4 Testing Fixture (Temperature Gradient System)

The Temperature Gradient System (TGS) was built by Matt Klein [17], and consisted of machined aluminum blocks that were compressed around cylindrical 18650 type LIBs. The blocks held a row of 5 cells. Each cell had a type-K thermocouple with $\pm 1°C$ measurement error attached, with the cells on either end having two. The temperatures of the first and last cells were taken as the average of the two thermocouples. Temperature differences across the pack were generated in the aluminum blocks by 24V thermoelectric Peltier elements at each end of the blocks. Thermocouples were also placed near the Peltier elements and connected to a TE-36-25 temperature controller to maintain the set temperature. To maximize the thermal contact between the cells and the aluminum, thermal interface material paste (Cooler Master IceFusion) was applied to the cells and to the Peltier elements. The setup is shown in Figures 22 and 23. Insulation was then placed on the end plates to reduce unwanted heat transfer. Using this setup, linear temperature profiles could be generated of the form

$$T(x) = \left(T_{avg} - \frac{1}{2}(T_6 - T_0)\right) + \frac{x}{L}(T_6 - T_0) \tag{42}$$

Where L is the length of the aluminum blocks and the average temperature of the entire battery pack was calculated as

$$T_{avg} = \frac{1}{N_{cells}} \sum_{j=1}^{N_{cells}} T_{cell_j} \tag{43}$$

Finally, the total pack temperature difference was taken as the difference between the warmest and coldest thermocouples. $\Delta T_{pack} = T_6 - T_0$. The system was capable of generating $\Delta T = 17°C$ at a variety of T_{avg} covering the safe operational temperatures for LIBs. The entire fixture was placed in a temperature controlled chamber which allowed for a wider range of average temperatures to be applied to the cells. The maximum root mean squared error of applied temperature vs. measured temperature profile for this setup has been determined to be $0.9°C$ [17].

The original configuration of the TGS was designed for connecting the 5 cells in parallel. To convert the TGS to a series-connected battery pack, voltage measurements for each cell had to be added. This was done by welding nickle strips to the cell terminals to provide connection points for both series connections and voltage measurement connection. The cells were then connected in series by alligator clip wires. Voltage measurement connections were made at both terminals of each cell; this configuration prevented voltage drops along the series connections from affecting the cell voltage measurements. The voltages were measured by a National Instruments NI 9205 analog input module as shown in Figure 24. The 9205 can measure 16 differential voltage pairs, at 10V per measurement with 16bit precision and a sample rate of 250kHz. The absolute voltage measurement accuracy was 6.23mV, with standard deviation of signal noise of 0.240mV, and a sensitivity of 0.096mV. LabView was used to record the cell voltage data at 15 Hz.

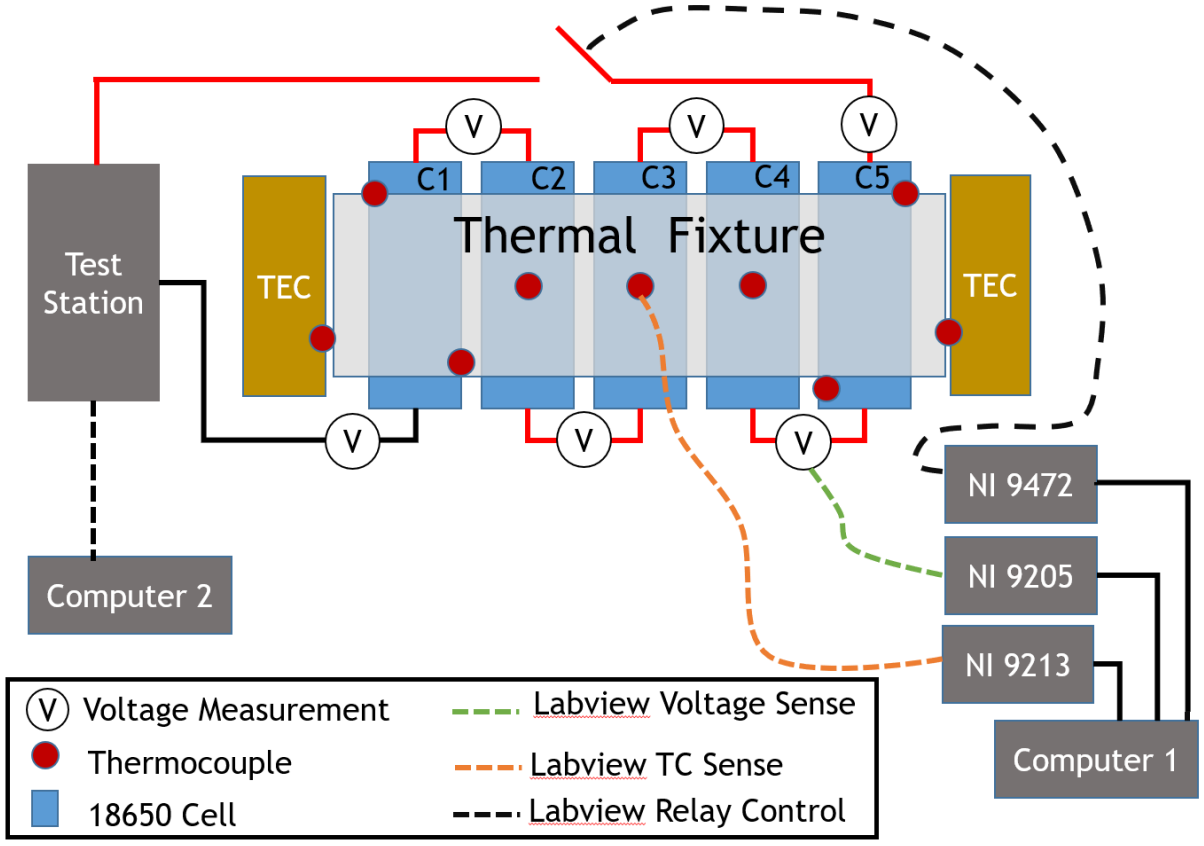

FIGURE 22. Diagram showing the test rig, location of thermocouples, thermoelectric elements, and data collection devices.

Another problem caused by conversion to a series battery pack was that the Arbin battery test station could only measure the pack terminal voltages. However, charging or discharging had to stop when any single cell reached its cutoff voltage otherwise safety issues could occur. Since it was entirely possible for the pack voltage to be within the safe 12.5-18.25V while a single cell was outside of its safe 2.5-3.65V range, a secondary safety mechanism was required. This took the form of placing a relay in series with the battery pack that was controlled by a National Instruments 9472 digital output module as shown in Figures 25 and 26. This relay was triggered to disconnect the pack from the test station when any cell's voltage exceeded the minimum or maximum voltage limit, as measured by the NI 9205. Typically, this would cause a battery test station to enter an error state and stop the test. To get around this, the Arbin was set to enter a rest state rather than an error when the voltage exceeded the normal limits, it would then wait until a normal voltage was

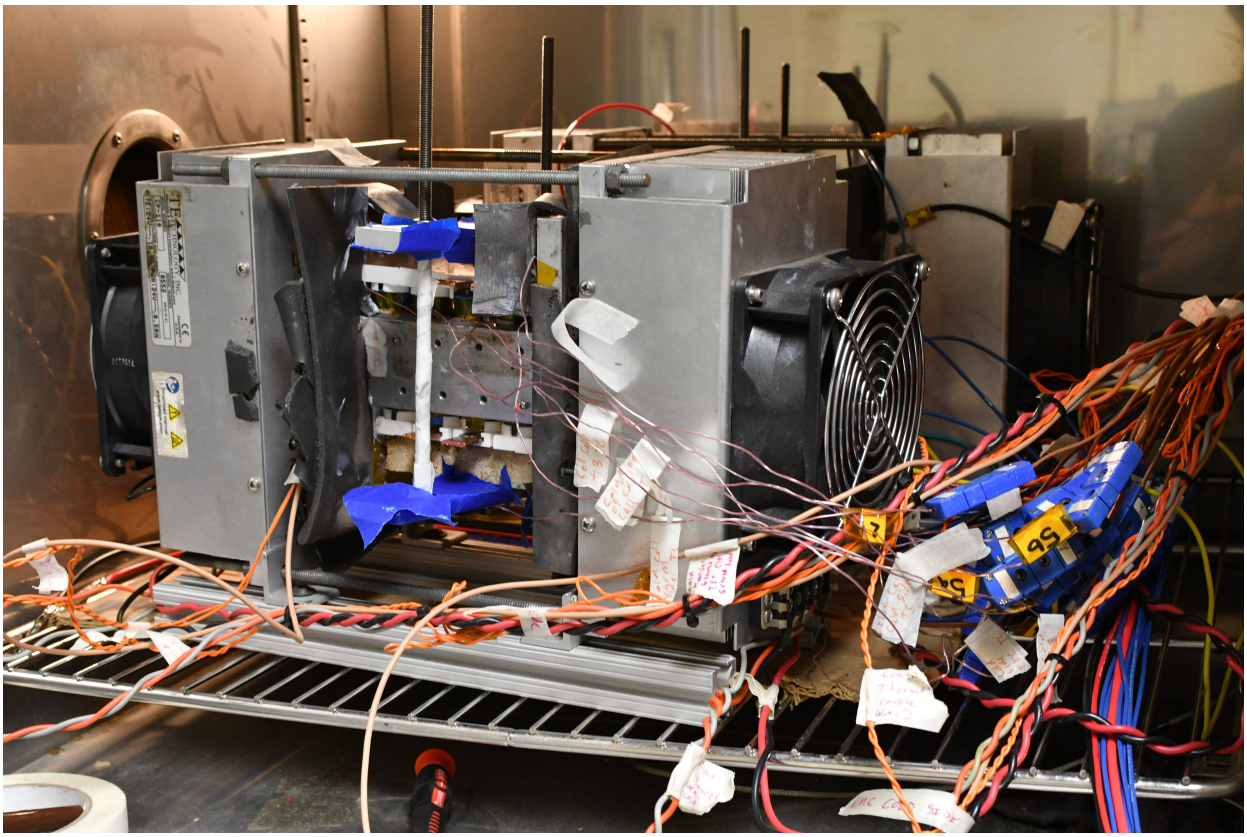

FIGURE 23. Picture showing the test fixture located in the thermal chamber before testing.

measured again before continuing the test. After 5 seconds, the relay would close again, restoring the connection between the battery pack and the test station. This method did not compromise system safety because if a cell's voltage remained outside of the safe range, the relay would not close.

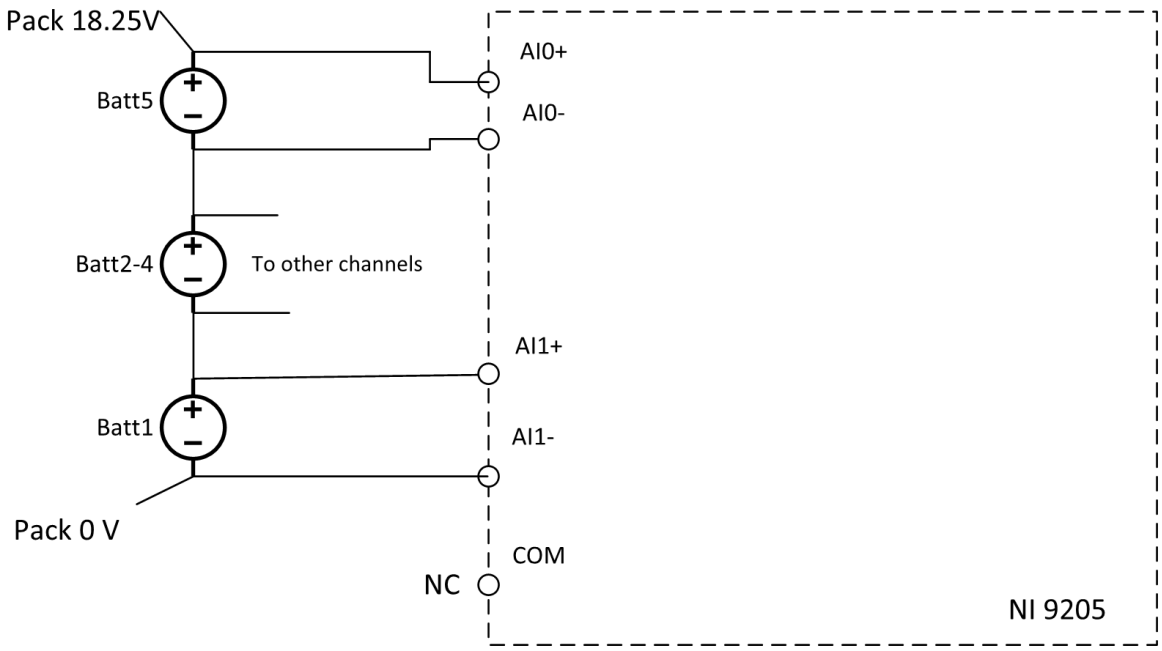

FIGURE 24. Wiring diagram of the National Instruments 9205 analog input module configured to measure differential voltages.

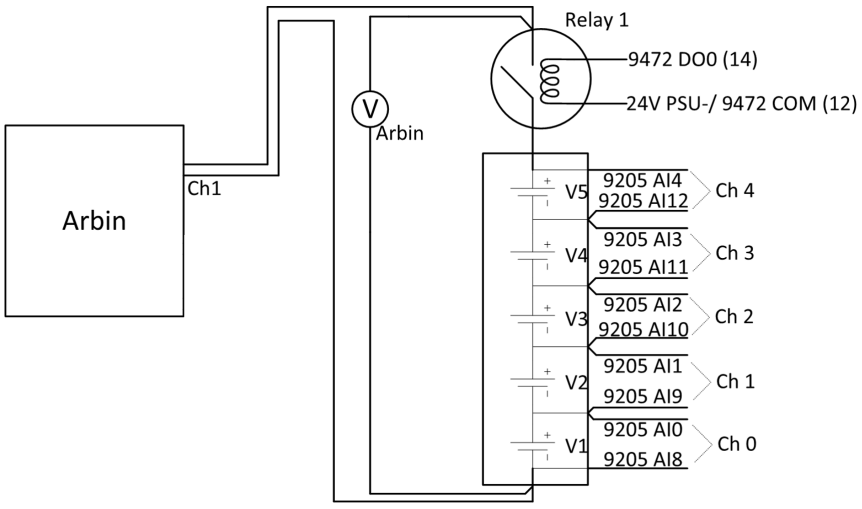

FIGURE 25. Wiring diagram of the National Instruments 9472 digital output module configured to control battery shutoff relays.

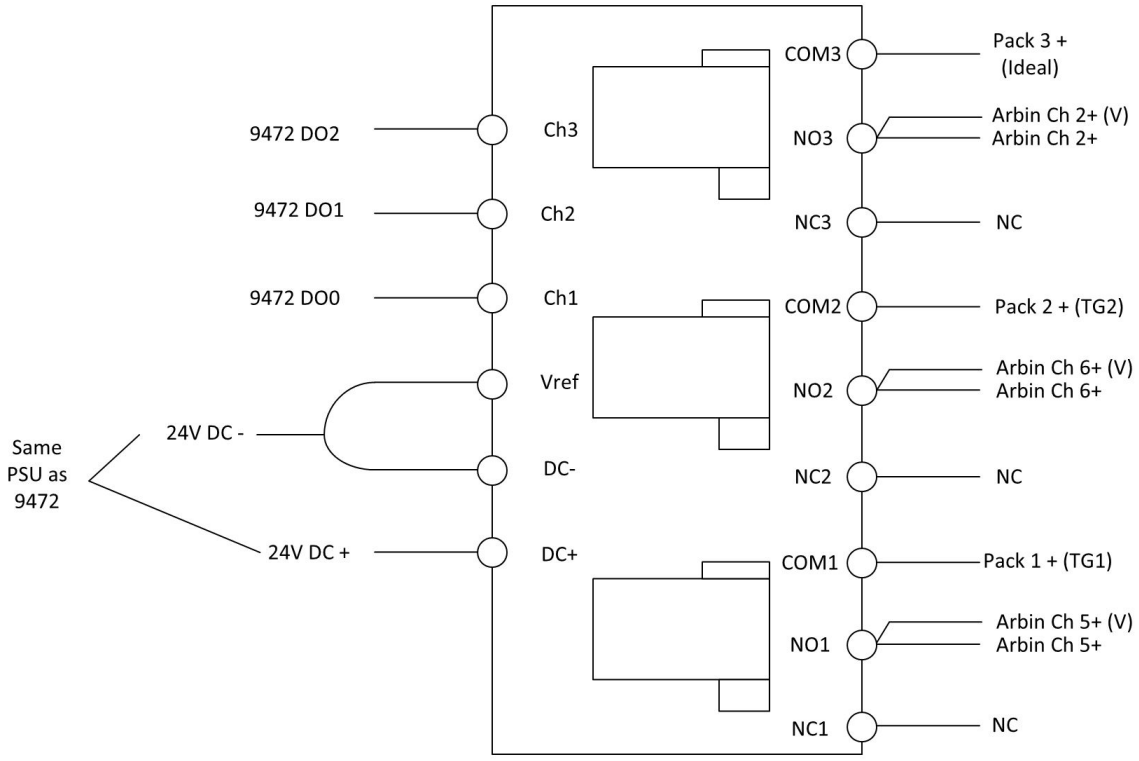

FIGURE 26. Wiring diagram of the relay board used to protect the batteries during cycling from over charge or over discharge.

7.4.5 Degradation Test Profiles

Cell Cycling This test performed a simple repetitive charging and discharging of a single cell. The goal of this test was to cycle the cell in a consistent way to degrade it. The results from this test were compared to the similar test for pack cycling. The test started by charging the cell at 1C (1.5A) until the voltage reached 3.65V. Typically, cells would be charged with a CCCV charge as in the capacity test described in section 7.3.2, but for this test, that was forgone in the interest of increasing the total charge throughput of the cells. The CV charge portion of a CCCV charge for these cells typically took 20-26 minutes, while only adding $< 0.1Ah$ of capacity to the cell. Meanwhile, by neglecting the CV charge, in the same time $0.5 - 0.65Ah$ could be cycled through the cell at 1C. Therefore, more total charge could be cycled through the cell by not performing CCCV charging, thus shortening the experimental time. After completing the charge, the cell was

allowed to rest for 30 seconds before being discharged at 1C until the voltage reached $2.5V$.The cell was then allowed to rest for 30 more seconds before being charged again. This was repeated for 200 cycles. This test was performed on cells at $20°C$ and at $45°C$. The test profile is defined below.

1. Rest for 10 seconds.
2. Charge cell at 1C (1.5A) until the voltage reaches 3.65V.
3. Rest for 30 seconds.
4. Discharge cell at 1C (1.5A) until voltage reaches 2.5V.
5. Rest for 30 seconds.
6. Increment cycle counter.
7. Check cycle counter. If cycles < 200, go to step 1. If cycles $>= 200$, go to next step.
8. Charge cell to 50% SoC.

Pack Cycling This test performed the pack equivalent of the above cell cycling test. However, special considerations had to be made for when the safety relay described in Section 7.4.4 was opened, and for the increased resistance added by the relay board. The pack was charged at 1C (1.5A), which is the same as for the cell because the cells were connected in series. The increased resistance of the relay board and the associated connectors between the battery test station and the battery pack increased the pack resistance from $\approx 300m\Omega$ to $\approx 2.3\Omega$. This caused a considerable voltage drop and resulted in the Arbin test station reaching the $20V$ limit before the battery pack was fully charged, or reaching the $12.5V$ lower limit before the pack was discharged. To avoid tripping safety limits, the charge was converted to a CCCV charge, but the constant voltage portion of the charge was set to 20 V rather than the pack maximum voltage. Meanwhile, the safety cutoff was set to 105% (21 V) of the voltage range, preventing it from triggering. This allowed the Arbin to continue charging the pack at the highest rate it was able to without cutting off the charge. For discharging, the lower voltage limit was based on observing the voltage drop during test experiments, and set to 9.6 V for the same reason. As discussed above in Section 7.4.4, the charge and discharge steps were ended by the relay which disconnected the battery pack from the Arbin. This resulted in the voltage spiking to outside of the safety limits. This effect can be

seen in Figure 27 when the pack voltage drops to $-4V$. The relay then closed and the voltage recovered to around $16V$, then the Arbin continued the test and began charging the pack. This was achieved in the Arbin software by defining the following program:

1. Rest for 10 seconds
2. Increment cycle counter.
3. CCCV Charge at 1.5 A until voltage reaches 20, then stop when the current $< 0.075A$.
   (a) If Voltage $> 20V$ (relay opened), go to next step
   (b) If Voltage $< 12.5V$, go to next step (safety).
4. Rest for 30 seconds and until voltage $< 18.25V$ (wait for relay to close).
5. Discharge at 1.5 A until voltage $< 9.6V$ or voltage $> 18.25V$ (until relay opens)
6. Rest for 30 seconds and until voltage $> 12.5V$
7. If cycle counter < 200, go to step 2, else wait 5 seconds and end test.

FIGURE 27. Plot of pack voltage over a discharge cycle, showing the relay cutting off the discharge step.

Part IV

Results and Discussion

8 Initial Cell Characterization Data

8.1 Summary Data

The initial state of all the cells is shown in Table 5. The table is sorted by where each cell was used (as opposed to cell number). This was the data that was used to match cells together into packs and testing groups. It shows for each cell, what cycling or degradation test it was used for, and at what temperature the test was run. The bottom of the table shows cells that had no assigned experiment, these cells were not used, but were initially characterized to increase the sample size of cells to select from. They were also used to increase the sample size of room temperature calendar aging cells. This data was based on the standard Cell Capacity Test (Section 7.3.2). The table also shows some cells listed as their primary experiment being neutron radiography. This was because the initial plan only called for these cells to be neutron imaged, but eventually all cells were imaged (before and after testing), thus negating the need for that experiment. For cells connected in a pack, the cell number (shown in the table as (C#) started with cell 1 being the cell whose negative terminal was the pack's negative terminal, and cell 5 being the cell who's positive terminal was the pack's positive terminal. For packs with non-uniform temperatures, cell 1 was also the coldest cell, while cell 5 was the hottest cell.

TABLE 5: Initial cell characterization data.

Cell #	**Experiment**	**Temperature ($°C$)**	**SoH**	**Capacity (Ah)**	**Efficiency**	**0.1s DCIR ($m\Omega$)**
16	calendar avg SoH	20	94.1%	1.41	93.7%	59.97
25	calendar avg SoH	5	94.0%	1.41	93.7%	60.10
65	calendar avg SoH	45	94.2%	1.41	93.6%	59.90
8	calendar max SoH	20	95.2%	1.43	93.8%	58.33
11	calendar max SoH	5	95.6%	1.43	94.0%	58.82

12	calendar max SoH	45	95.1%	1.43	93.6%	61.67
48	calendar min SoH	20	93.0%	1.39	93.5%	59.83
54	calendar min SoH	45	93.0%	1.39	93.4%	60.97
69	calendar min SoH	5	92.9%	1.39	93.4%	61.06
5	ideal pack C1	5	94.5%	1.42	93.3%	60.50
21	ideal pack C2	20	93.7%	1.41	93.2%	60.82
28	ideal pack C3	20	94.2%	1.41	93.5%	61.06
57	ideal pack C4	20	94.1%	1.41	93.5%	61.00
70	ideal pack C5	20	94.3%	1.41	93.4%	60.62
22	individual avg SoH	20	94.3%	1.41	93.5%	59.97
40	individual avg SoH	20	93.6%	1.40	93.2%	59.77
41	individual avg SoH	45	94.4%	1.42	93.3%	60.08
4	individual max SoH	20	94.9%	1.42	93.4%	57.40
52	individual max SoH	5	95.0%	1.42	93.0%	60.98
62	individual max SoH	45	94.9%	1.42	93.2%	60.19
9	individual min SoH	45	93.1%	1.40	93.5%	60.08
45	individual min SoH	20	93.0%	1.40	93.3%	62.93
64	individual min SoH	5	93.0%	1.40	93.1%	58.65
2	neutron radiography	20	93.9%	1.41	93.6%	58.13
10	neutron radiography	20	94.8%	1.42	93.5%	58.01
13	neutron radiography	20	93.1%	1.40	92.9%	62.84
61	neutron radiography	20	93.4%	1.40	93.4%	60.27
66	neutron radiography	20	93.4%	1.40	93.0%	66.16
73	neutron radiography	20	93.9%	1.41	92.7%	61.51
74	TG pack 1 C1	3.5	94.3%	1.41	93.6%	58.85
55	TG pack 1 C2	7.75	93.7%	1.41	93.6%	59.20
42	TG pack 1 C3	12	94.4%	1.42	93.6%	58.64

20	TG pack 1 C4	16.25	94.3%	1.41	93.6%	58.84
17	TG pack 1 C5	20.5	94.0%	1.41	93.3%	58.93
56	TG pack 2 C1	26.5	94.8%	1.42	93.6%	59.45
49	TG pack 2 C1	26.5	93.5%	1.40	93.4%	59.58
44	TG pack 2 C2	30.75	94.3%	1.41	93.6%	59.38
43	TG pack 2 C3	35	94.4%	1.42	93.3%	59.06
15	TG pack 2 C4	39.25	94.0%	1.41	93.7%	59.08
14	TG pack 2 C5	43.5	94.3%	1.42	93.5%	58.98
1		20	93.2%	1.40	93.0%	63.18
3		20	94.4%	1.42	93.1%	60.78
6		20	93.7%	1.41	93.5%	58.19
7		20	93.7%	1.40	93.2%	61.80
18		20	93.8%	1.41	93.7%	58.32
19		20	93.6%	1.40	93.3%	60.71
23		20	93.6%	1.40	93.2%	58.98
24		20	93.8%	1.41	93.3%	62.75
26		20	94.2%	1.41	93.6%	58.83
27		20	94.1%	1.41	93.7%	60.28
29		20	94.7%	1.42	93.5%	61.90
30		20	94.6%	1.42	93.1%	62.57
46		20	93.4%	1.40	93.7%	59.75
47		20	93.3%	1.40	93.1%	62.10
50		20	93.3%	1.40	93.2%	60.93
51		20	93.5%	1.40	93.4%	60.48
53		20	93.7%	1.41	93.2%	61.22
58		20	94.7%	1.42	93.6%	59.77
59		20	94.1%	1.41	93.1%	60.16

60		20	93.1%	1.40	93.4%	60.96
63		20	93.5%	1.40	93.3%	60.48
67		20	94.1%	1.41	93.3%	64.14
68		20	93.3%	1.40	93.5%	59.16
71		20	93.3%	1.40	93.0%	65.08
72		20	93.8%	1.41	93.4%	57.64

8.1.1 Capacity Test Results The distribution of cell SoH is shown in Figure 28. It is interesting to note that no cell had a capacity greater than or equal to the rated capacity of the cells, which was 1.5 Ah. The datasheet did provide a range of 1.45-1.55 Ah, but still no cell had even the lower end of this capacity. However, the consistency of the capacity of the cells was quite good, with the standard deviation being only 0.009 Ah, or 0.6% of the rated capacity. This was inline with expectations about cell manufacturing consistency. Brand et. al. [32] found a variation of $\kappa_Q = 0.72\%$ where κ_Q was defined as the standard deviation of the capacity divided by the mean value of capacity, or $\kappa = \frac{\sigma_Q}{Q}$. Using this metric, $\kappa_Q = 0.66\%$ for the initial state of these cells. Similarly, the 0.1-second internal resistance of the cells at 50% SoC, which was measured during the capacity test as described in Section 7.3.2 had a standard deviation of $1.70m\Omega$, a mean of $60.34m\Omega$, and a $\kappa_{IR} = 2.82\%$. This was as compared to Brand et. al's result of $\kappa_{IR} = 1.83\%$, being consistent with their results in that the coefficient of variation of internal resistance was larger than that of capacity. By using the data collected from the capacity tests with the matching algorithm described in Section 7.4.3, the consistency of the cells chosen to be packed together for the series connected packs was increased. For example, $\kappa_{Q,TG1} = 0.28\%$ and $\kappa_{IR,TG1} = 0.31\%$.

8.2 Capacity Characterization Test Results

The results of this test exemplified the importance of using a standard capacity test that cycled the cell according to the datasheet's recommendations. This test was run on 10 cells (13, 14, 16, 17, 18, 19, 20, 21, 54, and 55), which provided a good spread of cell characteristics and meant that

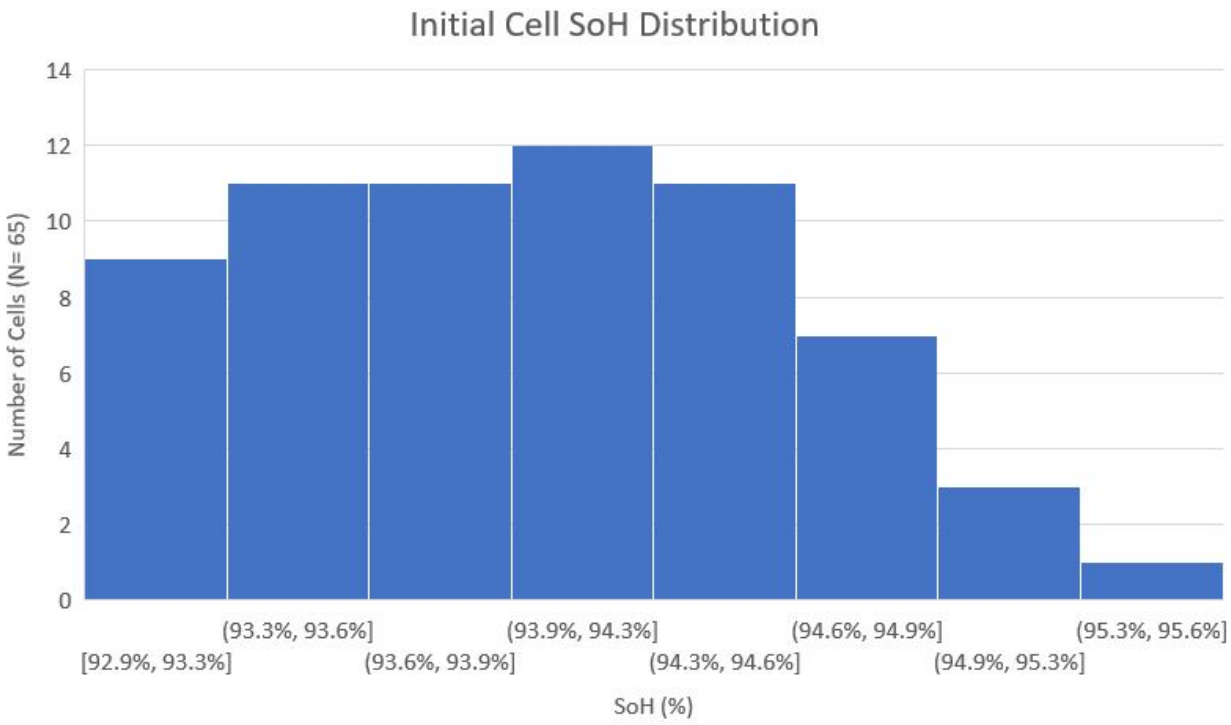

FIGURE 28. Histogram of the initial distribution of cell SoH before any other testing had been performed.

most degradation experiments had a representative cell characterized in this test. The discharge capacity of the cells is plotted in Figure 29. The large reduction in measured capacity at C/5 was due to an error in the battery test station program where the cells were only charged to 3.36 V instead of 3.65 V. This occurred during the charge step of the C/10 cycle. Since the charge step was done after the discharge step, this error did not affect the measured discharge capacity of the C/10 cycle. In Figure 30, this error was 'corrected' by taking the average value of discharge capacity from the C/10 cycle and the C/2 cycle for each cell as the discharge capacity at C/5. While this methodology is not perfect, it still provided some interesting insights nonetheless.

After the correction to the C/5 rate was made, Figure 30 shows that there are two distinct curves to the capacity as a function of C-rate. This is expected behavior, and the elbow of the curve is what defines the maximum nominal working C-rate of the cell [227]. Since the rated C-rate of these cells was C/2, and the elbow of the capacity vs. C-rate curve in Figure 30 is at C/2, the cells performed as designed. The location of the elbow, and hence the power capability of the cell, is a

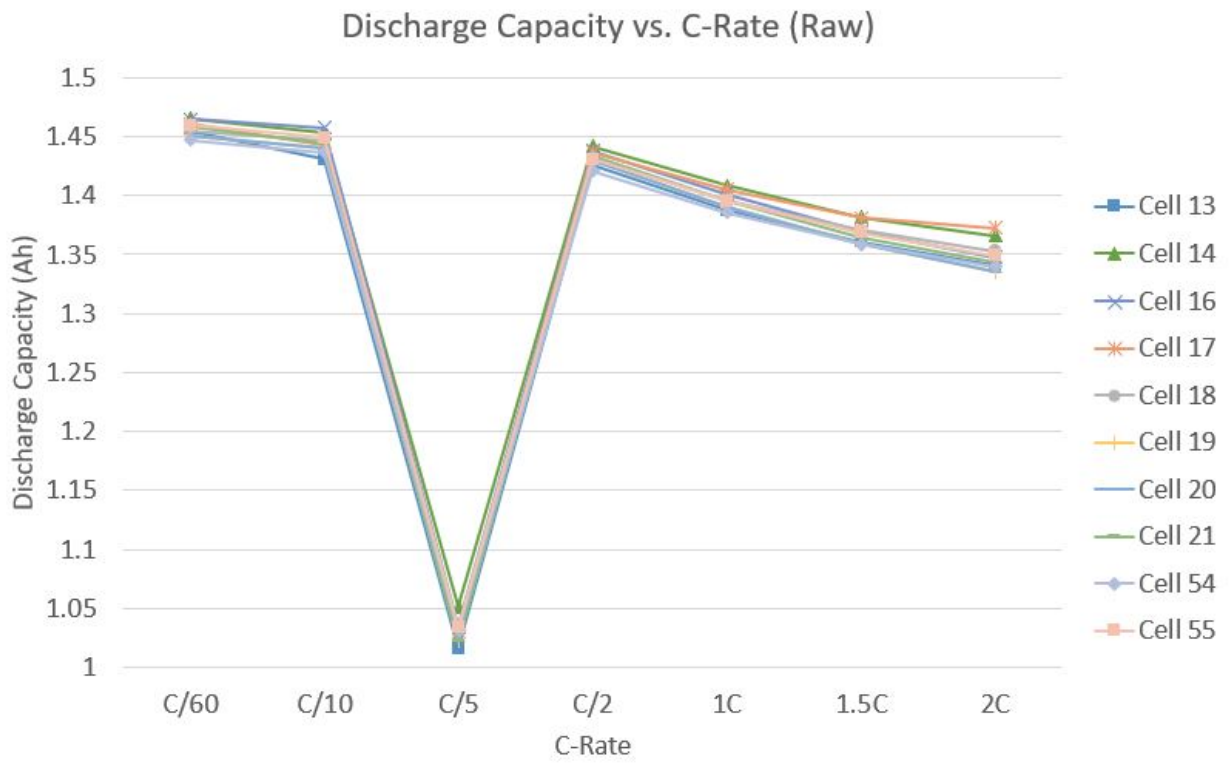

FIGURE 29. Plot of 10 cells discharge capacity as a function of discharge C-rate. Note the outlier at C/5.

function of the electrode thickness, with higher energy density cells having thicker electrodes that increase capacity, but reduce maximum working current [227]. Since the degradation cycling tests were performed at 1C, Figure 30 shows the importance of using a separate capacity test to track cell degradation rather than relying on data from the degradation cycles themselves.

8.3 Internal Resistance Characterization Results

This test was run on 5 cells, 4, 27, 61, 66, 71, and 72. These cells were selected based on their 1 second discharge resistance at 50% SoC as measured by the capacity test (Section 7.3.2). Cells 4 and 72 were selected as the two lowest resistance cells, 27 and 61 were chosen to represent average resistance cells, and 66 and 71 were chosen as the two highest resistance cells.

The results of the internal resistance characterization test, as described in Section 7.3.4, are shown in the following figures and show the 0.1 second internal resistance and the 10 second internal resistance as a function of SoC and temperature. Firstly, in Figure 31, the resistance can be seen

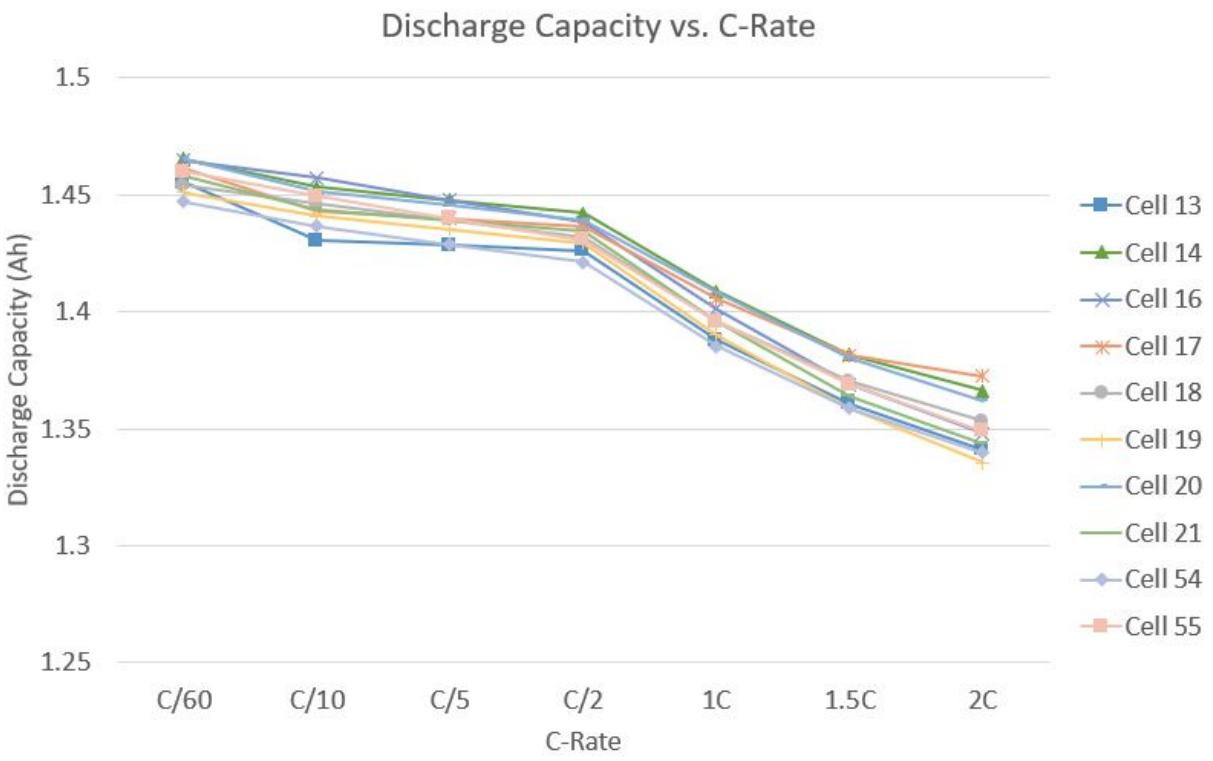

FIGURE 30. Plot of 10 cells discharge capacity as a function of discharge C-rate.

to decrease with increasing temperature. However, at $50°C$ erratic behavior of the resistance can be observed. The $50°C$ resistance shows extremely high values across a wide range of SoCs, and moreover, is not consistent between cell samples. For example, cell 4 saw a large increase in $50°C$ resistance at around 90% SoC, while cell 27 saw higher resistance between 10-60% SoC. It was determined that this was not an unusual characteristic of these cells, but rather due to the testing fixture. Since the cell holder described in Section 7.3.1 was 3D printed from PLA, the fixture softened sufficiently at $50°C$ to allow the pressure from the spring to deform the plastic which resulted in poor cell contact. Therefore the $50°C$ results were removed. The remaining resistance was then averaged across all cells for each temperature and resistance and the resulting data is shown in Figure 32. Note that Figure 32 includes data from more than the 6 cells plotted in Figure 31.

In Figure 32, the behavior of the 0.1 second DC resistance is clearly visible. It can be seen that the cell resistance was higher at lower SoCs, especially when the SoC was less than 10%. Inspecting

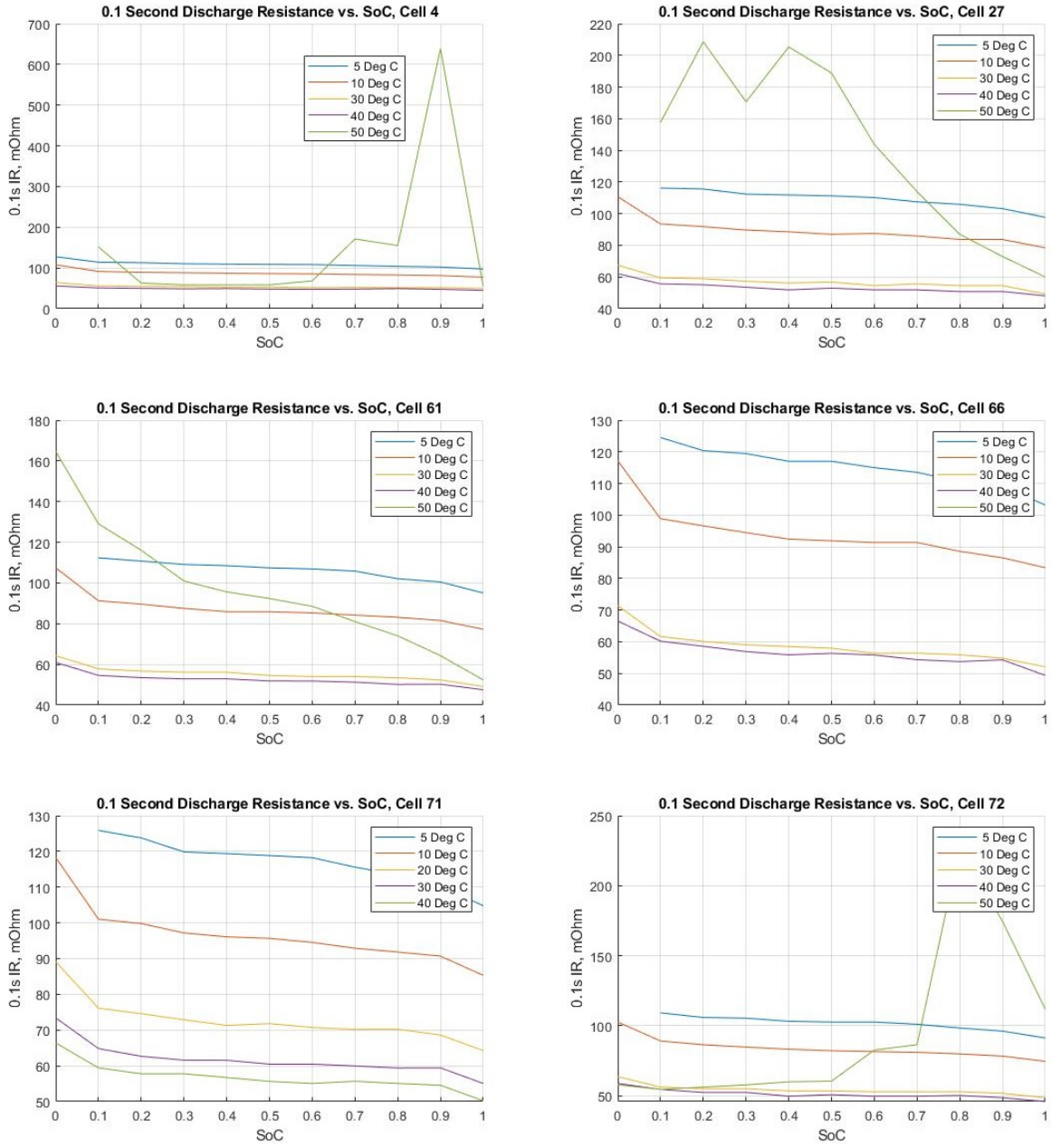

FIGURE 31. Plots showing the 0.1 second discharge resistance's dependence on SoC and temperature. Error bars are 1 standard deviation of the resistance for the cells measured at that temperature.

the plots closely shows that the near 0% SoC resistance data points become farther from 0% SoC as the temperature was decreased. This was because the resistance was measured by a discharge current pulse, but at lower temperatures, the increased cell resistance meant that the lower cutoff voltage limit was reached earlier, preventing measurement at very low SoCs. Interestingly, the

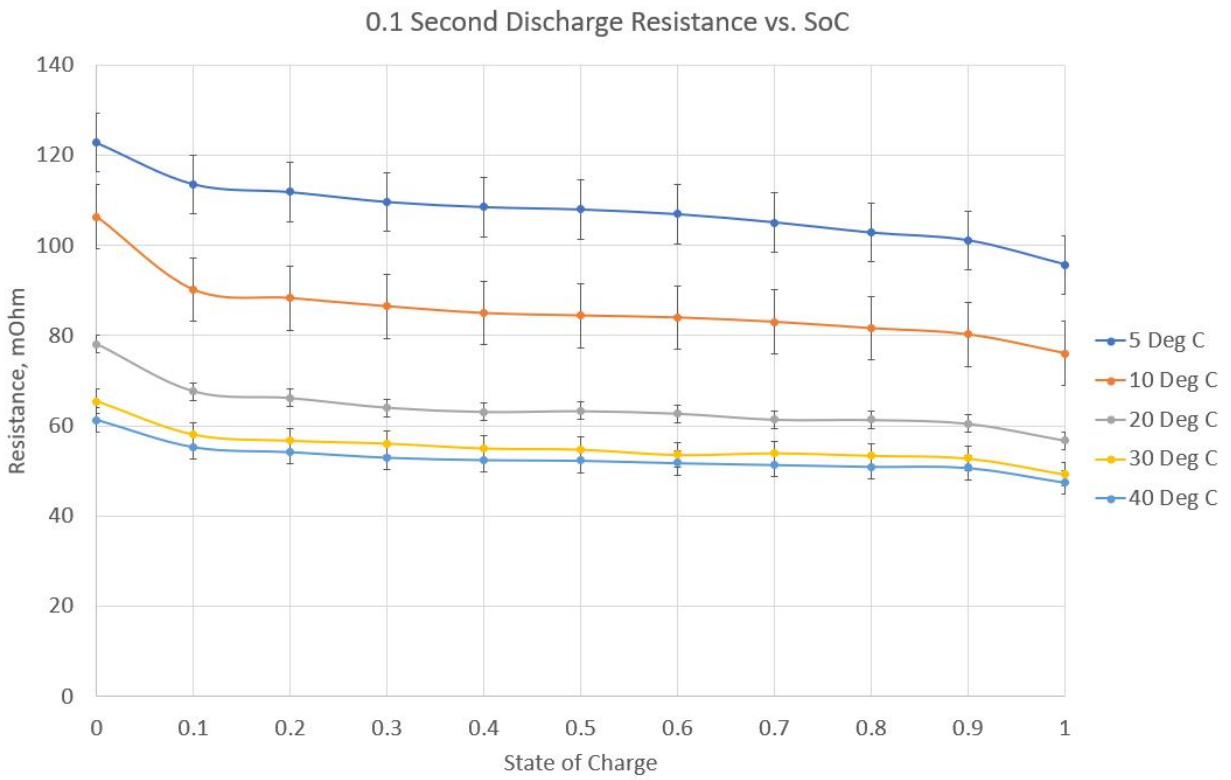

FIGURE 32. Plots showing the 0.1 second discharge resistance's dependence on SoC and temperature with the $50°C$ results removed.

resistance was decreased when the cell was fully charged. The literature was strangely quiet on this phenomenon, suggesting this resistance change may be an area requiring future study. One possible explanation for the lower resistance at high SoC could be the volume change of the cell. As mentioned above, the cell expands most when charged to around 95-100% SoC. Then, since the cylindrical cell is contained within a metal can, this expansion results in increased pressure on the cell layers. It is also known that cell compression can reduce the Ohmic resistance of cells [229] and thus it seems reasonable to hypothesize that this was the mechanism behind the result presented in Figure 32. Another interesting observation was that the standard deviation of the results at lower temperatures was 3 times higher than the higher temperatures. Given that a similar number of cells were tested at each temperature, and the same procedure and equipment was used for all experiments, this may suggest that cell manufacturing differences can be more easily detected by measuring the resistance at low temperature.

As expected, the resistance decreased substantially as temperature increased to around $30°C$, after which increasing the temperature provided only marginal improvements in the resistance of cell. This was in agreement with the Arrhenius Equation 15, as can be seen in Figure 35. To generate Figure 35, the 0.1 second DC discharge resistance was averaged across all cells for each SoC and temperature. As with Figure 32, the $50°C$ data was excluded. Then the resistance data for 50% SoC was taken and the reference temperature was set to $30°C$ ($303°K$), and Rref was the average resistance from all the cells at $30°C$. Then, the activation energy of the Arrhenius equation was found using a non-linear least squares fit which produced the results shown in Figure 35.

For the 10 second resistance, it can be seen in Figure 33 that the magnitude of the resistance was significantly higher than the Ohmic resistance. This was expected because the 10s resistance included both the 0.1s Ohmic resistance and the electrochemical resistance. The shape of the curve was also different for the 10s resistance. While the 0.1s resistance had a slight increase at 0% SoC and a slight decrease at 100% SoC, the 10s resistance had a large increase at both 0% and 100% SoC. Between 10% and 0%, the 10s resistance increased by $\approx 50\%$, and the resistance at 100% SoC increased by $\approx 50\%$ at low temperatures, and by over 100% at higher temperatures. This implies that when nearly fully charged, the cell entered a region where factors other than temperature began to have a measurable impact on cell performance. These could include local overcharging of the anode, reduced intercalation site availability, increased SEI layer formation rate, and anode potential changes at high SoC. Note that these effects were sufficient to completely cancel out the slightly lower Ohmic resistance observed at 100% SoC.

Another interesting observation can be made that at high temperatures, the 10s resistance was only marginally (20%) higher than the 0.1s resistance. But as the temperature was reduced, the 10s resistance increased significantly faster than the Ohmic resistance, resulting in a difference of 50%. This would suggest that the electrochemical resistance was more susceptible to temperature changes than the Ohmic resistance, which should be expected as the electrochemical processes in LIBs are highly temperature dependent. This was made even more clear by plotting only the electrochemical resistance by subtracting the 0.1s resistance from the 10s resistance as shown in Figure 34. Here it

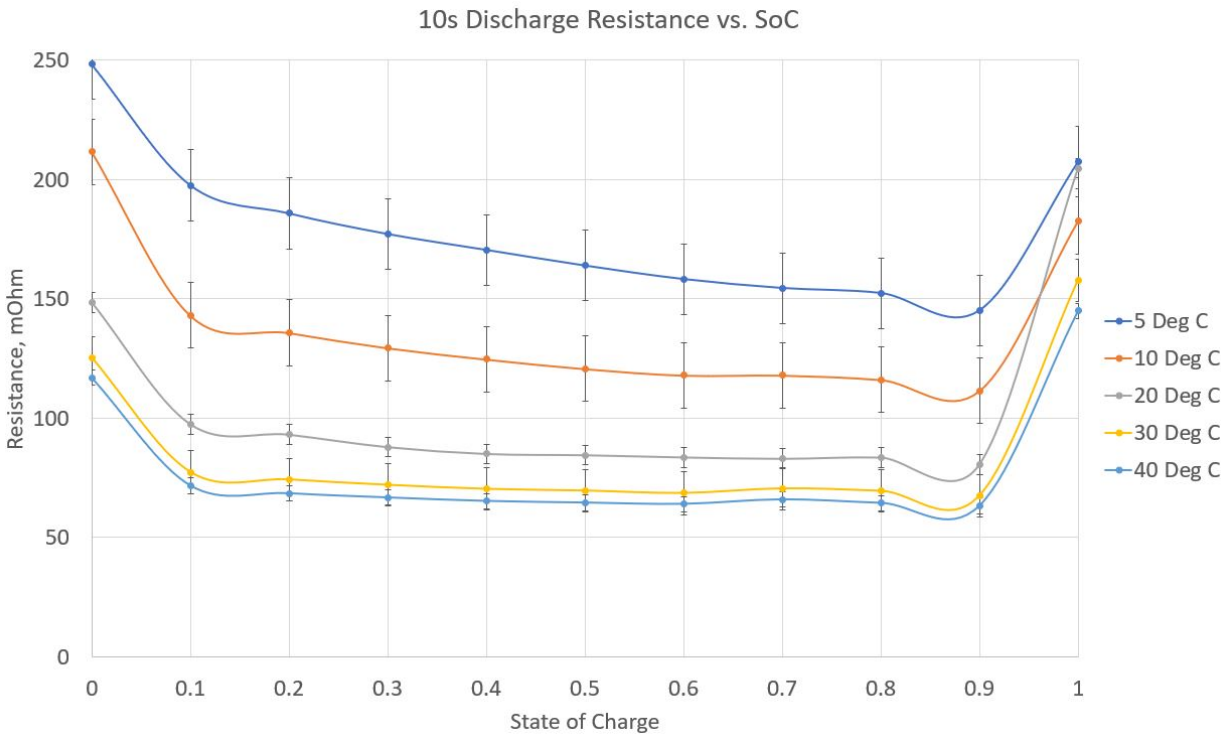

FIGURE 33. Plots showing the 10 second discharge resistance's dependence on SoC and temperature.

can be seen that the electrochemical resistance was lower than the Ohmic resistance for intermediate values of SoC. But at high and low SoC, the large increases in electrochemical resistance dominated the behavior of the overall 10s resistance of the cells. Also, the temperature sensitivity of the electrochemical resistance was even higher than that of the 10s resistance. At 50% SoC, the resistance increased by an average of 380% between $40°C$ and $5°C$ compared to just 160% for the 10s resistance and 110% for the 0.1s resistance. Again, it makes sense that the electrochemical resistance was affected significantly more than the Ohmic resistance by changes in temperature.

To further illustrate the difference in the effect of temperature on the electrochemical vs. Ohmic resistances, consider the plots in Figures 35 and 36, which show the fit of the Arrhenius relations and the calculated activation energies for the Ohmic and electrochemical resistances, respectively. Immediately the difference in activation energies is obvious, with the electrochemical resistance of $\approx 42kJ/mol$ being 2.2 times higher than the Ohmic resistance's activation energy of $\approx 19kJ/mol$. The larger activation energy of the electrochemical resistance implies that it is much more tem-

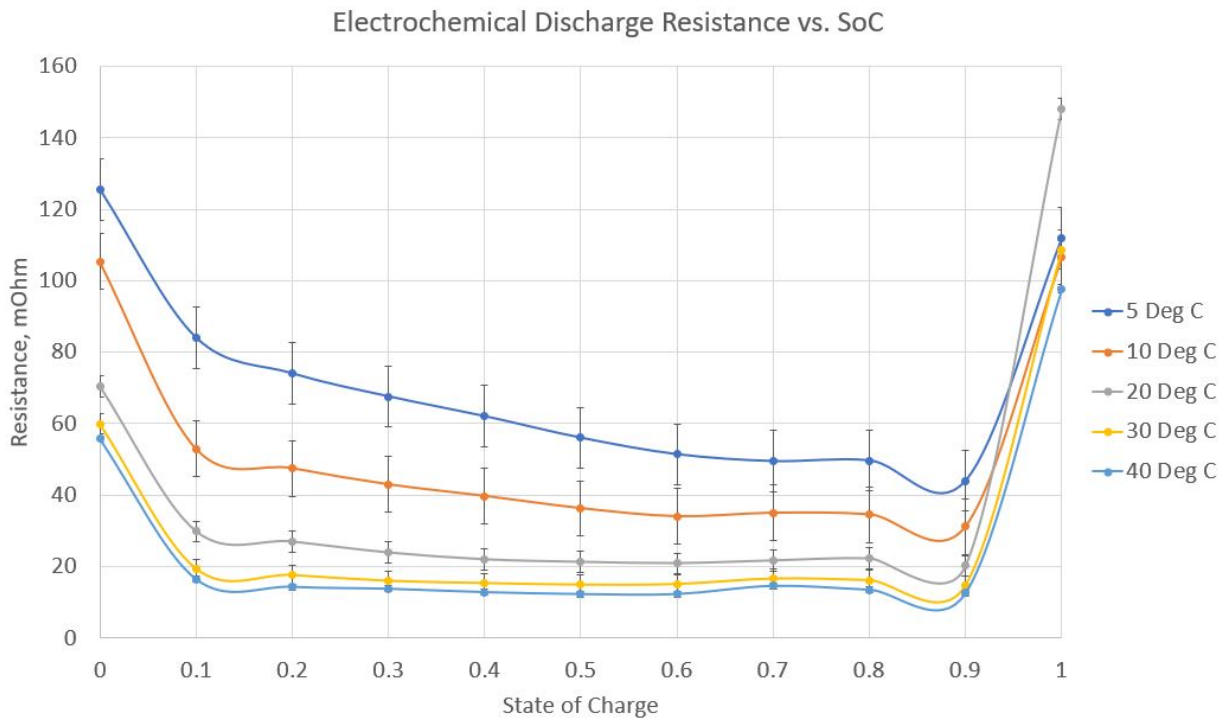

FIGURE 34. Plots showing the electrochemical discharge resistance of the cells, which is the difference between the 10s resistance and the 0.1s resistance. Error bars are 1 standard deviation of the resistance at 50% SoC for all tested cells at that temperature.

perature dependent, and at low temperatures requires additional over potential (which manifests as a terminal voltage drop) to discharge the cell [230].

The implications of this resistance data for battery packs with non-uniform temperatures are clear. Considering pack TG1, the coldest cell was $3.5°C$, so would be expected to have a resistance of $\approx 120m\Omega$. Meanwhile, the warmest cell was $20.5°C$ and would have a resistance of $\approx 75m\Omega$, which amounts to the colder cell having a 60% higher resistance. For cells connected in parallel as demonstrated by Klein [17], this will lead to large current variations between the cells, and as shown by Gogoana et. al. [231], this in turn leads to rapidly accelerated degradation. For series connected packs, this difference means that the usable capacity of the entire pack is reduced due to the colder cell hitting the discharge cutoff voltage.

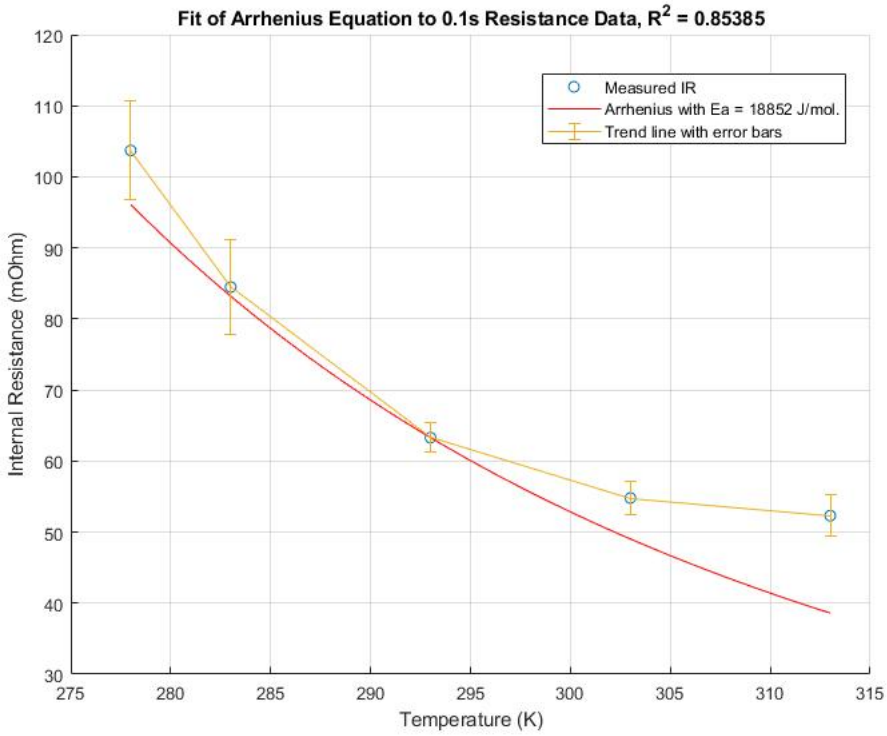

FIGURE 35. A fit of the Arrhenius Equation to the 0.1 second discharge data from the IR characterization test at 50% SoC. Error bars are 1 standard deviation of the resistance at 50% SoC for all tested cells at that temperature.

9 Degradation Results

9.1 Neutron Radiography Results

The first NR images are shown in Figure 37, which was taken on cells 2, 10, 13, 61, 66, and 73. Before image processing began, manual interpretation of the images was done. The first notable thing about the images was the high intensity (high neutron absorption) around the perimeter of the batteries. The effect was more pronounced when the cells were imaged along the cylindrical axis of the cell. These regions do not indicate that there was a high lithium concentration at the edge of the cell, but were the result of neutron imaging edge effects. Specifically, refraction, diffraction, and blur due to imperfect beam collimation are the main source of the edge enhancement effect. Making the effect more pronounced was iron's low (< 1) index of refraction for neutrons [232, 233]. The outer casing of the cell was made from steel ($\approx$ iron), and this resulted in the edge effects shown in Figure 37. It is also common for thicker samples to have more pronounced edge effects,

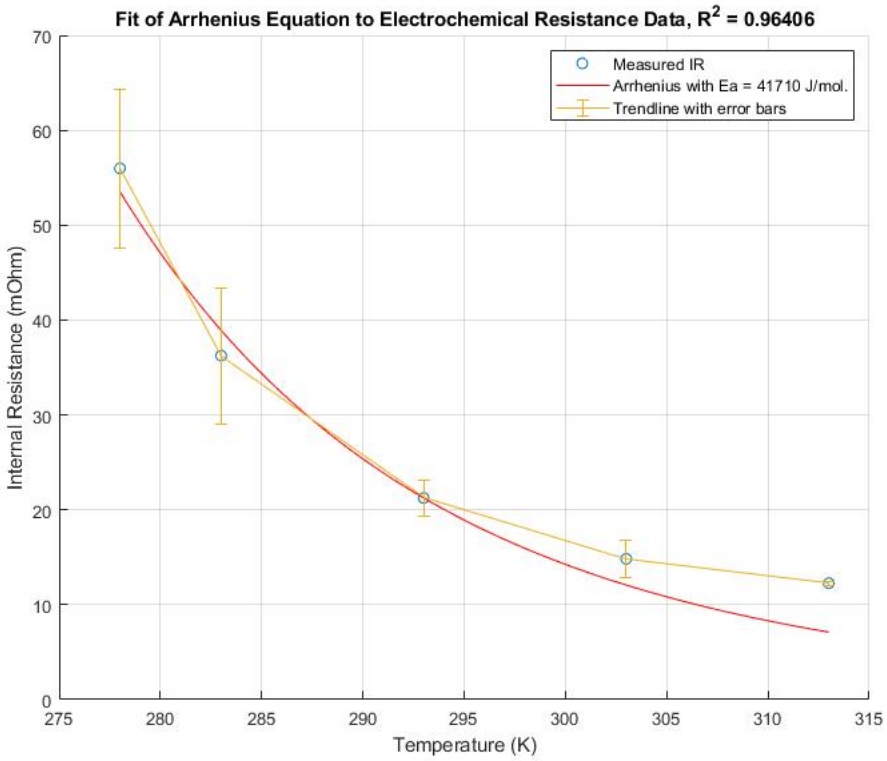

FIGURE 36. A fit of the Arrhenius Equation to the electrochemical resistance discharge data from the IR characterization test at 50% SoC.

and this increase is linear [233]. This is due to the increased chance that a neutron traveling through the sample will interact with the sample as the distance through the sample increases. This explains the higher apparent absorption at the edge of the cells when they were imaged along their cylindrical axis. Based on these images, it was determined that imaging the cells axially was the best way to measure changes in lithium concentration throughout the entire cell as it would provide a radial lithium distribution and the geometry made isolating cell areas from the image simple. Therefore, further NR imaging samples were taken axially only.

9.1.1 Neutron Data Analysis

The images generated by the detector were .dcm (dicom) images, with a bit depth of 10. This gives the images a dynamic range of between 0 and 1024, compared with a traditional .jpg which has a bit depth of 8 and dynamic range of 0-255. The original images are inverted compared to

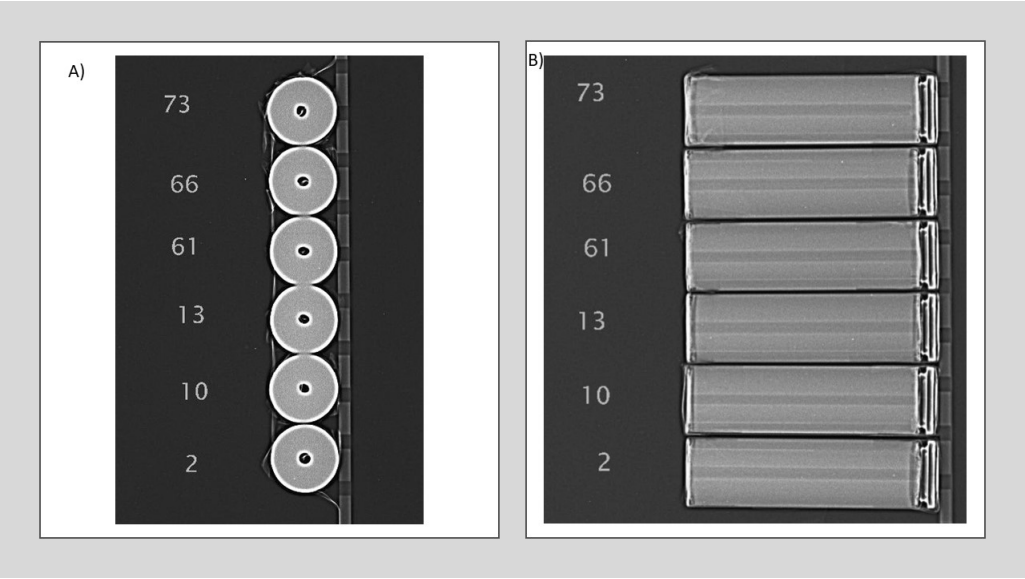

FIGURE 37. NR images showing both the top (A) and side (B) view of the first set of cells that were imaged. (Those listed under 'neutron radiography' in Table 5).

Figure 37, as a brighter pixel meant more neutrons were transmitted through the sample. The images were inverted such that a brighter pixel indicates more neutron absorption. A colorized version of images was then generated, as this allowed for easier inspection of the images. This was done by mapping a color space to the pixel intensities. This mapping had the result of reducing the bit depth of the colorized images to 8, so was used for qualitative analysis only. An example of one of these colorized images is shown in Figure 38 which shows the NR image of all the cells taken after the degradation experiments.

In Figure 38, some of the cells do not appear to be perfectly circular. This was caused by imperfect alignment of the cells with the direction of the neutron beam causing the projected profile of the cell to appear elongated. This misalignment was not due to the neutron beam angle, otherwise all the cells would have appeared similarly. More likely, the tape holding the cells in place was loosened while relocating the imaging tray and positing it with the remote-controlled sample holder. In extreme cases, such as with cell 55 (bottom right corner), the misalignment could be such that it blocks the entire center hole of the cell from showing on the image. This 'hole' in the center of the cell is empty space not occupied by the jelly roll due to the small bending

radius, and to allow for volume changes of the cell during charge/discharge and as the cell ages. For example, Waldmann et. al. [125] found that after degradation, the layers of the jelly roll deformed and began to fill the space in the center of the cell, and this effect was worse for cells aged by cycling at higher C-rates. Thus, it may in principle be possible to estimate the SoH and gain insight into the degradation mechanism of the cell by measuring the diameter of the central column on the jelly-roll. However, due to the imperfect alignment of the cells in imaging tray this was not possible from the results obtained in this experiment.

The next step in quantifying the results from the NR images as to normalize the brightness/exposure of each image. This was done by choosing a reference image, then selecting an area of the image that only contained the aluminum tray. The average brightness of the tray was then calculated by taking the average grey scale value of each pixel in the reference area. Then for each additional NR image (input image), a sample area of the tray was taken and the brightness averaged. The ratio of reference brightness to the input image's reference area brightness was taken. Next the grey scale values of the entire input image were multiplied by the brightness ratio. This method ensured that the exposures between all the NR images were equalized so that calibration differences could be eliminated as a potential source of appreciable error.

After image normalization, the pixel coordinates of the center of each cell were located manually in the image using the open source image editing software GIMP 2.10.20. For future NR studies with larger quantities of cells, implementing an image recognition system to extract the cell center locations from each NR image would be highly recommended. As it was, the sample size of cells made the manual approach feasible. A MATLAB script was then used to extract circular areas of the input NR image corresponding to the cell area. These were then centered on a new 10 bit 170x170 pixel image, an example of which is shown in Figure 39 left. The background of the extracted cell area was set to black to make analysis of the cell area simpler. Also as may be seen when comparing Figures 39 and 37, the edge effects have been removed from the extracted cell. This was done by simply reducing the diameter of the area around the cell's center to be extracted. These extracted images were also colorized and plotted using a 3D representation as

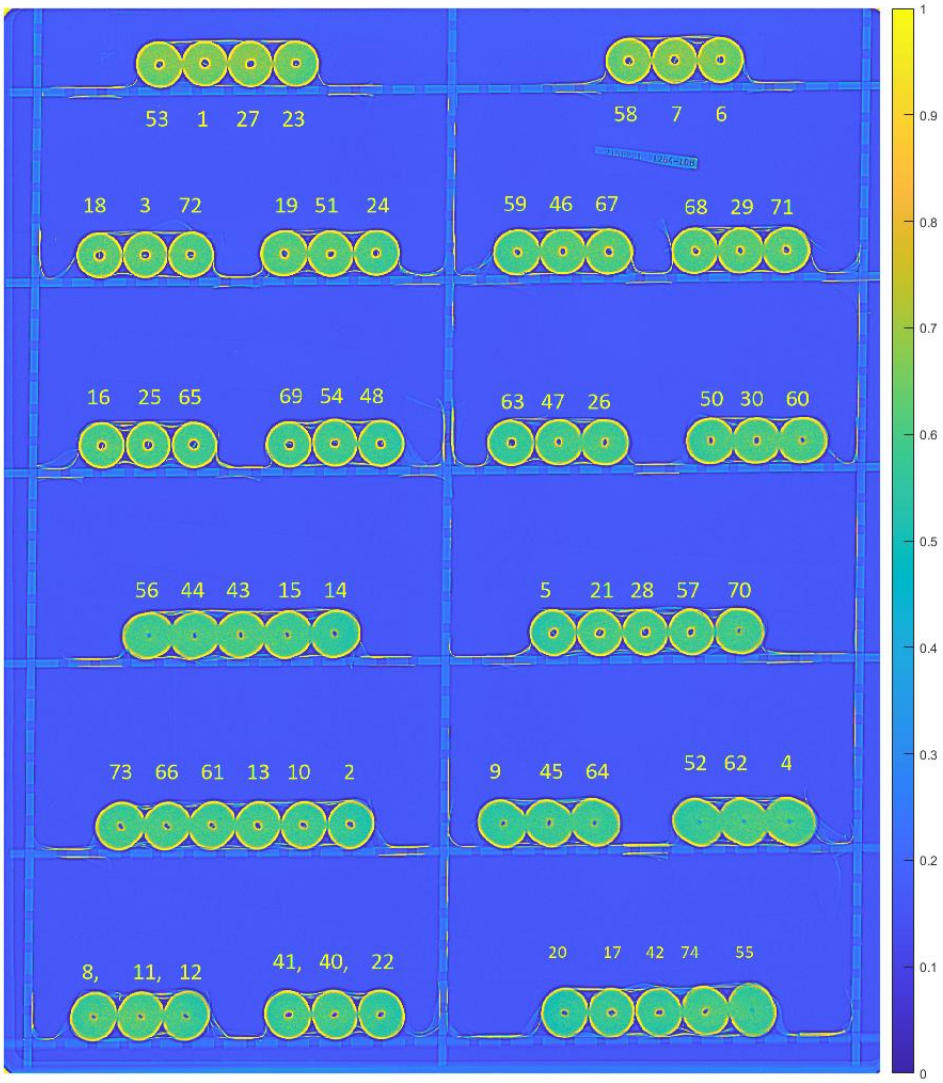

FIGURE 38. A colorized neutron image, where blue indicates less neutron absorption by the sample and yellow indicates more neutron absorption. Image taken with neutrons passing axially through the cylindrical cells. The numbers adjacent to each cell correspond to the numbers in Table 5.

shown in Figure 40. These images were used for quick visual inspection to determine if there was any problem with the image that may require correction, examples of which include noise pixels pinned to the maximum value of intensity and edge effects that had not been sufficiently removed.

To analyze each of the extracted cell images, the edge effects at the center of the cell needed to be removed as well. This was done by selecting a rectangular 52x52 pixel area from the center of the image and setting all pixel grey scale values in this region to 0. While this did remove some of the image data in the region of the cell, the area was equally sized for all cells, analysis was not done based on the total count of pixels, and the absorption intensity was mostly uniform throughout the cell area. An example of a resulting cell image is shown in Figure 39 right. From this image, the average intensity of the cell's neutron absorption was calculated, and a histogram of grey scale intensities was generated, an example of which is shown in Figure 41 C. A Gaussian distribution was then fit to the histogram using the open source peak fitting package for MATLAB, peakfit.m [234]. Using this function, the peak position, full width at half-maximum, and height were calculated. An example peak fit can be seen in Figure 41 A, with the residual plot of the fit shown in Figure 41 B.

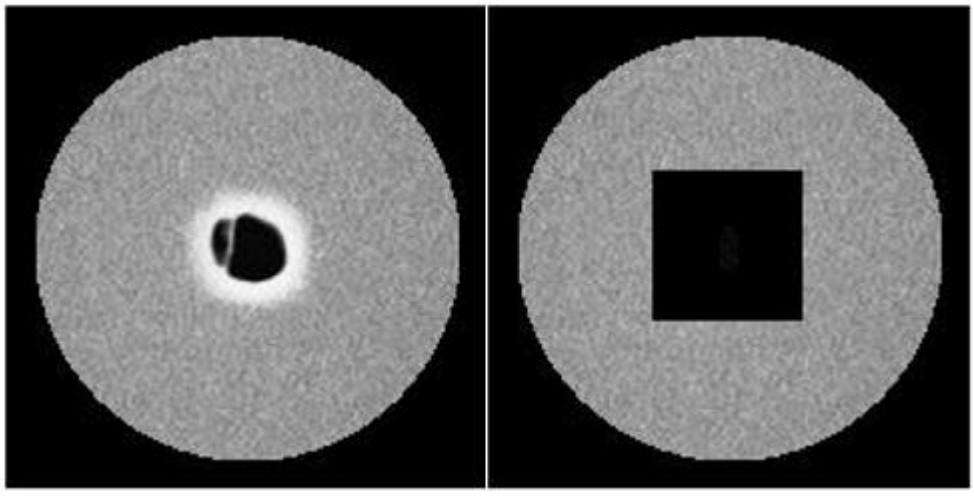

FIGURE 39. Example of an extracted cell image from an original NR image. Left) Single cell image with the center edge effects still in place. Note the jelly roll winding can be seen to not be perfectly wound at the center of the cell. Left) The same image after removing the center area of the cell to remove the edge effects. Note that both these images have been scaled down to 8-bit dynamic range for reproduction purposes.

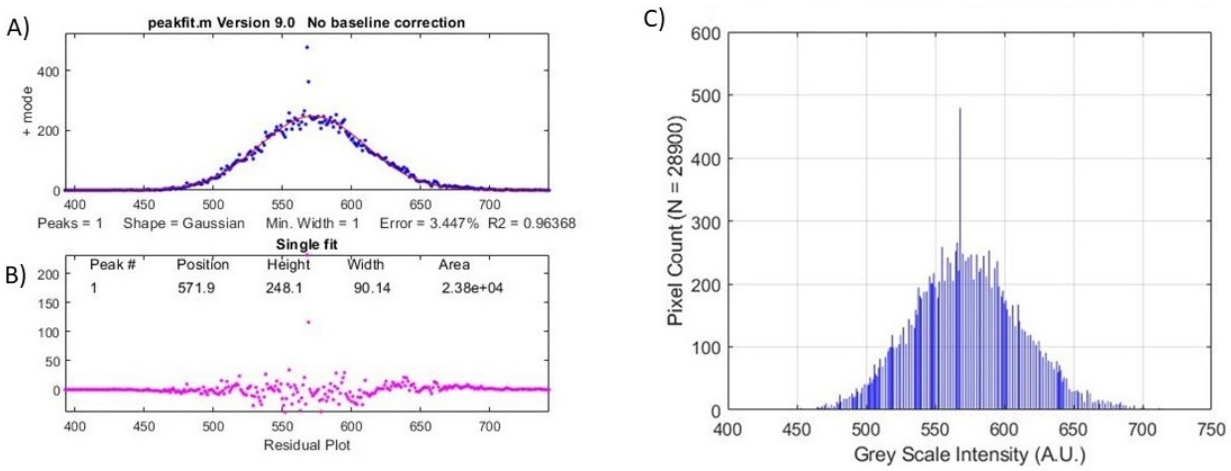

FIGURE 41. A) A Gaussian distribution fit to the NR image intensity histogram. B) Residual plot of the distribution fit. C) The raw histogram of the extracted cell image from the original NR image.

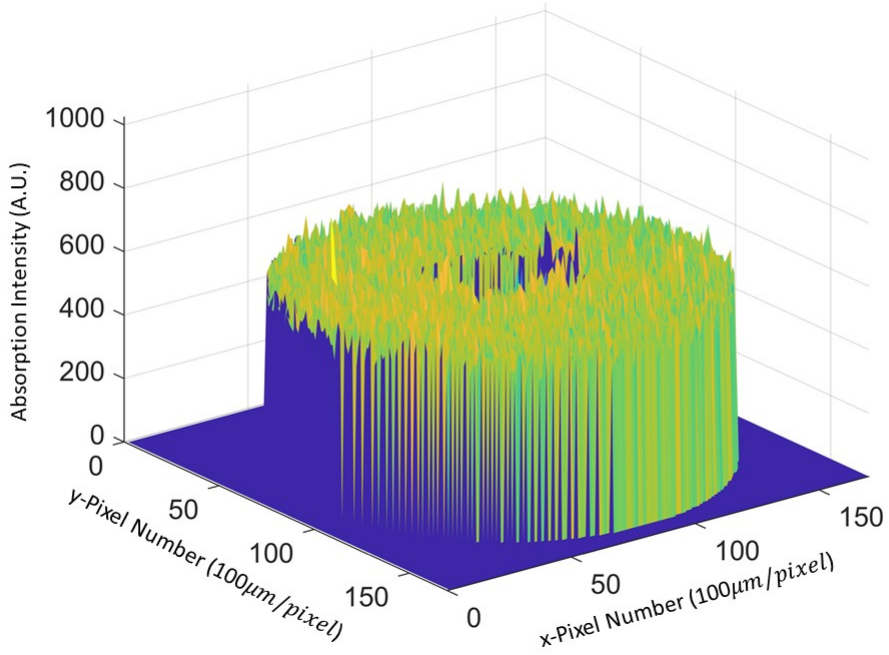

FIGURE 40. Example extracted cell image that has been colorized and converted to a 3-dimensional plot for visual examination.

The peak properties calculated by peakfit.m were used to quantify the image results from the neutron images so that the images from before degradation experiments could be compared to

images of the degraded cells. The results of the initial neutron imaging experiment are summarized in Table 6, showing each cell's quantified image data. In this table, cells that were not used for a degradation test were excluded even though neutron imaging data was collected for them. The peak position and average pixel intensity represent the amount of neutrons that were absorbed by the cell and could indicate the state of charge of the cell, presence of plated lithium, and changes in lithium concentration as discussed in Section 7.3.6. The peak width could be a measure of neutron scattering and an indicator of the composition of the cell. The MNRC was not designed to measure neutron scattering angles, so scattered neutrons would be detected as a slightly different intensity from a directly transmitted neutron as they would have had to travel slightly farther through the cell. Likewise, as the cells degrade and secondary reactions in the cell result in formation of new compounds that have different neutron capture cross sections, the peak width of the cell would be expected to increase [235].

9.1.2 Results Before Degradation

Each column of Table 6 was evaluated for correlation with cell SoH. This was done by calculating the correlation coefficient with the SoH data from Table 5. It was found that none of the quantitative measures in Table 6 had a correlation coefficient with the SoH of the cells greater than 0.1, which effectively meant no correlation. Unfortunately this was not determined until after the start of degradation testing, which prevented performing additional NR studies to improve the methodology for "before" images. Potential factors leading to this could include non-uniform cell SoC and taking cell images on three separate imaging trays. Based on this, some improvements were made to the imaging process for the "after" images, which will be discussed in the following section. On the other hand, the main goal of the NR study was not to measure SoH, since this was readily measurable in the lab, but to measure lithium dendrite growth and plating, neither of which were expected to be visible on the new cells. This limited the value of the initial NR imaging results, but provided lessons that enabled the final NR images to be useful.

TABLE 6: Neutron imaging results for all cells before degradation experiments. All units are in 10-bit grey scale pixel intensities. *Int.* is short for *intensity*, *Pos.* is short for *position*

Cell	**Experiment**	**Peak Position**	**Peak Height**	**Peak Width**	**Avg. Int.**	**Total Int.**
16	calendar avg SoH	542	240	87	534	8030152
25	calendar avg SoH	550	249	86	539	8159212
65	calendar avg SoH	546	248	86	533	8081487
8	calendar max SoH	558	251	87	555	8263176
11	calendar max SoH	563	246	90	558	8347334
12	calendar max SoH	552	240	90	546	8185580
48	calendar min SoH	540	237	90	532	7995258
54	calendar min SoH	570	254	88	565	8449506
69	calendar min SoH	563	243	91	560	8339339
5	ideal pack C1	569	244	92	564	8426021
21	ideal pack C2	560	244	90	556	8287711
28	ideal pack C3	568	244	91	564	8414102
57	ideal pack C4	563	263	85	558	8352994
70	ideal pack C5	544	243	88	539	8048149
22	individual avg SoH	553	242	90	549	8178671
40	individual avg SoH	552	242	90	546	8186121
41	individual avg SoH	563	247	89	554	8343122
4	individual max SoH	561	248	89	558	8311819
52	individual max SoH	567	249	90	563	8412189
62	individual max SoH	567	252	89	561	8395207
9	individual min SoH	540	243	86	534	7999869
45	individual min SoH	547	256	83	534	8110216

64	individual min SoH	543	255	85	529	8046320
2	neutron radiography	589	251	93	572	8763375
10	neutron radiography	612	247	97	599	9093432
13	neutron radiography	610	253	97	598	9086280
61	neutron radiography	603	245	98	589	8954184
66	neutron radiography	596	252	96	582	8855820
73	neutron radiography	584	247	94	570	8673724
74	TG pack 1 C1	553	259	83	546	8209818
55	TG pack 1 C2	541	259	82	535	8044236
42	TG pack 1 C3	525	258	78	519	7792872
20	TG pack 1 C4	522	262	77	518	7761054
17	TG pack 1 C5	523	257	79	518	7762680
56	TG pack 2 C1	605	244	97	599	8973855
49	TG pack 2 C1	574	246	92	566	8520406
44	TG pack 2 C2	570	246	91	563	8453474
43	TG pack 2 C3	554	235	92	542	8213763
15	TG pack 2 C4	574	246	91	561	8509098
14	TG pack 2 C5	575	246	93	570	8532164

9.1.3 Results After Degradation

The first improvement to the NR experiment after cell degradation was to improve the consistency of the cell SoC during imaging. This was done by combining the cell capacity test with the constant voltage hold at 3.29 V. The reason this resulted in improved cell SoC consistency was that for the initial test, cells had been used for various (and some none at all) characterization tests, then left in storage for differing time periods. After this, they were then subjected to a CCCV charge to 3.29 V. However, given the large hysteresis of LFP cells [40, 236], this likely resulted

in non-uniform SoCs between the cells. To remedy this, the 3.29 CCCV charge was appended to the end of the cell capacity test. This ensured that each cell started the CCCV charge from the same voltage and recent cycling history. The next change was taking the neutron image of all cells simultaneously, instead of ac cross three separate imaging events, this removed any image-to-image discrepancy, and even meant that when not comparing to the "before" images, the image normalization procedure was not required. Last (and least), the insulation tape method was standardized such that the tape layer was flatter and did not wrap around the cell.

The full table of NR imaging data after the degradation experiments is provided in Table 7. Similarly to Table 6, attempting to correlate the any column of Table 7 with cell SoH resulted in a correlation coefficient of 0.1 or less. Despite the applied image normalization, no pattern was observed when comparing the NR images from before degradation to after degradation. For example, the correlation coefficient for the change in SoH of the cells with the change in average NR absorption intensity was 0.00. Other metrics from Tables 6 and 7 were not any more useful. However, as previously noted, the NR results correlate to more complex behaviour than simply cell capacity and the cycling conditions of the cell must be taken into account when interpreting the NR imaging results. Also, the improved methodology for cell preparation for NR imaging after degradation may have reduced the comparability of the before and after NR images. Interesting results can be seen by concentrating on cell groups by their degradation experiment.

TABLE 7: Neutron imaging results for all cells after degradation experiments. All units are in 10-bit grey scale pixel intensities *Int.* is short for *intensity*, *Pos.* is short for *position*

Cell	**Experiment**	**Peak Position**	**Peak Height**	**Peak Width**	**Avg. Int.**	**Total Int.**
16	calendar avg SoH	593	236	98	578	8791485
25	calendar avg SoH	590	246	93	571	8756872
65	calendar avg SoH	576	235	94	558	8547143
8	calendar max SoH	583	226	100	579	8638759

11	calendar max SoH	598	233	99	594	8867931
12	calendar max SoH	568	220	100	563	8417291
48	calendar min SoH	561	239	90	547	8329810
54	calendar min SoH	578	242	92	566	8577927
69	calendar min SoH	576	243	93	560	8546758
5	ideal pack C1	557	238	89	544	8261044
21	ideal pack C2	582	244	93	567	8619698
28	ideal pack C3	584	247	92	568	8656340
57	ideal pack C4	579	244	91	568	8589040
70	ideal pack C5	575	240	92	572	8524549
22	individual avg SoH	556	235	91	548	8245509
40	individual avg SoH	580	235	96	574	8597897
41	individual avg SoH	572	233	95	563	8481988
4	individual max SoH	578	232	97	577	8561717
52	individual max SoH	563	237	92	562	8335313
62	individual max SoH	584	243	94	583	8647908
9	individual min SoH	554	246	87	549	8205601
45	individual min SoH	568	248	88	562	8409065
64	individual min SoH	569	248	89	566	8435096
2	neutron radiography	548	232	91	538	8126867
10	neutron radiography	573	239	93	564	8485635
13	neutron radiography	583	239	95	572	8645157
61	neutron radiography	581	236	95	573	8604209
66	neutron radiography	582	242	93	575	8632060
73	neutron radiography	580	234	97	573	8595009
74	TG pack 1 C1	585	237	95	579	8666646
55	TG pack 1 C2	576	232	96	574	8517923

42	TG pack 1 C3	559	237	91	551	8275240
20	TG pack 1 C4	530	228	90	525	7867145
17	TG pack 1 C5	560	243	90	551	8297212
56	TG pack 2 C1	581	245	92	580	8607203
49	cell failed	-	-	-	-	-
44	TG pack 2 C2	585	238	95	581	8664802
43	TG pack 2 C3	589	244	95	583	8721116
15	TG pack 2 C4	581	243	93	577	8615123
14	TG pack 2 C5	552	239	89	547	8179954

Figure 42 shows the average intensity of neutron absorption for all the cells connected in the TG packs. The pattern observed in this figure suggests that the coldest cell in TG1 experienced the most lithium plating, while capacity test data also showed that it degraded the most. Then as cells became warmer, their degradation was reduced (i.e. the amount of active lithium increased), but the amount of lithium plating was reduced. At TG 1 C4 ($17.5°C$), no more lithium plating was measured, at the same time as some capacity degradation. Then, at the warmest cell which degraded the least, the impact of remaining lithium in the cell became the more important, so that the average absorption intensity increased again. For the TG Pack 2 cells, no lithium plating was expected, and so their degradation should have been primarily caused by loss of lithium to side reactions, and this should have increased as the cells became warmer. This is the pattern that the neutron absorption follows for TG Pack 2 in Figure 42. In fact, for TG Pack 2, the correlation coefficient between neutron absorption intensity and SoH was 0.9. This runs counter to the statement made previously that there was no correlation between SoH and neutron absorption intensity. The explanation for this may be that the entire population of cells contained cells degraded in various ways that all affected the neutron imaging response differently. Whereas by looking at sets of cells treated similarly, these methodological differences could be removed so that the data were more comparable. On the other hand, the fact that the majority of the TG Pack 2

cells showed similar absorption intensities to the coldest cell in TG Pack 1, despite the expectation that TG Pack 1 cell 1 should have had the most lithium plating suggests that the sensitivity of the NR results was insufficient to draw any firm conclusions.

Given the inconsistency of the NR results, this data was not used during the analysis of the TG cell data as presented in previous sections to compare cells before and after degradation. There was insufficient change in the neutron absorption between the *before* and *after* NR images, with some cells observing an increase in absorption, while others showed a decrease, with no discernible pattern over the whole cell population. This can be seen from Tables 6 and 7. This, combined with the lack of a correlation between SoH, cycling temperature, or any other observed parameter meant that any analysis was subject to high error. Potential reasons for the lack of positive results from these experiments include factors from both the battery side and the reactor side. From the cell side, the NR images were taken while the cells were charged to 50% SoC, but given the large hysteresis associated with LFP cells [40, 236] combined with the relatively flat voltage curve in the 50% SoC range, it was possible the cells were not *exactly* at the same SoC for each imaging experiment. This may have been avoidable by performing neutron imaging with the cells charged to 100% SoC, as the charging method to reach 100% was well defined by the cell datasheet, and that voltage curve in that region is not flat. Factors on the reactor side include an imaging resolution that was too low to identify layers within the cells, non-constant beam intensity, and a lack of filtering of neutron energy/wavelength distribution. The above analysis method attempted to compensate for these reactor-related inconsistencies, but were clearly unsuccessful. Further research may be required to define the optimal methodology to image LIBs at the MNRC to compensate for some of the reactor's shortcomings.

9.2 Calendar Aging Results

The results of the calendar aging study are shown in Figure 43 and include data from the extra cells that were not used for other experiments and were stored at room temperature during the entire duration of testing. The calendar aging of the cells at the specified temperatures was completed over the same 16 month period that the TG packs took to complete 1000 cycles. This

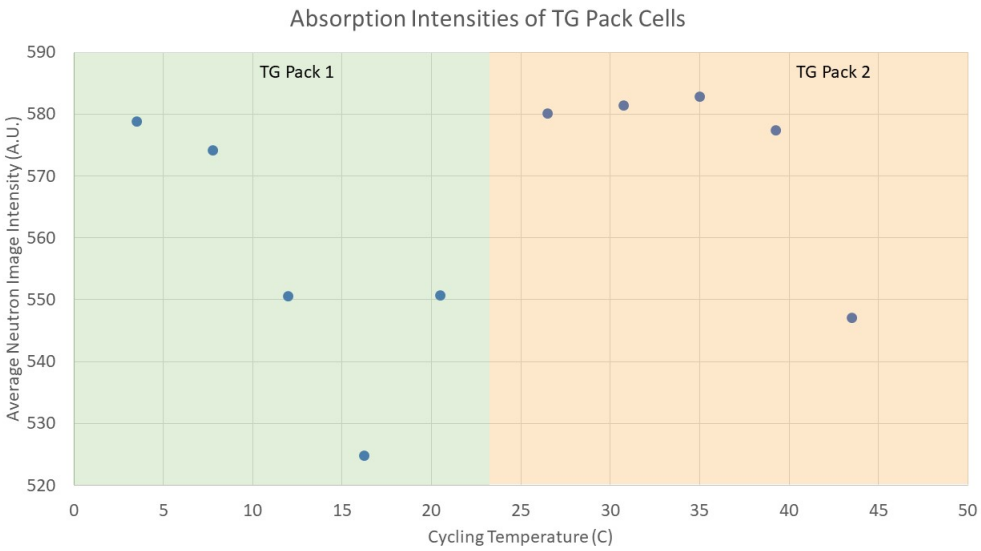

FIGURE 42. Average absorption intensities for the cells cycled in the TGS after degradation. The green shaded area indicates TG Pack 1 and the orange shaded area indicates TG Pack 2.

allowed for the results of the calendar aging to be compared to the aging experienced by the cycled cells in the TG packs and to the cells cycled individually.

From Figure 43, it can be seen that the cells aged at $5°C$ and $20°C$ gained a small amount of capacity equivalent to a 1.5% SoH increase. Every single cell in the calendar aging experiment that was stored at less than $45°C$ gained capacity relative to its initial characterization test. This behavior was indicative of incomplete cell formation before the initiation of the experiment. Other works have found similar results for calendar aging of cells when the cells used were cycled very few times (around 3) before beginning of the calendar aging experiment. One proposed explanation for the mechanism behind this increases capacity is the increase in electrode surface area caused by electrochemical milling, or cracking of the electrodes when the first set of stresses (i.e. charge/discharge cycles) are applied to the cell [237]. Over time and increased cycle number, this would lead to increased degradation due to the increased area for SEI layer formation, but for the low number of cycles associated with calendar aging experiments, this could easily result in a measured capacity increase [238, 239]. Another factor favoring this was that for the lower storage temperatures, the side reactions that form the SEI layer progress more slowly, especially

with the lack of lithium ion transfer. Therefore, the increased contact area of the electrode with the electrolyte would by sustained over a longer period of time. This effect is especially common for calendar aging experiments for cells stored at lower SoCs and lower temperatures, those being at or below 50% SoC and below 30 degrees C. This is because the side reactions at those temperatures are much slower [240].

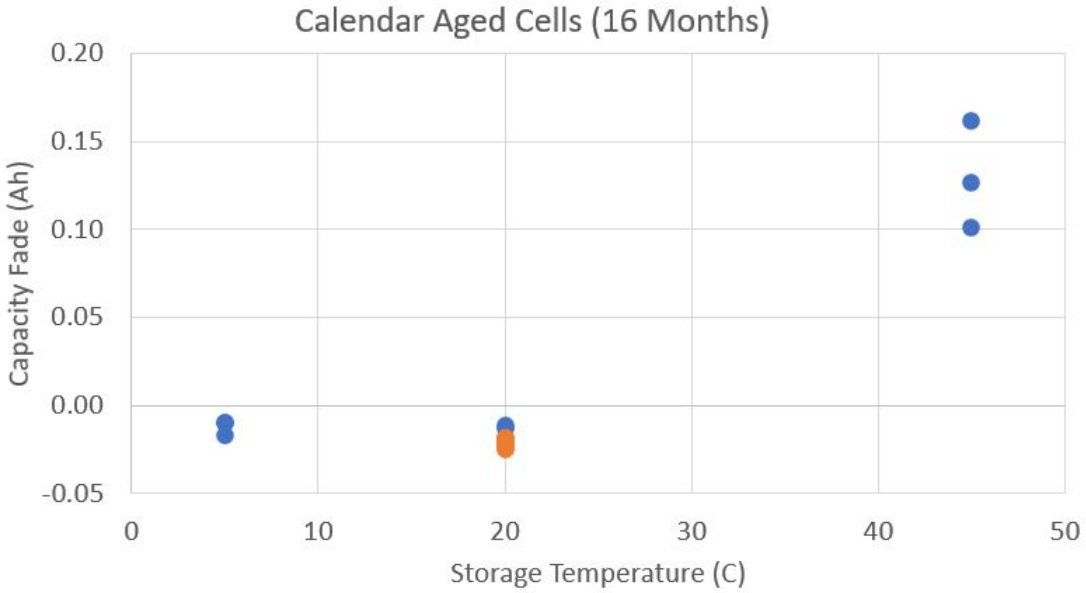

FIGURE 43. Capacity fade of the cells subjected to calendar aging plotted against storage temperature. Blue indicates cells which were specifically chosen for the calendar aging study while orange represents the cells that were initially tested but not used for any experiment.

9.3 Individual Cycling Result

The results from the individual cycling test are shown in Figure 44. In general, the cells cycled at $45°C$ degraded more and faster than the cells cycled at $22°C$. However there were two exceptions to this. First, the cell labeled *Max 22* was cycled at $22°C$ was observed to follow a different degradation trajectory compared to the other cells. Every other cell for which cycle 200 data existed saw an increase in capacity at cycle 200 compared to cycle 0. Meanwhile, cell Max 22 started at cycle 0 with a capacity similar to the cycle 200 capacity of cells Max 45 and Avg 22, and immediately began its linear degradation trend. This behavior might be expected had cell

Max 22 been cycled several times before the beginning of this experiment, however that was not the case because the initial capacity check was the first test run on all the cells. Two potential causes of this behavior could be random manufacturing variations of the cells, or perhaps the cell was selected for a small number of quality control cycles at the factory.

The next cell that behaved unexpectedly was cell *Max 45*. This cell was cycled at $45°C$, but degraded similarly to the cells cycled at $22°C$. Interestingly, between cycles 200 and 800, it can be seen to have had a degradation rate higher than the $22°C$ cells, but the rate then slowed at cycles 800 and 1000. This resulted in the cell losing a similar capacity in Ah compared to the other cells cycled at $45°C$, but due to its higher initial SoH, ended the test with similar capacity to those cells cycled at $22°C$.

The increased capacity seen in the degradation trajectories in Figure 44 was not unexpected behavior. This is a commonly measured effect with new cells and with cells that have been in storage for a long period of time. See Sections 9.2 and 9.4.1 for more detailed explanations on these two factors.

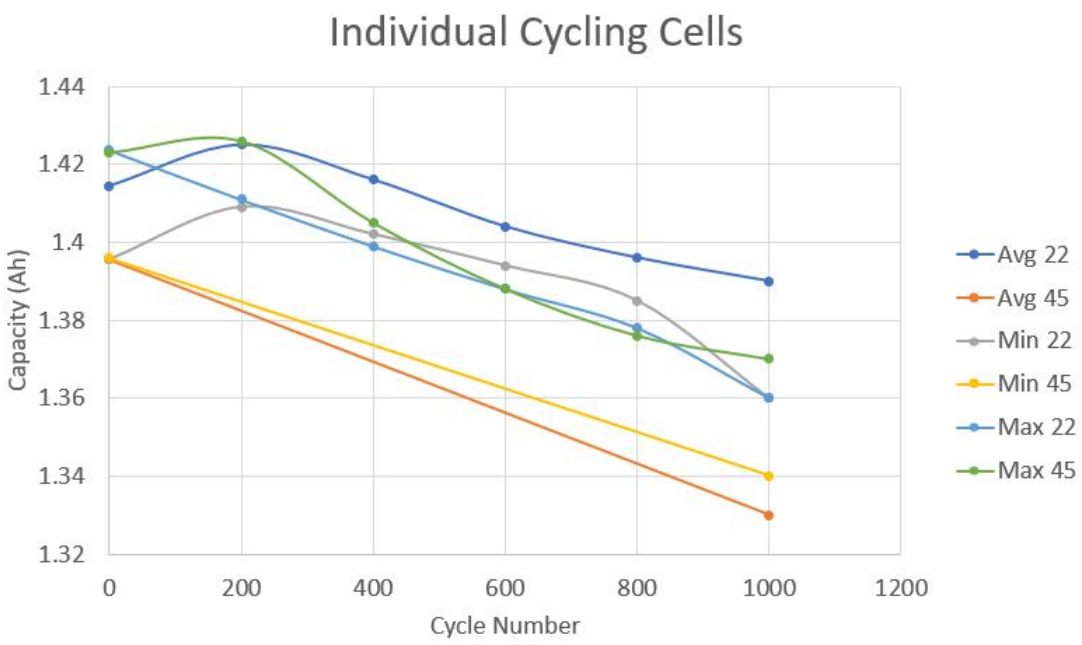

FIGURE 44. Capacity fade of the cells cycled individually at various temperatures plotted against cycle number.

9.4 Temperature Gradient Pack Degradation Data

After 1000 cycles, the cells in all cycled battery packs had degraded noticeably, but each had a different pattern of degradation. Cycling data was assessed based on the voltage measurements obtained by the National Instruments NI 9205, which provided noisy data for some cells. To facilitate analysis, this data had to be cleaned. This was done by using the moving average method and a sliding window of 5 data points which amounted to 0.333 seconds per window and provided satisfactory noise reduction in the data. However, for TG 1 cell 5 on cycle 1000, TG 2 cells 1, 2, and 4 on cycle 1, a sliding window of 15 data points (1 second) was required to smooth the data. Note that the voltage data from cycling was primarily used for qualitative analysis. This was because the cells were not fully cycled (there was no constant voltage charge) during the test, and each cell was cycled to a different voltage. Quantitative measurements were made using the checkup tests performed every 200 cycles on each cell individually.

9.4.1 Temperature Gradient Pack 1

TG Pack 1 was the coldest pack with a temperature gradient applied and cells in the range of $3.5°C$ to $20.5°C$. Cycle data for TG Pack 1 for cycles 2 and 999 are shown in Figure 45. Note that for these comparisons, Cycles 2 and 999 were chosen to avoid inconsistent voltage response data from cycles 1 and 1000. For example, cycle 1 started from 50% SoC due to being run after a capacity test, and by using 999 instead of 1000, the entire plotted voltage profile of the cycle plus the first few minutes of cycle 1000 better matched the plot of cycle 2. Also, recall that for the TG packs, cells were numbered such that cell 1 corresponded with the negative cell of the pack, and with the coldest cell in the pack while cell 5 corresponded with the most positive cell in the pack and the warmest.

From Figure 45, the reduction in pack performance over 1000 cycles can be clearly seen. However, it was also the case that the impact on pack performance, specifically on operating voltage, of the large temperature difference was larger than the degradation of the pack. This can be seen from the fact that the voltage curves of packs overlapped even at the end of discharge. This can be seen by comparing the performance of cell 1 from cycle 2 with the performance of cell 5 from cycle 999 where even during cycle 2, the effect of the temperature gradient was large enough to reduce cell 1's performance more than cell 5 degraded over 998 cycles.

When comparing the charge step to the discharge step, it can clearly be seen that cell 1 was the limiting cell for both the charge and the discharge step. As it was the coldest, it had the highest resistance, so the largest voltage drop. The meant that, when charging, it had the highest voltage and reached the charge cutoff voltage much sooner than the rest of the cells, preventing them from being fully charged. Then, during the discharge, cell 1 immediately became the lowest voltage cell, and again reached the discharge cutoff sooner than any other cell. This was true for both cycle 2 and cycle 999. This suggests that despite cell 2 being cycled at lower temperatures, which would typically help reduce most electrochemical aging mechanisms as discussed above, it did not degrade slower (and in fact degraded faster) than the warmer cells. However, seemingly conflicting with this, at the end of discharge there was clearly a smaller voltage difference between cell 1 and cell 5 in cycle 999 than in cycle 2 by 0.073 V. This would be expected had the warmer cells degraded

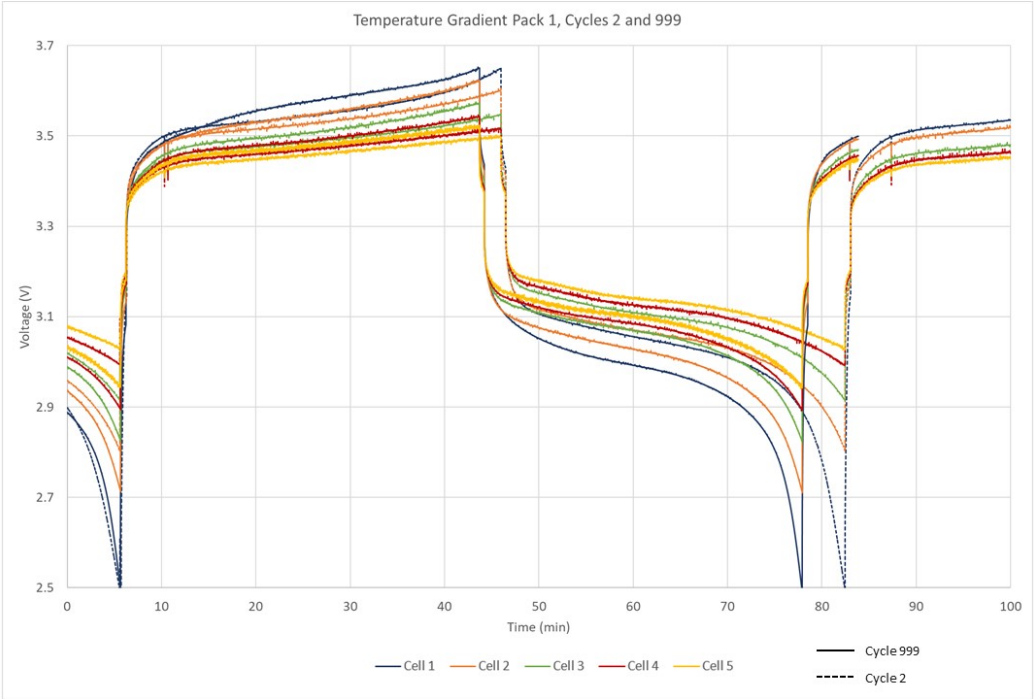

FIGURE 45. Plot of cell voltages from TG pack 1 during cycle 2 compared to cycle 999. List of cell number and cycling Temperatures (Cell #, $T°C$): C1, $3.5°C$; C2, $7.8°C$; C3, $12°C$; C4, $16.3°C$; C5, $20.5°C$

more quickly than cell 1. In this case, this was likely caused by the fact that the voltage drop is much faster near the end of discharge of the cells, so even though cell 5 only degraded slightly, this made a relatively large impact on its voltage near the end of discharge.

Figure 46 shows a detail of Figure 45 from 4-10m, which shows the end of discharge, the rest while the relay reset, and the beginning of charge. Considering cell 1 cycle 2, the voltage recovered from the discharge much faster than after cycle 999. This indicates lower diffusion resistance for the un-aged cell. Interestingly, at the start of charge, cell 1 cycle 1 had a higher voltage than cell 1 cycle 999. Typically, it would be expected that the degraded cell with higher resistance would have a higher voltage during charging. This can be explained by slow diffusion in the aged cell, possibly due to increased SEI layer thickness, or damage to the structure of the electrodes. Then, since charging occurs immediately after discharging, there would be more sites available for Li ions to bind to the surface of the electrodes as ions from deeper in the electrode did not have a chance to diffuse to the surface yet. This would be a short term effect, and eventually the more degraded

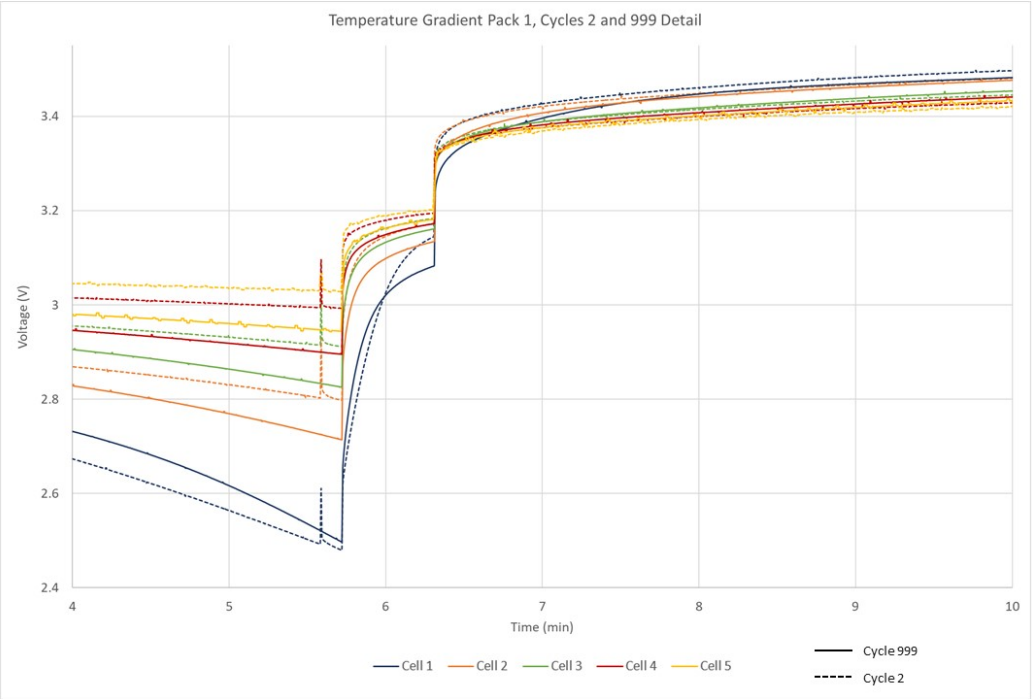

FIGURE 46. Detail of cell voltages from TG pack 1 during cycle 2 compared to cycle 999 focusing on the switch from discharging to charging. X-Axis is Time (1/10 s), Y-Axis is Voltage (V).

cell would have a higher voltage than the new cell. Looking again at Figure 45, this is exactly what is seen. After about 10 minutes of charging, the degraded cell 1 became the highest voltage cell as would be expected. This behavior suggests more than simple capacity fade occurred to the cell, and that its overall performance was damaged. When comparing cell 1 to the other cells in TG1 in Figure 46, it can be seen that they showed similar behavior, but to a less extreme degree as befitting their lower degradation.

Based on the data collected during the capacity tests every 200 cycles and shown in Table 8, Figure 47 shows the trend of capacity fade for each of the cells in TG Pack 1. The feature of this plot that immediately jumps out is that the capacity after 200 cycles was higher than the initially measured capacity. This was likely the result of two well-known phenomenon. The first was discussed in the Calendar Aging Results (Section 9.2), and the second is known as the capacity recovery effect. It is an artifact of how the cells are made with larger anodes than cathodes which allows lithium to migrate to an inactive area if the cell is rested for a long period of time

(multiple weeks or months). This results in less lithium in the anode being readily accessible during discharging. However, when discharging or cycling, the lithium concentration gradient in the anode eventually brings the lithium ions back into the usable area of the anode, resulting in the recovery of the lost capacity [241, 242]. In the case of the first 200 cycles, the resting that caused the capacity increase was the delay between cell manufacturing, purchasing, and the beginning of the experiment. After the beginning of the experiment, there were only minimal resting periods of a few days between tests, minimizing the effect of the anode overhang.

Figure 47 Left also shows the high degree of consistency of the cells chosen for pack TG1, and shows how their capacity diverged as they aged. Note that the capacity values shown in Figure 47 Left and Table 8 were measured at $20°C$ and thus do not include any temperature gradient effects. As initially expected of the colder TG pack, cell 1 (the coldest cell) degraded the most and finished the experiment with the lowest capacity. This trend continued perfectly from coldest cell to warmest cell, with colder cells experiencing greater degradation than the warmer cells. The effect of the temperature gradient on cell aging was significantly lower for cells 3 - 5, or from $12 - 20.5°C$ compared to cells 4 and 5, or $7.8 - 3.5°C$. This suggested a similar temperature dependence for aging at low temperatures as internal resistance, and this was confirmed by fitting the Arrhenius equation to the capacity reduction observed after 1000 cycles. This was done using the same methodology as for the resistance data, and with $T_{ref} = 12°C$ and $Q_{ref} = 0.036Ah$ from cell 42 in Table 8. The result is shown in Figure 47 Right, and the fit was better than for the internal resistance. This heavily implies that an electrochemical, rather than mechanical, process was responsible for the reduced cell capacity. However, note that the degradation is predicted to decrease as temperature continues to increase. This clearly is not the case for LIBs which, as discussed above, degrade significantly faster when exposed to elevated temperatures. Therefore, this result would seem to be contrary to most literature, aging models, and other results presented herein, that predict (and have shown) increased aging at increased temperatures. On the other hand, cycling cells at low temperatures has also been shown to increase degradation rates [126, 166, 243], despite the still common assumption made among some authors that degradation is slower at lower temperatures [6]. The implications of this increased

low temperature degradation for packs with temperature gradients is discussed further below.

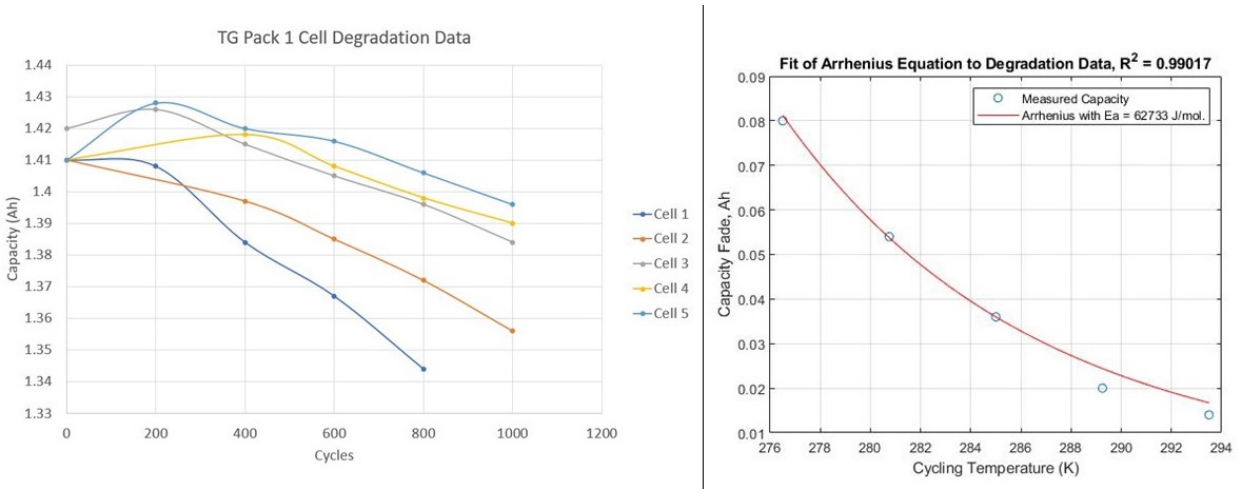

FIGURE 47. Left) Plot of cell capacities for each cell in TG pack 1 over the degradation experiment. Cell 1 capacity is not shown for 1000 cycles because it failed and was not able to be tested. Right) Fit of Arrhenius equation to the observed degradation after 1000 cycles. Fit is based on the change (reduction) in capacity observed, not absolute capacity of the cells.

9.4.2 Temperature Gradient Pack 2

TG Pack 2 was the warmest temperature gradient pack, with cell temperatures in the range of $26.5°C$ to $43.5°C$. Cycle data for TG Pack 2 for cycles 2 and 99 are shown in Figure 48. Cycles 2 and 999 were chosen for the same reasons as for TG Pack 1. Similarly to TG Pack 1, cell 1 was the coldest cell in the pack, and the lowest voltage cell in the pack while cell 5 was the warmest and most positive cell in the pack.

From Figure 48, it is again clear that the pack experienced degradation due to cycling. For this pack, the operating voltage curves at cycles 2 and 999 appear similar except that cycle 999 was compressed in the time axis. However, examining the discharge curve more closely from the inset of Figure 48 shows that the voltage drop along the entire discharge portion of the curve was lower than the lowest voltage cell from cycle 2. This lack of overlap of any cell voltages for any portion of the discharge curve implies that cell degradation had a larger impact on the pack's operating voltage than the temperature gradient. This is in contrast to TG Pack 1 where the

significant overlap in discharge curve voltages showed that the performance degradation caused by the temperature gradient was more significant than the effect of degradation. There are two possible causes of this. First, degradation was higher for TG pack 2, as seen in Table 8, with the average capacity loss of the cells in TG pack 1 being 0.04 Ah, and for TG pack 2, the average was 0.05 Ah (25% higher). This increased degradation would result in lower working voltages of the pack. The second, compounding reason for the degradation to be more significant than the temperature gradient for TG pack 2 is related to the temperature's influence on resistance as shown in Figures 35 and 36. Specifically, that at increased temperature, the magnitude of the change in resistance for each ΔT is smaller. This means that TG Pack 2 had a smaller range of cell resistances than TG Pack 1 due to the increased cell temperatures in TG Pack 2. This in turn resulted in a narrower range of operating cell voltages, as can be seen by comparing Figures 45 and 48. The tighter grouping of cell voltages meant that the reduced operating voltages caused by cell degradation were more apparent for TG Pack 2 than for TG Pack 1.

Now, considering the individual cell cycling profiles in TG Pack 2, it can be seen that similarly to TG Pack 1, the 'order' of the cells was reversed for charge and discharge. For example, cells 4 and 5 had the lowest voltage during charging, and the highest voltage during discharging. This is typical behavior and is a result of the lower resistance of the warmer cells and thus their reduced overpotential. During cycle 2, cell 2 (the second-coldest cell) was the cell that triggered the end of charge by reaching 3.65 V first, but during cycle 999, cell 1 triggered the end of charging. This suggests that cell 1 degraded faster than cell 2, and this is what is seen in Table 8. At the discharge end of cycle 2, cell 1 reached the cut-off voltage first, ending the discharge, as might be expected of the coldest cell. The fact that cell 1 did not also trigger the end of charge in cycle 1 may be explained by the initial SoH of cell 1 being slightly higher than that of cell 2, which was responsible for triggering the end of charge during cycle 2. Unlike in TG Pack 1 where the relative performance of the cells to one-another remained generally the same, in TG Pack 2 degradation caused the cell performance distribution to shift over time. However, this performance change was only seen near the end of charge and end of discharge when the voltage curves of the cells became steep. Additional cycles and degradation would be required to further emphasize these changes

and shift them closer to the center of the charge/discharge curves.

More closely examining cell 5, during the bulk of the charging phase of both cycles 2 and 999, it had the lowest voltage, implying the lowest resistance and best performance. But during cycle 999 near the end of the charge, cell 5 began to overtake cells 3 and 4, showing that it had exhausted its capacity faster than the other cells. So, despite having better performance for most of the charge, cell 5 actually had a lower SoH than the other cells which implies it degraded more than the other cells. A similar pattern is observed in the discharge portion of the curve where cell 5 had the highest voltage (again, best performance) during the bulk of the discharge in both cycles. In cycle 2, cell 5 had the highest voltage at the end of the charge as well, showing its higher performance however, by cell 999, cell 5 was the lowest voltage cell and the one causing the end of discharge. It can be seen that right as the voltage curve begins to increase in slope near the end of discharge in cycle 999, cell 5's voltage began to fall much faster than the rest of the cells. Why then, if cell 5 was weaker than the rest of the cells, did it not also cause the end of charge during cycle 999? It can be seen that cell 5 was in the process of 'overtaking' the other cells, but that the charge ended before it did. The reason this was seen in the discharge before the charge, was that the voltage change at the end of discharge was much more dramatic than at the end of charge, with the exponential region of the charge curve accounting for a voltage change of only about 0.15 V while the end of discharge has a voltage change of 0.5 V. It is likely that degrading the cells for additional cycles would eventually result in cell 5 causing both the end of charge and the end of discharge.

Figure 49 shows the capacity fade trend of the cells for TG Pack 2 using the data from the capacity tests performed after every 200 cycles and shown in Table 8. Note that the initial capacity of the cells chosen for TG Pack 2 were in the same range as the initial capacities for TG Pack 1. Similarly to Figure 47, at cycle 200, the cells all had higher measured capacities than during cycle 1. This was again attributed to the capacity recovery effect and electrochemical milling. By 400 cycles, the cell capacities had returned to near their initial values and the cells had already organized their capacities by cycling temperature, with cell 1 (the coolest) having the highest

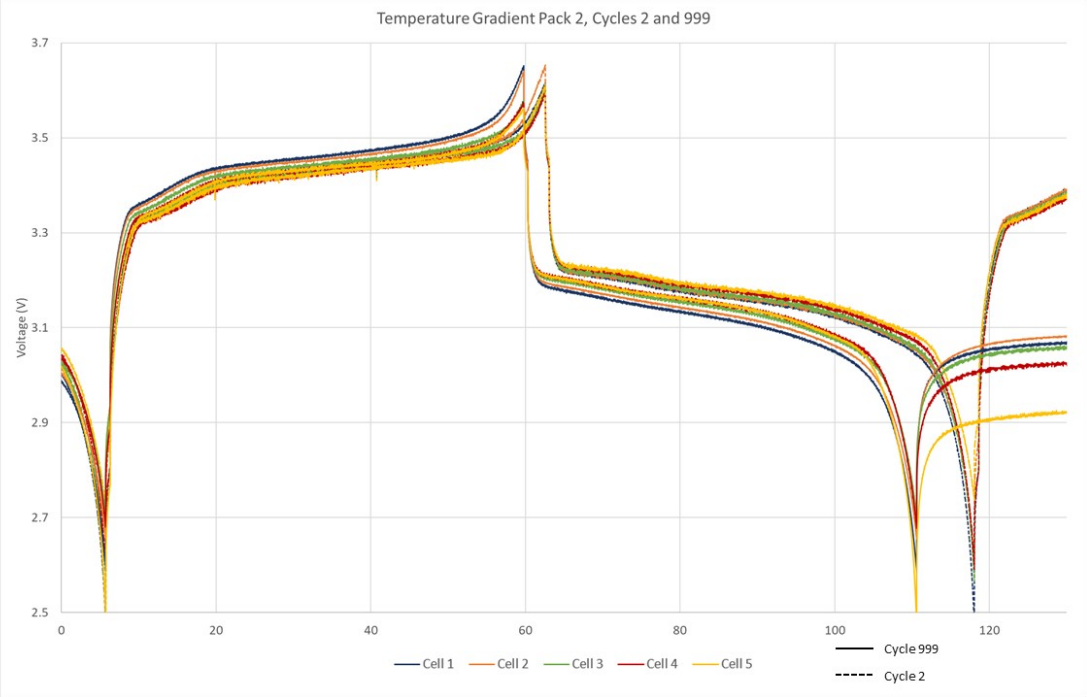

FIGURE 48. Plot of cell voltages from TG pack 2 during cycle 2 compared to cycle 999. List of cell number and cycling Temperatures (Cell #, $T°C$): C1, 26.5°C; C2, 30.8°C; C3, 35°C; C4, 39.3°C; C5, 43.5°C. The inset shows the discharge curve where both cycles have been aligned to the start of discharge, compared to the main plot which is aligned to the start of charge.

capacity and cell 5 (the warmest) having the lowest capacity. This matched the expected result for TG Pack 2, but was contrary to the results from TG Pack 1. This trend then continued through cycle 800, but with cell 5 widening the gap by degrading faster than the rest of the cells.

From Figure 49 right, the fit of the Arrhenius equation to the degradation of TG Pack 2 can be seen, which was generated in the same manner as for TG Pack 1 except the reference values were taken at 30.8°C. The figure shows that for increasing temperature, cell degradation was predicted to increase. This matches the accepted degradation behavior of lithium-ion cells in the literature. The sign of the activation energy was opposite of that found for TG Pack 1, and of very similar magnitude (being only 4% smaller). The opposing sign matched with the finding that for TG Pack 2, the warmer cells degraded more where as in TG Pack 1 the cooler cells degraded more.

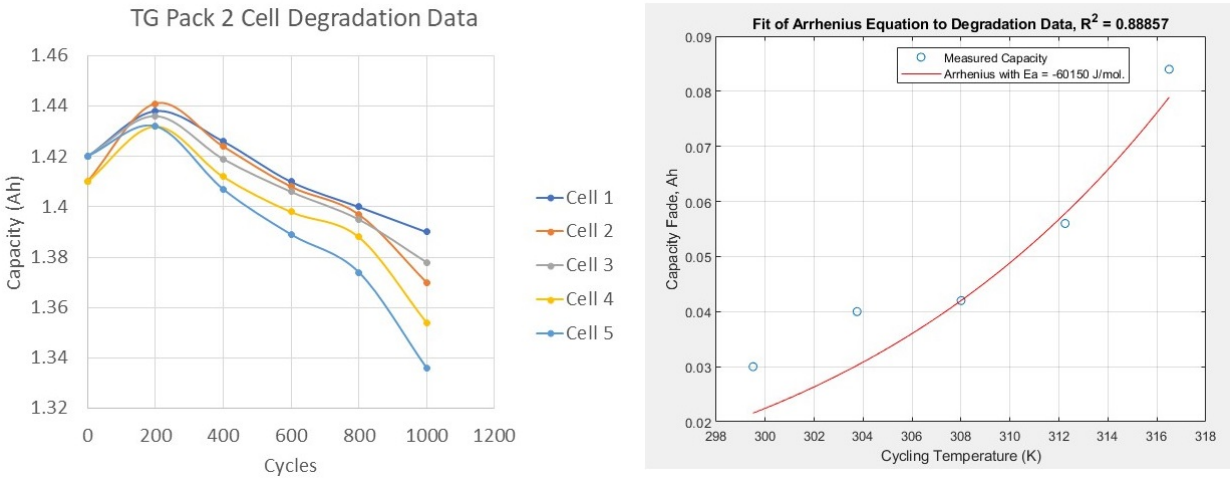

FIGURE 49. Left) Plot of cell capacities for each cell in TG pack 2 over the degradation experiment. Right) Fit of Arrhenius equation to the observed degradation after 1000 cycles. Fit is based on the change (reduction) in capacity observed, not absolute capacity of the cells.

This reduced impact of resistance on cell voltage at increased temperature has implications for battery pack performance, degradation, and monitoring. Since the resistance change is relatively small, the cell voltages remain similar which makes detection of the temperature difference more difficult. Additionally, even in the long term, if the same temperature profile is maintained in the pack, the increased temperature on the hottest cell increases its short term performance sufficiently to mask its additional degradation until near the end of discharge. This may result in a BMS overestimating the SoH of the hotter cells in the battery pack. While not observed in this experiment, it is expected that after a large enough number of cycles, the increased degradation of the hottest cell would eventually catch up to it, and its performance will become the limiting factor of the battery pack.

9.4.3 Control Pack

The control pack was the pack cycled at $22°C$ to serve as a comparison to the TG packs. Figure 50 shows the voltage curve for the cells in the control pack for cycles 2 and 1010 due to an experimental error where the cells were improperly balanced before beginning the last set of cycles. This resulted in an effective capacity reduction of the pack of 5%, or reducing the number of

cycles done by 10. To both make up this (small) difference and recollect more representative data for the pack's performance, an additional 10 cycles were performed on the pack. As with the TG packs, the pack's performance degraded over the course of the experiment, but much less obviously. Again, the cells were numbered such that the lowest numbered cell was the lowest voltage cell in the pack, but with a lack of temperature difference, the cell numbers were expected to have no relevancy to degradation rate.

From Figure 50, it is difficult to see the difference between cycle 2 and 1010, since the cell's operating voltages remained so similar and the pack's degradation was minor compared to the TG Packs. The degradation can be observed by looking at the end of charge and end of discharge, where the steep voltage profile made the difference between the two cycles visible. It can be seen that for both cases, cell 2 was the limiting cell for both the charge voltage cutoff and the discharge voltage cutoff. Cell 2 was the lowest initial SoH cell in the pack, having started the experiment with an SoH 0.8% (percentage points) lower than the highest SoH cell in the control pack. Since no externally applied temperature effect was present to influence cell aging, it was unsurprising then that this cell remained the lowest performing cell in the pack over the course of the testing. Cycle 1010 then was notable for its similarity to cycle 2, showing that when the pack was cycled under "ideal" conditions, degradation was both minimized and the consistency of capacity fade was maintained.

Despite Cell 2 being consistently the lowest performing cell in the Control Pack, from cycle 2 in Figure 50 it can be seen that the voltages of all the cells were much more consistent than for either TG Packs 1 or 2. This also shows the effect that non-uniform temperatures have on the operating voltage of the total battery pack. In addition, since the cells reached the end of charge at very close to the same voltage, each cell had a similar actual DoD which minimized aging rate differences between the cells and leading to the similar and consistent voltage profiles of the control pack between cycles 2 and 1010. Cycle 2 shows a near ideal case of what pack cycling "should" look like, with all cells having similar capacities, resistances, and operating voltages while cycle 1010 shows the 'desired' degradation behavior of the battery pack.

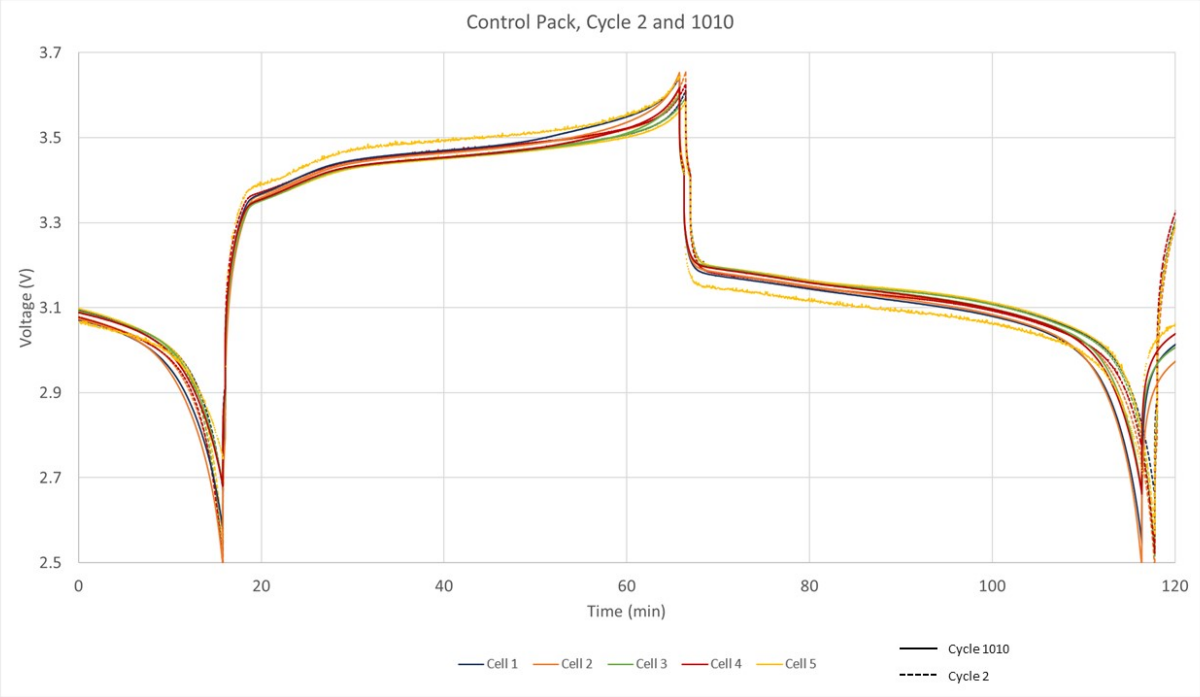

FIGURE 50. Plot of cell voltages from the control pack during cycle 2 compared to cycle 1010.

9.5 Degradation Comparison and Analysis

9.5.1 Series Packs vs. Controls

One of the primary areas of interest of this research was to evaluate the effect of temperature variation on a battery pack compared to individual cells. This effect was determined by comparing the results from the calendar aging and cycle aging tests to the results of the TG and control pack cycling results.

Calendar Aging One of the more interesting results of the calendar aging study can be observed by comparing Figure 43 to Figures 44 and 53. From these figures, it can be seen that the cells stored at $45°C$ degraded more than the cells individually cycled at $45°C$ or the cell in TG Pack 2 that was at $43°C$. This implied that calendar aging was more detrimental to cell health than cycling the cells, at least at elevated temperatures, which was counter-intuitive. It is possible that for increased time and cycle number, eventually cycle aging would degrade the cells more, as this

TABLE 8. Table of cell capacity at different stages of the experiment. Cells *TG 1* refers to the pack with an average temperature of $12°C$, *TG 2* refers to the pack with an average temperature of $35°C$, and *control* refers to the pack with no ΔT applied and tested at $22°C$. x's indicate that the cell died during testing. Dashes - indicate that no valid capacity test data could be collected. *Cell 74 cycle 1000 capacity based on linear extrapolation due to cell failure.

	Cell #	Temp ($°C$)	Ah New	Ah200	Ah400	Ah600	Ah800	Ah 1000	dAh
TG 1	17	20.5	1.41	1.428	1.42	1.416	1.406	1.396	0.014
	20	16.25	1.41	-	1.418	1.408	1.398	1.39	0.02
	42	12	1.42	1.426	1.415	1.405	1.396	1.384	0.036
	55	7.75	1.41	-	1.397	1.385	1.372	1.356	0.054
	74	3.5	1.41	1.408	1.384	1.367	1.344	1.33*	0.080
TG 2	14	43.5	1.42	1.432	1.407	1.389	1.374	1.336	0.084
	15	39.25	1.41	1.432	1.412	1.398	1.388	1.354	0.056
	43	35	1.42	1.436	1.419	1.406	1.395	1.378	0.042
	44	30.75	1.41	1.441	1.424	1.408	1.397	1.37	0.04
	49	26.5	1.4	1.43	x	x	x	x	-
	56	26.5	1.42	1.438	1.426	1.41	1.4	1.372	0.031
Control	5	22	1.42	1.428	1.414	1.407	1.385	1.39	0.03
	21	22	1.41	1.428	-	1.401	1.372	1.37	0.04
	28	22	1.41	1.425	1.416	1.41	1.387	1.382	0.028
	57	22	1.41	1.422	1.42	1.417	1.397	1.38	0.03
	70	22	1.41	1.427	1.426	1.42	1.407	1.39	0.02

would be inline with what is found in the literature [244, 245]. However, comparing results for the same number of cycles and storage time as performed in this work, some studies did observe similar results. [122, 244–246]. Therefore, the results found here may be a temporary condition of the cells due to the difference in the degradation trajectories of calendar aging compared to cycle aging. Despite this, the difference still calls for explanation as a direct discussion of it could not be found in the literature.

As of this writing, there were 2 main proposed mechanisms that could result in calendar aging at higher temperature being worse than cycling aging at the same temperature. The first, and likely

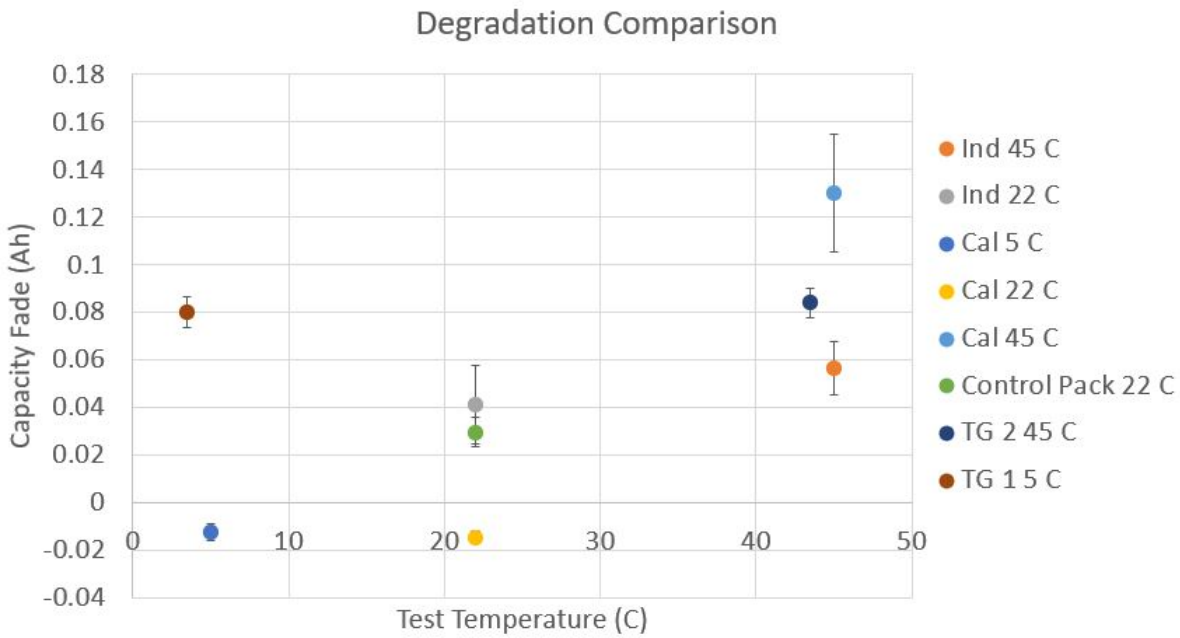

FIGURE 51. Comparison of the degradation experienced by the cells tested at different temperatures and by different degradation conditions. Error bars for individually cycled cells and calendar aged cells were calculated as the standard deviation of all cells individually cycled or stored at that temperature. The error bars for the TG Pack cells were calculated based on the standard deviation of the degradation from the control pack.

least significant, was the capacity recovery effect which was introduced in Section 9.4.1. Since the cells that were simply stored were not cycled (except for occasional capacity checks), there was ample time available for lithium ions to migrate away from the active area of the anode into the overhang. This migration would be made faster by increased temperature due to increased diffusion coefficients. But during the capacity checkup cycles, the cells were cooled to room temperature, such that the diffusion of the lithium ions out of the anode overhang was slower than diffusion into it. This effect could provide the cycled cells with an SoH advantage of up to 1.7% [242].

The second reason which was likely of larger magnitude, especially for new cells was electrochemical milling, first introduced in Section 9.2. It has been shown that for the first 50 to 200 cycles (depending on the cell's manufacturing process), the capacity of the cell may increase. This is caused by the electrode's structure cracking due to the initial stresses of charging/discharging. These cracks increase the effective surface area of the electrodes, and thus reduce the internal

resistance of the cell, increasing the available capacity. This effect has been found for cells cycled at rates above C/5. The cracking of the electrodes then allows the electrolyte to penetrate further into the electrodes, further increasing the conductivity of the cell [237–239, 247–249]. Since this effect is triggered by cell cycling, the cells that were individually cycled and the hot cell in TG Pack 2 were able to benefit from this effect while the calendar aged cells were not (as much). This increase can be seen in the plotted degradation trajectories for all the cycled cells up to cycle 200. In turn this would result in the cycled cells having reduced Ah capacity loss compared to the calendar aged cells at high temperature. While the capacity checkup cycles meant that the calendar aged cells were cycled, there may have been insufficient cycles to trigger this effect. It maybe possible that cycling the calendar aged cells for 100-200 cycles [248] could increase their capacity to a value lower than the cycled cells, but this cannot be stated definitively based on the data collected here.

As a result of the behavior of the calendar aged cells, comparison of the magnitude of calendar aging to that of cycle aging and of TG Pack aging was made difficult. Since it should be expected that the cycled cells *include* a calendar aging component, the total degradation of calendar aging should not be greater than the total degradation of cycling. Likewise for the cooler cells, it did not make sense to add a negative calendar aging component to the cycled cells, since the proposed mechanism behind the observed capacity increase for the calendar aged cells at low temperature was due to the capacity checkup cycles. Therefore, it was decided to consider the individually cycled cells to be the reference "calendar + cycling" aging to compare against the TG Pack cells. Perhaps for future studies, a sample of cells should be cycled until they reach their maximum capacity to find the cycle count where cell capacity reduction begins. Then, the entire population should be cycled to that number of cycles and the cells should be considered "new" at that point.

Individually Cycled Cells The degradation data for the individually cycled cells is summarized in Figure 51 along with the calendar and TG Pack data. The individually cycled cells at $22°C$ can be seen to have degraded similarly to the control pack cells that were also cycled at $22°C$. This was expected, and is what a pack designed would 'hope' for, as it implies that the battery pack

with no temperature gradient possessed the same lifetime as the individual cells. Therefore, for a series battery pack cycled without a temperature difference, the degradation mechanisms and rates can be said to be identical to those of the individual cells at the same temperature.

More interestingly was the comparison between the individually cycled cells at $45°C$ and the hottest cell (cell 5) in TG Pack 2. This cell was cycled at $43.5°C$, but this temperature difference was considered negligible. It can be seen that cell 5 degraded appreciably more than the individually cycled cells (50% more), despite the fact that they were cycled at a *slightly* higher temperature and therefore might have been expected to have degraded marginally more. This result was counter-intuitive mainly because the depth of discharge of the individually cycled cells was expected to be higher compared to hottest cell in TG Pack 2. This was because the coldest cell in the pack had higher resistance so would at least initially be the cells that triggered the end of charge and end of discharge, as can be seen in cycle 2 of Figure 45. This would prevent cell 5 from reaching its full charge or full discharge state while the individually cycled cells were always fully cycled. Eventually cell 5 degraded more than the colder cells and became the limiting cell, but it 'should' still have had an advantage over the individually cycled cells.

This result was thought to be explained by internal temperature gradients within the hot cell in the TG pack. Due to the construction of the TGS, the cell had an externally applied temperature difference of $2.4°C$ in the radial direction. As demonstrated in the literature, this causes uneven internal current distributions which accelerates cell aging by inducing locally higher currents and non-uniform SoC distributions within the cell which may lead to local over charging or over discharging [15, 29, 32, 182, 250]. To investigate this further, neutron images of TG2 cell 5 and of the individually cycled cells at $45°C$ were compared. Note that while the NR image data was insufficiently reliable to determine changes between separate images, it was still able to provide information within a single image.

Figure 52 shows a sample comparison between TG2 Cell 5 and Cell 62, which was individually cycled at $45°C$. It can immediately be seen that the right side of TG2 Cell 5 showed lower neutron absorption than the left side, while for cell 62 the two sides were symmetric. This was evaluated

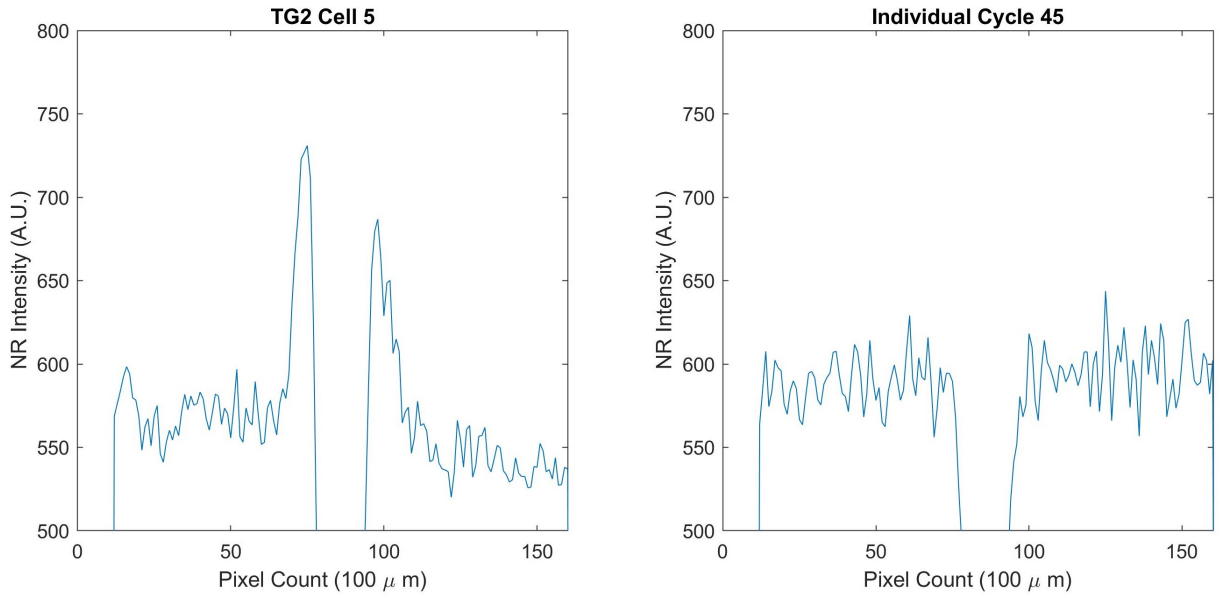

FIGURE 52. Intensity cross-sections of sample cells showing averaged pixel intensity in the radial direction through the cells.

quantitatively by averaging the absorption intensities of each side of each cell (not including the edge effects that remained in TG2 Cell 5. The right side of TG2 Cell 5 was found to be 5% less bright than the left side, while cell 62 showed a difference of only 1.6% in absorption intensity between the left and the right side. Note that the two images compared in Figure 52 were taken from the same NR image so no cross-normalization was required. This suggested that TG2 Cell 5 was subjected to non-uniform internal degradation, while cell 62 degraded mostly uniformly. Also of note, the average intensity of TG2 Cell 5 was 6% lower than the intensity of cell 62, corroborating that it had indeed degraded more.

9.5.2 Effect of Average Temperature and Temperature Difference

Figure 53 shows the measured degradation of each cell connected in a series battery pack vs the temperature at which the cell was cycled. A clear parabolic trend can be seen, with the minimum degradation occurring between $20 - 25°C$. However, the trend was not perfectly symmetric, with the warmer cells from the colder pack degrading less than the cooler cells from the warmer pack. Similarly, the warmer cells of TG Pack 1 also degraded less than the cells from the control pack.

The proposed explanation for this is that due to the low temperatures of the coldest cells in TG Pack 1, the charge and discharge voltage cutoffs were reached sooner than in the warmer pack. This resulted in a smaller depth of discharge for TG Pack 1 than TG Pack 2. Then, since the test station counted cycles rather than total cycle capacity, the Ah throughput of TG Pack 1 was smaller than that of TG Pack 2. Considering the data from the test station, TG1 cycled only 73% of the capacity in Ah as did TG Pack 2. However, this did not completely explain the result, as can be seen by comparing Figures 47 and 49. From these figures, it can be seen that cell 1 in TG Pack 1 was degrading faster than cell 5 in TG Pack 2, despite lower Ah throughput. By around cycle 700, TG Pack cell 1 had already degraded below 1.36 Ah of discharge capacity as measured by the standard capacity tests. Meanwhile, cell 5 of TG Pack 2 would not reach 1.38 Ah until cycle 900. Likewise, considering TG Pack 1 cell 5, by cycle 1000, which was equivalent to about cycle 700 of TG Pack 2 in terms of cycled capacity, its capacity was less than 1.4 Ah while TG Pack 2 cell 1 still had a capacity over 1.4 Ah. Therefore, on a per Ah basis, TG pack 1 degraded faster than TG Pack 2.

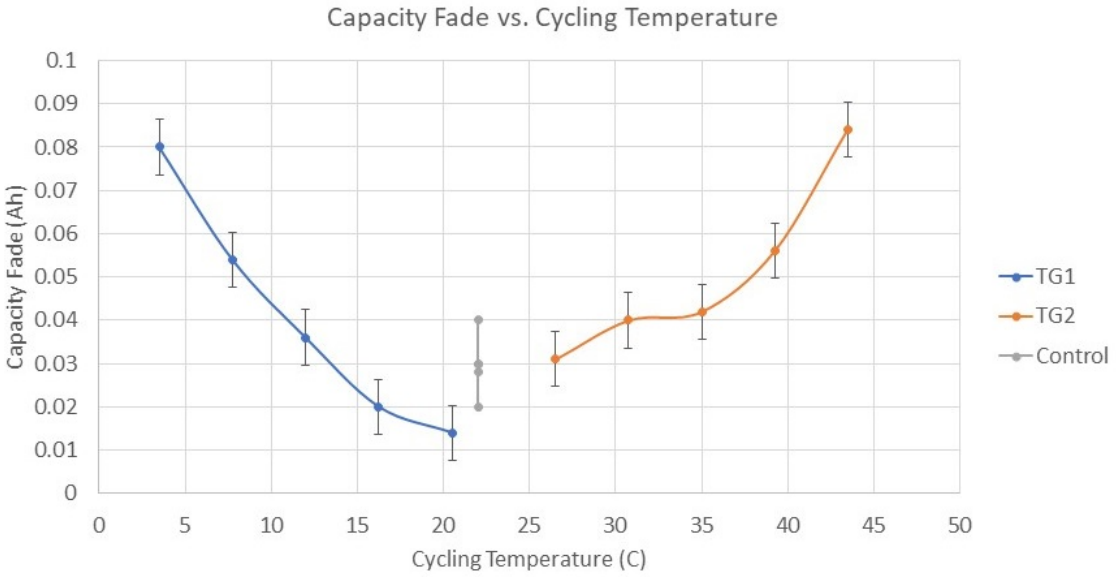

FIGURE 53. Plot of the change in cell capacity vs cycling temperature and the battery pack in which the cell was connected. Error bars for TG Pack 1 and TG Pack 2 were calculated as +/- one standard deviation of the degradation observed by the cells in the control pack.

Few other works have reported similar aging behavior all in one study. Many works assume degradation only increases with increasing temperature, while most others focus exclusively on a low temperature region. However, some studies that have considered a wide range of temperatures have reported similar findings to those presented above. Waldmann et. al. [126] independently cycled NMC/LMO cells between $-20°C$ and $70°C$, and demonstrated two unique aging mechanisms for low temperature cell degradation compared to high temperature cell degradation. They found that at $25°C$, the degradation rate of NMC/LMO cells is minimized. Increasing the cell temperature resulted in cathode degradation and SEI layer growth, while lower temperatures resulted in lithium plating on the anode. These degradation mechanisms were equal in magnitude at $0°C$ for the cold cells and $70°C$ for the hot cells, with cells cycled at $-20°C$ degrading significantly faster than those at any other temperature. These temperature ranges suggest, in agreement with the above result, that the colder cells degraded faster than the warmer cells for the considered temperature range. In another study, Ruiz et. al. [251] examined LFP cells in the range from $-20°C$ to $30°C$ and found the optimal temperature to minimize degradation was $5°C$. However, they also noted that charging at lower temperatures had a larger effect on capacity fade than altering the discharge temperature. This was expected as charging at lower temperatures is known to cause lithium plating [166]. The large difference in optimal temperature suggests that these results may be highly specific to the particular cell chemistry. The results presented here for LFP cells agreed more closely with the findings of Waldmann et. al. despite their use of a completely different chemistry while disagreeing with the results obtained by Ruiz et. al. for cells of the same chemistry. These results may also have implications for the design of battery pack thermal management systems, as the allowable temperature ΔT can now be said to be a function of the average temperature of the pack.

To evaluate this, a second-order polynomial curve was fit to the degradation data in Figure 53, with $R^2 = 0.95$ and was given by

$$dAh = 0.0001T^2 - 0.0068T + 0.1016 \tag{44}$$

where dAh is the observed reduction in cell capacity, and T is the cell cycling temperature. This expression is only valid for the number of cycles performed as shown in Figure 53, however, by considering the number of cycles performed by the cells and determining the degradation rate it was adapted to account for cell age.

$$\frac{dSoH}{dCyc} = \frac{Ah_{new} - Ah_{old}}{Cyc} \times \frac{1}{Q_{nom}} \tag{45}$$

Where $dSoH/dCyc$ is the change in SoH of the cell per cycle, Ah_{new} is the capacity of the cell when it was new, Ah_{old} is the capacity of the degraded cell, and Q_{nom} is the nominal capacity of the cell. Note that Equation 45 assumed a linear relationship between cycle number and degradation for a given temperature. As can be seen from Figures 47 and 49, this assumption is only valid for a portion of the cell's life. However, it is common to find linear degradation rates for cells cycled at constant conditions during the majority of their life until they reach the 'aging knee' and begin to die [252]. This effect can be seen in Figure 49 where for cells 5, 4, and 3, their degradation rate increased after being linear between cycles 200 and 800. The degradation rates for all the TG cells was calculated and plotted in the same manner as Figure 53. (This figure was not shown because it looked similar but with a different y-axis.) From this plot, another second-order polynomial fit was obtained

$$\frac{dSoH}{dCyc} = 1.38 \times 10^{-7} T^2 - 6.815 \times 10^{-6} T + 0.00010157 \tag{46}$$

Using this expression, a simple model was developed to evaluate the expected degradation of a battery pack subjected to a wide range of temperature conditions. These ranged from a temperature difference between cells within the pack of $0 - 20°C$, and with average pack temperatures of between $5 - 45°C$. Packs were modeled as having 100 cells with a linear temperature gradient, and the pack was assumed to have completed 1000 cycles. The results are presented in Figure 54 which

shows the effect of operating temperature on the degradation of the pack. Specifically, it considers the degradation of the worst (i.e. the cell that degraded the most due to its cycling temperature), and the difference between the worst cell and the cell that degraded the least. Due to the shape of the plots, the most degraded cell in a pack was always either the hottest or the coldest cell, while the least degraded could be anywhere in the pack, depending on the operating conditions of the pack.

Figure 54A shows a surface plot of the expected maximum degradation of a single cell in the battery pack as a function of the pack's average temperature (x-axis) and of the temperature difference within the pack (y-axis). As expected, the minimum degradation was observed at $25°C$ and with no temperature difference. Interestingly, the plot predicted that the increase in maximum degradation was affected by average temperature exactly twice as much as by temperature difference. This was due to the fact that by changing the pack's average temperature by $1°C$, the hottest or coldest cell's temperature would increase of decrease by $1°C$, respectively. Meanwhile, changing the pack's ΔT by $1°C$ resulted in the hottest or coldest cell's temperatures changing by only $0.5°C$ each in order to maintain the same pack average temperature.

Figure 54B shows the difference in SoH between the most degraded and least degraded cells in a pack as a function of pack average (x-axis) temperature and pack temperature difference (y-axis). This is a measurement of the homogeneity of pack degradation, and an ideal pack would degrade such that all cells lose the same capacity. As expected, for the same temperature ranges as Figure 54A, the maximum SoH difference between the cells in the pack was less than the maximum degradation of the pack by 3%. There was also a wider range of pack average temperatures that resulted in even pack degradation. This was because for low pack ΔT, the cells would then be exposed to the same temperature conditions. While they may degrade faster, they would degrade faster *together*. It is noteworthy that with a pack average temperature of $25°C$, a temperature difference of up to $16°C$ would still result in cells degrading within 1% SoH of each other. This was due to shallow initial slope of the curve in Figure 53 and the fact that the minimum and maximum temperatures would only be $17°C$ and $33°C$ respectively, which are both within the low

degradation range for these (and most) cells.

Figures 54 C and D both show the same data as A and B respectively, but in the form of contour plots. They make more obvious the difference in the characteristics between the maximum degradation and the SoH difference plots. The contours of the Figure 54C are much straighter and parallel than those of Figure 54D. This shows that to maintain consistent cell SoH at higher or lower than ideal average pack temperature, a much tighter range of pack ΔT is allowable. These plots clearly show the operating windows that the packs could be subjected to while keeping their degradation within a specified value. For example, as mentioned earlier, many automakers target a $5°C$ temperature range for their battery packs [17]. For an average pack temperature of $25°C$, this specification may be overkill, but for colder (say, below freezing) temperatures, it can be seen that the pack would be expected to begin to degrade non-uniformly by about 2.5% SoH, but cause total degradation of pack capacity of over 8% SoH. Recall that for a series connected pack, the capacity of the entire pack is limited by the lowest capacity cell in the pack. So despite the fact that the temperature difference could result in cells having SoHs between 92% to 94.5%, the effective pack capacity would be limited to 92%. However, based on these figures then, a $5°C$ range of cell temperatures within the pack would keep cell degradation uniform expect at extreme pack average temperatures since it should not be expected that most packs would operate at or near freezing temperatures for the majority of their life. This makes the trade-off of allowing increased degradation during those times to save costs on the thermal management system reasonable.

However, as discussed above, the effect of temperature on the precise aging rate of the cells is highly dependent on the specific cell being considered. Therefore Equation 45 and Figure 54 could not be used directly to model an EV battery pack composed of different cell types. It is possible that particular cell chemistries could be less sensitive to non-uniform temperatures, which would result in over-engineering of the TMS to meet the $5°C$ temperature difference target. However, as a qualitative guide to other cell types, the data presented here could be used as a basis to design the experiment in terms of examined temperature ranges and ΔTs considered.

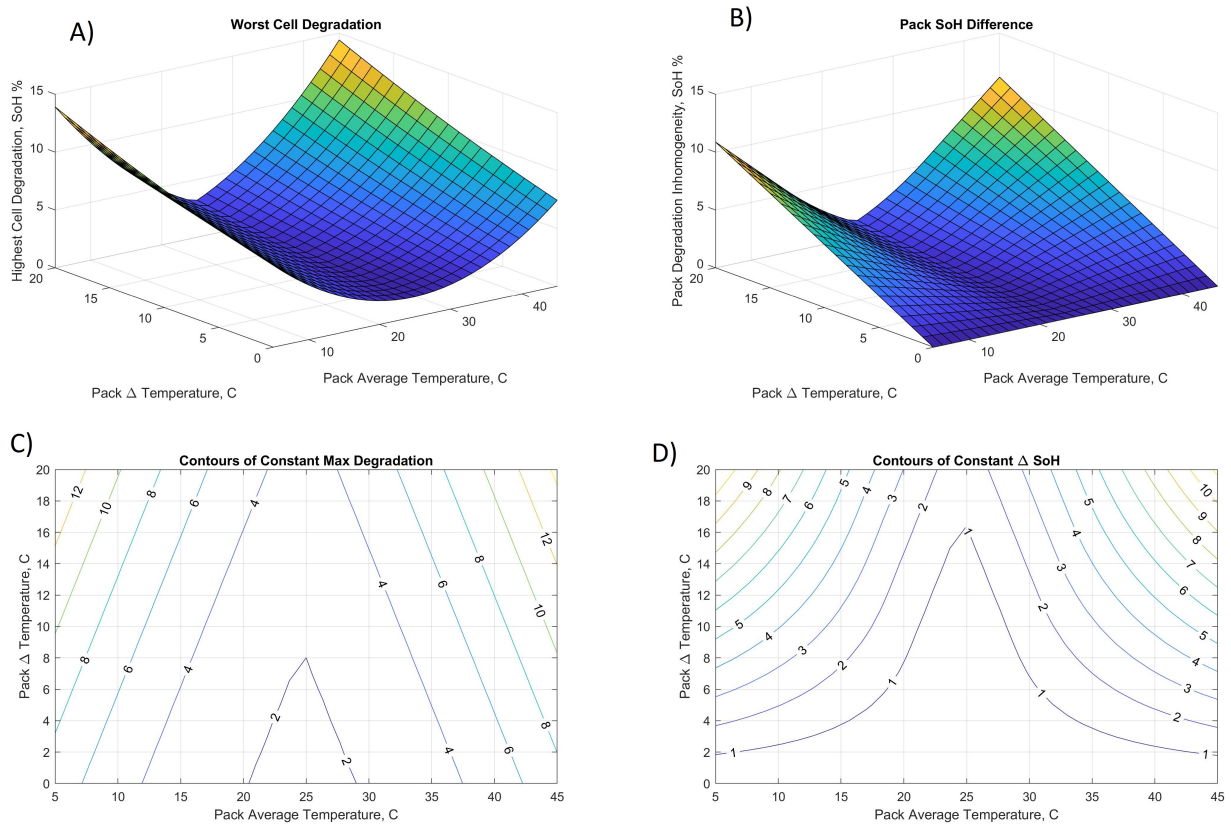

FIGURE 54. A) Surface plot showing the degradation of the most degraded cell in the pack. B) Surface plot showing the difference in SoH between the most and least degraded cells. C) Contour plot showing regions of constant maximum degradation. D) Contour plot showing regions of constant SoH difference within the pack. Units on the contour lines are SoH percentage points.

While the presented degradation model does not account for cycling the same pack at multiple temperature conditions, it is a valuable direction of research to continue. This model could be improved to consider dynamic temperature that changes on a per cycle basis if a temperature profile were known. For example, it could take the temperature history of a region and apply that assuming one cycle per day. Then by considering the per-cycle degradation rate, the total effect of a more realistic operating environment and temperature differences on the battery pack's lifetime and performance could be evaluated. Further development of this model in this direction is left to future work.

Part V

Summary and Conclusion

10 Answers to Key Research Questions

10.1 Attribution of Degradation to Cycling Conditions

Calendar Aging To answer the first question, *What portion of the total degradation of the battery packs was caused by calendar aging, cycling, and non-uniform temperature*, consider Figure 51. From this figure, it can be seen that for a battery pack with a nearly continuous duty cycle (as was the case for the above experiments), calendar aging was negligible for temperatures below around $30°C$. However, above this temperature, calendar aging became the most significant contributor to degradation. In fact, it was found that cells stored at $45°C$ degraded approximately twice as fast (in terms of calendar time) as cells cycled individually at the same temperature. This was attributed primarily to the low cycle count of the calendar aged cells resulting in incomplete initial cell formation. Compared to the degradation of the hottest cell (which was also the most degraded cell) of TG Pack 2, calendar aging was 1.5 times worse.

Cycle Aging Unfortunately, it was not feasible during this research to individually cycle cells at $5°C$ due to lab equipment constraints. Starting at $22°C$, it can be seen from Figure 51 that the series connected pack degraded at the same rate as individually cycled cells. Therefore, without the presence of non-uniform temperatures in the battery pack, a series connected pack will degrade at the same rate as individual cells at the same temperature. This implied that standard cycling degradation mechanisms were responsible for the same degradation in the series connected pack. Considering TG Pack 2 which contained cells between $26.5 - 43.5°C$, it can be seen that the warmest cell degraded faster than the individually cycled cells at the same temperature. The cycling degradation accounted for around 2/3 of the total degradation observed for the hottest cell of TG Pack 2. This in turn implies that the temperature gradient increased the cell's degradation by 50% compared to the individually cycled cells. This was attributed to internal temperature gradients within the cell which caused non-uniform and accelerated aging to the cell. This showed

that even in a series connected pack, a non-uniform temperature can induce the effects observed in parallel connected packs, but on the cell level. This degradation mode was verified by neutron imaging, which showed that the cell with applied temperature gradient aged unevenly internally, while the cell cycled at constant elevated temperature degraded uniformly. Further experiments could work to strengthen this finding. This could be done by developing an updated TGS that could apply a temperature gradient to a battery pack while maintaining a constant temperature for each cell in the pack. This could be achieved by the use of independently controlled TECs and heat sinks for each cell. Alternatively, one cell could be cycled at $45°C$ as cell 62 was done here, and another single cell could be cycled at $45°C$ with an applied $\Delta T = 2.4°C$.

10.2 Comparison to Parallel Cells

The second question, *How does non-uniform temperature affect series-connected packs compared to parallel-connected packs* can be addressed by comparing the results presented here with other works in the literature. Starting with [185], where it was found that lower average temperature increased the effect of temperature gradients on the pack performance for parallel connected cells. In that case, this was due to the rapidly increased cell resistance at lower temperature as can be seen from Figure 36, which caused highly non-uniform current through each cell. This work found similar results in Figure 53, where on a per Ah throughput of the pack basis, the colder pack with a temperature gradient degraded faster than the warmer pack. However, the long-term degradation of the parallel pack, while not studied, should be expected to be worse than for the series pack.

The longer term degradation for the parallel cell case was studied by Yang et. al. [184]. They found by simulation that increasing the temperature difference linearly increased the degradation rate of the pack. This result is different from the series cell case shown in Figure 54A, which shows pack degradation increase with increased temperature difference was not linear. However, the pack SoH difference in Figure 54B showed a nearly linear increase with increased ΔT. They also concluded that the temperature difference for the parallel pack did not significantly reduce the pack's usable capacity, because the current load was dynamically distributed between all the cells. This was not the case for series connected cells, since the most degraded cell in the pack resulted

in limiting the charge and discharge cutoffs of the entire pack. In the long term, the parallel pack may experience worse degradation in the sense that each cell experiences high current as the current distribution between the cells changes [69, 195]. This results in increased degradation stresses. Meanwhile, for the series-connected pack, only the coldest (or hottest) cells experience increased degradation, and their decreased performance results in a lower DoD for the remainder of the cells in the pack which reduces their degradation. Therefore, a series pack may only require a few cells to be replaced, while a parallel pack may require the entire pack to be replaced as a result of non-uniform temperatures.

10.3 Non-Uniform Temperature's Effect on Degradation Rate

The third question, *How does the temperature gradient affect the aging rate of the battery pack?* can be addressed by considering Figure 53. Due to the fact that a series connected pack is limited by it's lowest capacity cell, the hottest or coldest cell in the pack will dictate the degradation of the entire pack. In the case of TG Pack 1, cell 1 which was the coldest cell degraded the fastest, while in TG Pack 2, cell 5 (the hottest cell) degraded the fastest. These two cells then became the limiting cells for each pack, reducing the pack's capacity to match their own. For TG Pack 1 cell 1, the cold cell's maintained lower temperature caused increased lithium plating during the charging process. This limited capacity meant the remainder of the cells in TG Pack 1 saw reduced cycle DoD due to both the higher resistance and lower capacity of cell 1. Figure 54A shows the degradation of the most degraded cell in the pack. Keeping in mind the limitation of series connected cells which limits the pack's capacity to the lowest capacity cell, this plot shows the effect of non-uniform temperature on the usable capacity of the pack despite the fact that most of the cells in the pack had significantly higher capacity.

A similar explanation is valid for a series connected pack with a non-uniform temperature difference such that some of the cells are much hotter than the rest (TG Pack 2). However, in this case the hotter cells have lower resistance, and thus do not immediately result in reduced pack capacity. But over time, the increased temperature increases the degradation rate of the cell, and the hotter cells then have a lower capacity than the cooler cells. Again, due to the series-connection, the

reduced capacity of the hot cell limits the total capacity of the entire pack as shown in Figure 54.

10.4 Non-Uniform Temperature's Effect on Pack Performance

The fourth question, *How does the temperature gradient affect the performance of a series-connected pack* is similar to the question of degradation, but on the per-cycle level as opposed to long-term. The performance impact of applying a non-uniform temperature to a series connected battery pack can be seen by comparing Figure 50 with Figures 45 and 48. In Figure 50, the control pack shows the performance that would be expected of a battery pack if no non-uniform temperature existed. Compared to the other two figures, the voltage spread of the cells was much smaller, which indicates efficient use of the full capacity of the pack. On the other hand, for both of the TG packs, it can be seen that the spread of the cell voltages was much larger, especially after 1000 cycles. This indicates that the operating voltage of the pack is being reduced by higher resistance cells, which reduces the maximum power output of the battery pack. For example, considering TG Pack 1, the coldest cell had a resistance of $164.0 \pm 13.8 m\Omega$ while the warmest cell's resistance was only $84.5 \pm 3.3 m\Omega$ at 50% SoC. These resistance values come from the internal resistance vs. temperature data in Figure 33.

To calculate the effect this ΔIR has on the pack's performance, Ohm's Law can be applied. Considering the cell's OCV near 50% SoC during discharge of 3.28V as obtained from the results of the Capacity Characterization Test, and the minimum cell voltage of 2.5V, the maximum possible current to extract from the cell is the current which causes a voltage drop such that the cell operates at 2.5V. In this case, $\Delta V = 0.78V$. Then using Ohm's Law with $R = 70m\Omega$ and $R = 170m\Omega$ shows that the maximum current capacity of the cell was reduced from 8.2A to 4.6A. If even only a single cell is at a low temperature, the entire pack's maximum output current will be limited in this manner.

For a temperature difference with some of the cells at higher temperatures, the overall resistance of the battery pack is reduced, resulting in an increased pack operating voltage. However, if even a single cell is left at ambient temperature, the maximum current the pack can provide will not be changed. Considering that the internal resistance change from $25 - 45°C$ was only $20m\Omega$, the

maximum current gain of the pack would at most be to increase from 8.7-11.1A if all cells were to be heated to $45°C$. This increased temperature would then increase the degradation rate of the cells, as discussed above.

10.5 Effect of Average Pack Temperature

The fifth question, *How does the pack average temperature change the effect of the non-uniform temperature?*, was addressed in section 9.5. For pack capacity fade, it was found that moving the pack average temperature away from $25°C$ in either direction induces additional pack degradation, as can be seen in Figure 54. In terms of pack degradation, if the pack average temperature was above $25°C$, the hottest cell in the pack was measured and predicted to degrade faster than other cells in the pack. If the pack average temperature was below $25°C$, the coldest cell in the pack was measured and predicted to degrade faster than the other cells in the pack. The larger the deviation from $25°C$, and the larger the ΔT, the higher the degradation of pack capacity. The degradation can be calculated from Equation 46.

It was also determined that the degradation mechanisms for packs with non-uniform temperatures above and below $25°C$ were different. For packs below $25°C$, lithium plating during charging was determined to be the primary degradation mechanism. Since lithium-plating is promoted more at lower temperatures, this explained the increased degradation for the lower temperature cells as seen in Figure 53 where TG pack 1 cell 1 lost 5 times the capacity of TG pack 1 cell 5. At temperatures above $25°C$, the primary degradation mechanism was loss of active lithium due to the increased rate of parasitic side reactions which form the SEI layer. Since these reactions have more favorable reaction kinetics at increased temperature, the hottest cell in the packs above $25°C$ degraded just under 3 times faster than the coldest cell in the pack. This was contrary to the observations of the colder pack. The presence of two distinct aging mechanisms for warmer vs. colder cells was confirmed by comparison of the activation energies of the Arrhenius fits to the degradation for each battery pack, as seen in Figures 47 and 49 which where found to be 63 kJ/mol and -60 kJ/mol respectively.

In terms of pack performance (operating voltage/maximum current), lower pack average temperatures were found to more adversely affect pack internal resistance, as can be seen from Figure 33. Increased pack and cell resistance lowered the maximum power capability of the pack, as discussed above. This reduction was more significant for TG Pack 1 than for TG Pack 2. In fact, for TG Pack 2, the performance of the battery pack was not reduced until sufficient cycles had been completed for the hot cell to begin to lose capacity more rapidly than the rest of the cells in the pack and even then, not until the pack SoC was below 5%. Above this SoC, the increased temperature of the hottest cell was still sufficient to counterbalance its increased degradation. Therefore, in agreement with the literature on parallel connected cells with non-uniform temperature, lower average temperatures were found to have greater adverse effects on the battery pack than increased average pack temperatures [69, 185].

10.6 Power Capability Compared to Single Cells

Question six, *How does the temperature gradient affect power capability of the pack compared to an individual cell?* was partially addressed in the answer to question 4 above. The answer depends on the temperature of the single coldest cell because each cell's resistance is affected the same by temperature, except that at low temperatures, these cells were found to have a large variation in internal resistance of 7-10%, compared to their variation at higher temperatures of only 3-4%. Since the cell's resistance directly affects it's voltage drop, and no current greater than the current that would cause the cell's voltage to reach the cutoff voltage is allowable, this reduces the maximum power of the pack by an *additional* 7-10% on top of the change due to temperature. To avoid this increase, cells could be selected based on their low-temperature resistance rather than their $20 - 25°C$ resistance. For single cells, this issue is reduced because each single cell will be able to provide it's full power, but in a series connected pack, even the lowest resistance cell is limited by the highest resistance cell. Since the up to 10% difference in resistance was a $\pm$, it is conceivable that in a many-cell pack at low temperature, 20% of the performance of the lowest resistance cell could be unusable.

In principle a single cell at $45°C$ would have the same resistance as a cell in a temperature gradient pack that was also at $45°C$. For example, if the single cell's temperature was the average temperature of the pack with a temperature gradient, then the maximum current of the battery pack would be lower according to Ohm's Law, Equation 15 and Figure 33 than the single cell's maximum current because some cells in the pack would be colder and have higher resistance than the TG pack. However, for the high temperature pack, this effect would be small compared to a cold pack. Comparing TG packs 1 and 2 for example, consider the $T_{avg-TG1} = 12°C$ and $T_{avg-TG2} = 35°C$. Individual cells at these temperatures would have 10s resistances of $115m\Omega$ and $68m\Omega$, respectively. From 50% SoC as above, this would give maximum current draws of 6.8 A and 11.5 A, respectively. However, at the same SoC, the coldest cell in TG pack 1 would have a resistance of $180m\Omega$ and a maximum current of only 4.3A. The coldest cell in TG pack 2 would have a resistance of $70m\Omega$ and a maximum current of 11.1 A. Therefore, it can be seen that in TG pack 1, the coldest cell limited the average cell's maximum current by 2.5A (37%!) In TG pack 2, the coldest cell limited the average cell by only 0.4A (3%).

10.7 Aging Mechanisms for Non-Uniform Temperature Packs

Given the result shown in Figure 51, question seven *Which aging mechanisms are made worse by non-uniform battery pack temperature* becomes especially relevant. Specifically, the fact that the hot cell in TG Pack 2 degraded $50\% \pm 31\%$ more than the individually cycled cells at $45°C$ showed that some degradation mechanism was aggravated by cycling of the cell within a battery pack with applied temperature gradient. While a large measurement error was observed here, the result was still clear, but more experiments for refinement are required. This degradation was shown to be caused by internal temperature gradients induced in the cell as a result of the pack's temperature gradient. This internal temperature gradient resulted in non-uniform current densities within the cell, which lead to uneven aging as shown by the neutron absorption intensity change across the cell of 5%. This was in addition to the difference in degradation expected due to the difference in temperatures in the various regions within the cell.

11 Summary of Other Key Results

In an effort to make the results of this research as practical to battery pack designers as possible, a summary of important implications of thermal gradients on battery pack degradation is presented here. These conclusions were drawn from an analysis of Figure 54. Firstly, the effect of increasing the difference between $25°C$ and the pack average temperature resulted in twice as much degradation as increasing the temperature difference by the same amount. The implication of this finding is that it is advantageous to run the battery pack's TMS and induce a temperature gradient if it keeps the pack's average temperature closer to $25°C$. This is a fortunate result, because if it were the reverse, the TMS could potentially be the cause of more degradation than it prevented. However, if the TMS generates too large a ΔT within the pack, and the pack regularly operates under such extreme conditions, the pack should be expected to degrade faster. This would be a situation where a more effective TMS design may be required.

The existence of non-uniform temperature in a battery pack always resulted in uneven and increased degradation rate of the cells within the pack. There was no average temperature for which the effect was 0. However, with $T_{avg} = 25°C$, the effect was minimized. In fact, considering the difference in aging between the most and least degraded cells due to this effect, keeping $T_{avg} = 25°C$ would result in such a small difference in degradation between the cells that cell manufacturing variations would likely have a larger effect even with substantial ΔTs.

The effect of ΔT on the degradation of the hottest or coldest cell in the pack is second-order. There is therefore a critical point at around $\Delta T = 8°C$ and $T_{avg} = 12$ or $37°C$ where increasing ΔT significantly increases the degradation of the hottest or coldest cell in the pack and increases the unevenness of the degradation of the cells within the pack.

The increased degradation caused by ΔT was observed to be approximately equal at high and low pack T_{avg}. This was contrary to many degradation models in the literature that model increased degradation only with increased temperature. However, it was not unprecedented in experimental works, but was still not a common feature of degradation and thermal management discussions. Pack designers would do well to be fully aware of the optimal temperature for the specific cell

with which they are working, as it has also been shown that the temperature of minimum aging is highly chemistry dependent.

Pack degradation consistency, i.e. homogeneous pack degradation was found to be easier to achieve than pack degradation minimization. This can be seen by comparing Figure 54C with D. With no ΔT, the pack can degrade rapidly at high or low temperature, but all cells are expected to degrade similarly. For some applications with relatively short life, it may be important to ensure maximum energy density is extratable from the pack more than maximizing pack lifetime. This could be achieved by keeping degradation similar between all the cells as no single cell would limit the charge or discharge. In this case, Figure 54C shows that a much wider range of average temperatures and temperature difference is available. This allows for a cheaper, simpler, and lighter TMS design which are all highly valuable traits in applications such as drone batteries.

As a real-world example of the implications of temperature gradients, the operating window of a Nissan Leaf battery pack was reverse-engineered. The battery pack was removed from a 2013 Nissan Leaf. This battery pack contained 48 modules, each of which contained 4 cells in a 2S2P configuration. These modules are shown in Figure 6d. Henceforth with regard to the Leaf modules, "1 cell" refers to the two cells in parallel in the module. The nominal capacity of thees cells was 66Ah, and the SoH was measured by cycling between 2.5 and 4.15 V at C/2 with a CV charge current cut off of C/20 using the 12 channel Arbin tester from Table 4. The testing revealed that the cells had an average SoH of 59.9%, a minimum SoH of 49.9%, and a maximum SoH of 65.1%. Interestingly, the minimum capacity cell was the lowest capacity cell by far, with the next lowest cell's SoH being 56.4%. The ΔSoH of this pack was 14.2%. Considering figure 54, this implies that the pack was operated under highly extreme conditions, as no ΔSoH that large is present on the plot. If we consider the lowest SoH cell to be a fluke, then the $\Delta SoH = 7\%$. This more reasonable cell degradation difference implies that the pack was operated either in the range of $T_{avg} = 5 - 12°C$ or at $T_{avg} = 37 - 45°C$ with $\Delta T = 13 - 20°C$. Note that as previously stated, the values obtained here do not directly apply to cells of different chemistries making this analysis quantitatively invalid, but qualitatively informative. In addition, other factors may have

contributed to the degradation of these cells, because their history was unknown.

12 Conclusion

In this work, the effect of non-uniform temperature of the degradation and performance of series-connected battery packs was experimentally investigated. This effort was especially relevant to electric vehicle battery packs and second-life energy storage systems because they are made from cells with different characteristics that lead to varying heat generation. Additionally, these packs are typically large in a physical sense, meaning they have a large volume to surface area ratio, ensuring that non-uniform temperatures will arise in the pack. Meanwhile, EV battery packs are operated under adverse conditions, and may be subjected to frequent fast charging. By quantifying the aging effect of temperature gradients applied at different average temperatures compared to cells cycled under other conditions, the effect on the pack's degradation and performance was determined.

Three battery packs consisting of 5 series-connected cells each were cycled under different temperature conditions. One battery pack was cycled at $22°C$ as a control. The other two packs were both subjected to linear temperature gradients of $17°C$, one with an average temperature of $12°C$ and the other with an average temperature of $35°C$. These packs were all cycled 1000 times at 1C to evaluate their degradation. In addition, a sample of cells were aged by calendar aging and by being individually cycled at various temperatures. The measured degradation of all cells was then compared at the end of the cycling period.

The calendar aged cells were observed to have a slight gain in capacity when aged at $5°C$ and $22°C$ for 16 months. This increased capacity was attributed to initial electrochemical milling that occurred during the limited capacity checkups. However, the calendar aged cells stored at $45°C$ were found to have degraded more than any other tested cell. This was also attributed to cell formation, but at higher storage temperature, the increased surface area simply provided increased reaction area for additional SEI formation. Additionally, the calendar aged cells were compared to cycled cells, but the cycled cells were observed to initially increase their capacity over the first 200

cycles. Therefore the act of cycling the cells gave them a capacity advantage over the cells that were placed in storage.

The individually cycled cells were compared to the series connected packs. The individual cells cycled at $22°C$ were found to degrade in agreement with the control series pack that was cycled at $22°C$. However, when comparing the cells cycled at $45°C$ to the temperature gradient pack that was cycled with an average temperature of $35°C$ and a maximum cell temperature of $43.5°C$, it was discovered that the hottest cell in the series pack had degraded 50% more than the individually cycled cells. This increased degradation was attributed to internal temperature inhomogeneities, which both caused non-uniform current distributions within the cell, but also resulted in different side reaction rates across the cell.

The results from the series connected cells with an applied temperature gradient showed that cell degradation increased with both increasing temperature and with decreasing temperature and that degradation was approximately equal with lower temperatures as with higher temperatures. The results of the experiment were used to generate a simple model that revealed that non-uniform temperatures affect pack degradation half as much as changes in pack average temperature. The model also provided a method for battery pack designers to optimize their thermal management system by selection of acceptable operating temperature parameters for their pack. An example application of the model to a Nissan Leaf battery pack revealed that the lack of thermal management in the Leaf's battery pack contributed to large temperature and SoH variations within the battery pack.

REFERENCES

[1] An, S. J., Li, J., Daniel, C., Mohanty, D., Nagpure, S., and Wood III, D. L., 2016. "The state of understanding of the lithium-ion-battery graphite solid electrolyte interphase (sei) and its relationship to formation cycling". *Carbon,* ***105***, pp. 52–76.

[2] U.S. Department of Energy, 2017. Maps and data - u.s. plug-in electric vehicle sales by model. Data retrieved from DoE on 2019-09-25 from *https://afdc.energy.gov/data/10567*.

[3] USABC, 2018. Development of thermal management system for lithium-ion batteries used in vehicle applications. Tech. rep., United States Advanced Battery Consortium LLC. Accessed online on 10/8/2019 from `https://www.uscar.org/guest/article_view.php?articles_id=87`.

[4] Tennessen, P. T., Weintraub, J. C., and Hermann, W. A., 2014. Extruded and ribbed thermal interface for use with a battery cooling system, June 24. US Patent 8,758,924.

[5] California Independent System Operator, 2019. Today's outlook. Retrieved 2019-09-30 from `http://www.caiso.com/TodaysOutlook/Pages/default.aspx`.

[6] Gewald, T., Candussio, A., Wildfeuer, L., Lehmkuhl, D., Hahn, A., and Lienkamp, M., 2020. "Accelerated aging characterization of lithium-ion cells: Using sensitivity analysis to identify the stress factors relevant to cyclic aging". *Batteries,* ***6***(1), p. 6.

[7] Merla, Y., Wu, B., Yufit, V., Brandon, N. P., Martinez-Botas, R. F., and Offer, G. J., 2016. "Novel application of differential thermal voltammetry as an in-depth state-of-health diagnosis method for lithium-ion batteries". *Journal of Power Sources,* ***307***, pp. 308–319.

[8] Vetter, J., Novák, P., Wagner, M., Veit, C., Möller, K.-C., Besenhard, J., Winter, M., Wohlfahrt-Mehrens, M., Vogler, C., and Hammouche, A., 2005. "Ageing mechanisms in lithium-ion batteries". *Journal of power sources,* ***147***(1-2), pp. 269–281.

[9] Jiang, J., and Zhang, C., 2015. *Fundamentals and applications of Lithium-Ion batteries in electric drive vehicles*. John Wiley & Sons.

[10] Rui, X., Jin, Y., Feng, X., Zhang, L., and Chen, C., 2011. "A comparative study on the low-temperature performance of lifepo4/c and li3v2 (po4) 3/c cathodes for lithium-ion batteries". *Journal of Power Sources,* ***196***(4), pp. 2109–2114.

[11] Bilheux, H. Z., McGreevy, R., and Anderson, I. S., 2009. *Neutron Imaging and Applications: A Reference for the Imaging Community*. Springer.

[12] Kam, K. C., and Doeff, M. M., 2012. Electrode materials for lithium ion batteries.

[13] Gilbert, T., Kirss, R., Foster, N., and Davies, G., 2011. *Chemistry*, 3 ed. W. W. Norton & Company, 500 Fifth Ave, New York, NY 10110.

[14] Corp, A. P. P., 2019. Lfp-18650ht specification sheet. Retrieved 2020-03-12 from `https://www.batteryspace.com/prod-specs/9736-LFP-18650HT.pdf`.

[15] Fleckenstein, M., Bohlen, O., Roscher, M. A., and Bäker, B., 2011. "Current density and state of charge inhomogeneities in li-ion battery cells with lifepo4 as cathode material due to temperature gradients". *Journal of Power Sources,* ***196***(10), pp. 4769–4778.

[16] Huang, J., Li, Z., Liaw, B. Y., Wang, Z., Song, S., Wu, N., and Zhang, J., 2015. "Entropy coefficient of a blended electrode in a lithium-ion cell". *Journal of The Electrochemical Society,* ***162***(12), pp. A2367–A2371.

[17] Klein, M., and Park, J., 2017. "Current distribution measurements in parallel-connected lithium-ion cylindrical cells under non-uniform temperature conditions". *Journal of The Electrochemical Society,* ***164***(9), pp. A1893–A1906.

[18] Bowley, R., and Sanchez, M., 1999. *Introductory Statistical Mechanics*, 2 ed. Oxford Science Publications, Great Clarendon St, Oxford OX2 6DP.

[19] von Srbik, M.-T., Marinescu, M., Martinez-Botas, R. F., and Offer, G. J., 2016. "A physically meaningful equivalent circuit network model of a lithium-ion battery accounting for local electrochemical and thermal behaviour, variable double layer capacitance and degradation". *Journal of Power Sources,* ***325***, pp. 171–184.

[20] Osswald, P. J., Erhard, S. V., Noel, A., Keil, P., Kindermann, F. M., Hoster, H., and Jossen, A., 2016. "Current density distribution in cylindrical li-ion cells during impedance measurements". *Journal of Power Sources,* ***314***, pp. 93–101.

[21] Curry, C., 2017. Lithium-ion battery costs and market. Report, Bloomberg New Energy Finance.

[22] Chen, S., Wan, C., and Wang, Y., 2005. "Thermal analysis of lithium-ion batteries". *Journal of Power Sources,* ***140***(1), pp. 111–124.

[23] Torchio, M., Magni, L., Gopaluni, R. B., Braatz, R. D., and Raimondo, D. M., 2016. "Lionsimba: A matlab framework based on a finite volume model suitable for li-ion battery design, simulation, and control". *Journal of The Electrochemical Society,* ***163***(7), pp. A1192–A1205.

[24] Chen, Y., and Evans, J. W., 1993. "Heat transfer phenomena in lithium/polymer-electrolyte batteries for electric vehicle application". *Journal of the Electrochemical Society,* ***140***(7), pp. 1833–1838.

[25] Li, S., Pischinger, S., He, C., Liang, L., and Stapelbroek, M., 2018. "A comparative study of model-based capacity estimation algorithms in dual estimation frameworks for lithium-ion batteries under an accelerated aging test". *Applied energy,* ***212***, pp. 1522–1536.

[26] Stroe, D.-I., Świerczyński, M., Stan, A.-I., Teodorescu, R., and Andreasen, S. J., 2014. "Accelerated lifetime testing methodology for lifetime estimation of lithium-ion batteries used in augmented wind power plants". *IEEE Transactions on Industry Applications,* ***50***(6), pp. 4006–4017.

[27] Edelstein, S., 2012. Nissan leaf owners in arizona say heat is destroying their cars' batteries. Report, Digital Trends.

[28] Voelcker, J., 2013. Nissan tests new heat-resistant battery for leaf electric car. Report, Green Car Reports.

[29] Waldmann, T., Bisle, G., Hogg, B.-I., Stumpp, S., Danzer, M. A., Kasper, M., Axmann, P., and Wohlfahrt-Mehrens, M., 2015. "Influence of cell design on temperatures and temperature gradients in lithium-ion cells: an in operando study". *Journal of The Electrochemical Society,* ***162***(6), pp. A921–A927.

[30] Sabbah, R., Kizilel, R., Selman, J., and Al-Hallaj, S., 2008. "Active (air-cooled) vs. passive (phase change material) thermal management of high power lithium-ion packs: Limitation of temperature rise and uniformity of temperature distribution". *Journal of Power Sources,* ***182***(2), pp. 630–638.

[31] Klein, M., Tong, S., and Park, J., 2016. "In-plane nonuniform temperature effects on the performance of a large-format lithium-ion pouch cell". *Applied Energy,* ***165***, pp. 639–647.

[32] Brand, M. J., Hofmann, M. H., Steinhardt, M., Schuster, S. F., and Jossen, A., 2016. "Current distribution within parallel-connected battery cells". *Journal of Power Sources,* ***334***, pp. 202–212.

[33] Chiu, K.-C., Lin, C.-H., Yeh, S.-F., Lin, Y.-H., Huang, C.-S., and Chen, K.-C., 2014. "Cycle life analysis of series connected lithium-ion batteries with temperature difference". *Journal of Power Sources,* ***263***, pp. 75–84.

[34] Levi, M. D., and Aurbach, D., 1997. "The mechanism of lithium intercalation in graphite film electrodes in aprotic media. part 1. high resolution slow scan rate cyclic voltammetric

studies and modeling". *Journal of Electroanalytical Chemistry,* ***421***(1-2), pp. 79–88.
[35] Kalhoff, J., Eshetu, G. G., Bresser, D., and Passerini, S., 2015. "Safer electrolytes for lithium-ion batteries: state of the art and perspectives". *ChemSusChem,* ***8***(13), pp. 2154–2175.
[36] Tarascon, J.-M., and Armand, M., 2011. "Issues and challenges facing rechargeable lithium batteries". In *Materials for Sustainable Energy: A Collection of Peer-Reviewed Research and Review Articles from Nature Publishing Group*. World Scientific, pp. 171–179.
[37] Yang, N., Zhang, X., Li, G., and Hua, D., 2015. "Assessment of the forced air-cooling performance for cylindrical lithium-ion battery packs: A comparative analysis between aligned and staggered cell arrangements". *Applied thermal engineering,* ***80***, pp. 55–65.
[38] Saw, L. H., Ye, Y., and Tay, A. A., 2016. "Integration issues of lithium-ion battery into electric vehicles battery pack". *Journal of Cleaner Production,* ***113***, pp. 1032–1045.
[39] Yuan, X., Liu, H., and Zhang, J., 2011. *Lithium-ion batteries: advanced materials and technologies*. CRC press.
[40] Padhi, A. K., Nanjundaswamy, K. S., and Goodenough, J. B., 1997. "Phospho-olivines as positive-electrode materials for rechargeable lithium batteries". *Journal of the electrochemical society,* ***144***(4), pp. 1188–1194.
[41] Yoshio, M., Brodd, R. J., and Kozawa, A., 2009. *Lithium-ion batteries*, Vol. 1. Springer.
[42] Shearing, P. R., Howard, L. E., Jørgensen, P. S., Brandon, N. P., and Harris, S. J., 2010. "Characterization of the 3-dimensional microstructure of a graphite negative electrode from a li-ion battery". *Electrochemistry communications,* ***12***(3), pp. 374–377.
[43] Müller, M., Pfaffmann, L., Jaiser, S., Baunach, M., Trouillet, V., Scheiba, F., Scharfer, P., Schabel, W., and Bauer, W., 2017. "Investigation of binder distribution in graphite anodes for lithium-ion batteries". *Journal of Power Sources,* ***340***, pp. 1–5.
[44] Takahashi, K., and Srinivasan, V., 2015. "Examination of graphite particle cracking as a failure mode in lithium-ion batteries: a model-experimental study". *Journal of The Electrochemical Society,* ***162***(4), pp. A635–A645.
[45] Fleischhammer, M., Waldmann, T., Bisle, G., Hogg, B.-I., and Wohlfahrt-Mehrens, M., 2015. "Interaction of cyclic ageing at high-rate and low temperatures and safety in lithium-ion batteries". *Journal of Power Sources,* ***274***, pp. 432–439.
[46] Ein-Eli, Y., Markovsky, B., Aurbach, D., Carmeli, Y., Yamin, H., and Luski, S., 1994. "The dependence of the performance of li-c intercalation anodes for li-ion secondary batteries on the electrolyte solution composition". *Electrochimica Acta,* ***39***(17), pp. 2559–2569.
[47] Aravindan, V., Gnanaraj, J., Madhavi, S., and Liu, H.-K., 2011. "Lithium-ion conducting electrolyte salts for lithium batteries". *Chemistry–A European Journal,* ***17***(51), pp. 14326–14346.
[48] Zhang, S. S., 2006. "A review on electrolyte additives for lithium-ion batteries". *Journal of Power Sources,* ***162***(2), pp. 1379–1394.
[49] Agubra, V. A., and Fergus, J. W., 2014. "The formation and stability of the solid electrolyte interface on the graphite anode". *Journal of Power Sources,* ***268***, pp. 153–162.
[50] Schmuch, R., Wagner, R., Hörpel, G., Placke, T., and Winter, M., 2018. "Performance and cost of materials for lithium-based rechargeable automotive batteries". *Nature Energy,* ***3***(4), p. 267.
[51] Davies, D., Verde, M., Mnyshenko, O., Chen, Y., Rajeev, R., Meng, Y., and Elliott, G., 2019. "Combined economic and technological evaluation of battery energy storage for grid applications". *Nature Energy,* ***4***(1), p. 42.
[52] Inc, E. E., 2016. The enphase storage system.

[53] Sonnen, 2019. Introducing energy automation with ecolinx.
[54] Bandhauer, T. M., Garimella, S., and Fuller, T. F., 2011. "A critical review of thermal issues in lithium-ion batteries". *Journal of the Electrochemical Society,* ***158***(3), pp. R1–R25.
[55] AA Portable Power Corp. *Specification Approval Sheet Model 18500.*
[56] Menzinger, M., and Wolfgang, R., 1969. "The meaning and use of the arrhenius activation energy". *Angewandte Chemie International Edition in English,* ***8***(6), pp. 438–444.
[57] Larmine, J., and Dicks, A., 2003. *Fuel Cell Systems Explained*, 2 ed. John Wiley & Sons Ltd, The Atrium, Souther Gate, Chichester, West Sussex PO19 8SQ, England.
[58] Churikov, A. V., Ivanishchev, A. V., Ushakov, A. V., Gamayunova, I. M., and Leenson, I. A., 2013. "Thermodynamics of lifepo4 solid-phase synthesis using iron (ii) oxalate and ammonium dihydrophosphate as precursors". *Journal of Chemical & Engineering Data,* ***58***(6), pp. 1747–1759.
[59] Iyer, R. G., Delacourt, C., Masquelier, C., Tarascon, J.-M., and Navrotsky, A., 2006. "Energetics of lifepo4 and polymorphs of its delithiated form, fepo4". *Electrochemical and solid-state letters,* ***9***(2), pp. A46–A48.
[60] Reynier, Y., Yazami, R., and Fultz, B., 2003. "The entropy and enthalpy of lithium intercalation into graphite". *Journal of power sources,* ***119***, pp. 850–855.
[61] Jalkanen, K., Aho, T., and Vuorilehto, K., 2013. "Entropy change effects on the thermal behavior of a lifepo4/graphite lithium-ion cell at different states of charge". *Journal of Power Sources,* ***243***, pp. 354–360.
[62] Winter, M., and Brodd, R. J., 2004. What are batteries, fuel cells, and supercapacitors?
[63] Sauvage, F., Tarascon, J.-M., and Baudrin, E., 2008. "Insights into the potentiometric response behaviour vs. li+ of lifepo4 thin films in aqueous medium". *Analytica chimica acta,* ***622***(1-2), pp. 163–168.
[64] Prada, E., Di Domenico, D., Creff, Y., Bernard, J., Sauvant-Moynot, V., and Huet, F., 2012. "Simplified electrochemical and thermal model of lifepo4-graphite li-ion batteries for fast charge applications". *Journal of The Electrochemical Society,* ***159***(9), pp. A1508–A1519.
[65] Wu, B., Yufit, V., Marinescu, M., Offer, G. J., Martinez-Botas, R. F., and Brandon, N. P., 2013. "Coupled thermal–electrochemical modelling of uneven heat generation in lithium-ion battery packs". *Journal of Power Sources,* ***243***, pp. 544–554.
[66] Troxler, Y., Wu, B., Marinescu, M., Yufit, V., Patel, Y., Marquis, A. J., Brandon, N. P., and Offer, G. J., 2014. "The effect of thermal gradients on the performance of lithium-ion batteries". *Journal of Power Sources,* ***247***, pp. 1018–1025.
[67] Song, L., and Evans, J. W., 2000. "Electrochemical-thermal model of lithium polymer batteries". *Journal of the Electrochemical Society,* ***147***(6), pp. 2086–2095.
[68] Santhanagopalan, S., Guo, Q., Ramadass, P., and White, R. E., 2006. "Review of models for predicting the cycling performance of lithium ion batteries". *Journal of Power Sources,* ***156***(2), pp. 620–628.
[69] Erhard, S. V., Osswald, P. J., Keil, P., Höffer, E., Haug, M., Noel, A., Wilhelm, J., Rieger, B., Schmidt, K., Kosch, S., et al., 2017. "Simulation and measurement of the current density distribution in lithium-ion batteries by a multi-tab cell approach". *Journal of The Electrochemical Society,* ***164***(1), pp. A6324–A6333.
[70] Wu, B., Yufit, V., Marinescu, M., Offer, G. J., Martinez-Botas, R. F., and Brandon, N. P., 2013. "Coupled thermal–electrochemical modelling of uneven heat generation in lithium-ion battery packs". *Journal of Power Sources,* ***243***, pp. 544–554.
[71] Heubner, C., Schneider, M., and Michaelis, A., 2015. "Investigation of charge transfer kinetics

of li-intercalation in lifepo4". *Journal of Power Sources,* ***288***, pp. 115–120.
[72] Allu, S., Kalnaus, S., Elwasif, W., Simunovic, S., Turner, J. A., and Pannala, S., 2014. "A new open computational framework for highly-resolved coupled three-dimensional multiphysics simulations of li-ion cells". *Journal of Power Sources,* ***246***, pp. 876–886.
[73] Ramadesigan, V., Northrop, P. W., De, S., Santhanagopalan, S., Braatz, R. D., and Subramanian, V. R., 2012. "Modeling and simulation of lithium-ion batteries from a systems engineering perspective". *Journal of The Electrochemical Society,* ***159***(3), pp. R31–R45.
[74] Di Domenico, D., Stefanopoulou, A., and Fiengo, G., 2010. "Lithium-ion battery state of charge and critical surface charge estimation using an electrochemical model-based extended kalman filter". *Journal of dynamic systems, measurement, and control,* ***132***(6).
[75] Cho, H.-M., Choi, W.-S., Go, J.-Y., Bae, S.-E., and Shin, H.-C., 2012. "A study on time-dependent low temperature power performance of a lithium-ion battery". *Journal of Power Sources,* ***198***, pp. 273–280.
[76] Zhang, S., Xu, K., and Jow, T., 2003. "The low temperature performance of li-ion batteries". *Journal of Power Sources,* ***115***(1), pp. 137–140.
[77] Stubbe, R., 2018. Global demand for batteries multiplies. Retrieved 2019-09-25.
[78] Cole, J., 2016. Netherlands moves to only allow ev sales by 2025 - end of gas, petrol. Retrieved 2019-09-25.
[79] Halvorson, B., 2019. Colorado adopts california electric vehicle mandate. Retrieved 2019-09-25.
[80] Office of the Governor of California, 2020. Executive order n-79-20. *https://www.gov.ca.gov/wp-content/uploads/2020/09/9.23.20-EO-N-79-20-Climate.pdf*.
[81] Shahan, Z., 2021. 2020 us electric vehicle sales report. Retrieved 2021-10-25.
[82] Cook, R., 2018. Us auto sales rise as suvs, trucks dominate. Retrieved 2019-09-25.
[83] Hanley, S., 2016. Why are there so few ev & hybrid suvs & crossovers? Retrieved 2019-09-25.
[84] Kane, M., 2018. Bloomberg's latest forecast predicts rapidly falling battery prices. Retrieved 2019-09-27.
[85] Oldham, S., 2019. Looking for an ev? here's every 2019 and 2020 electric car and suv. Retrieved 2019-09-25.
[86] Ingham, J., 2015. New network rail train runs on rechargeable batteries. Retrieved 2019-09-25.
[87] Sebastian, B., 2019. Proterra ready for electric bus battery leasing with $200-million credit facility. Retrieved 2019-09-25.
[88] San Francisco Municipal Transportation Agency , 2018. San francisco commits to all-electric bus fleet by 2035. Retrieved 2019-09-25.
[89] Nelson, L. J., 2017. L.a. metro wants to spend $138 million on electric buses. the goal: An emission-free fleet by 2030. Retrieved 2019-09-25.
[90] Lambert, F., 2017. Seattle is getting a massive fleet of all-electric buses, proterra gets the bulk of the order. Retrieved 2019-09-25.
[91] McKenna, P., 2018. New york city aims for all-electric bus fleet by 2040. Retrieved 2019-09-25.
[92] Proterra, 2019. Revolutionizing transit: The proterra catalyst battery electric bus. Retrieved 2019-09-25.
[93] Haghighi, E. B., and Moghaddam, M., 2018. "Analyzing thermal management methods of li-ion battery modules". In 2018 IEEE International Telecommunications Energy Conference (INTELEC), IEEE, pp. 1–4.

[94] Pistoia, G., and Liaw, B., 2018. *Behaviour of Lithium-Ion Batteries in Electric Vehicles: Battery Health, Performance, Safety, and Cost*. Springer.
[95] Bower, G. S., and Ritter, K., 2017. 2017 chevy bolt battery cooling and gearbox details. Retrieved 2019-10-07.
[96] Zhu Yulong Automotive Electronics Design, 2018. Potential recall caused by gm bolt battery failure. Tech. rep., Zhu Yulong Automotive Electronics Design, April.
[97] Energy Storage Association, 2019. 35x25 a vision for energy storage. Retrieved 2019-09-27.
[98] , 2018. Us battery storage market trends. Tech. rep., U.S. Energy Information Administration, May.
[99] California Public Utilities Commission, 2016. Energy storage. Retrieved 2019-09-27.
[100] Commission, C. E., 2018. Tracking progress - energy storage. Retrieved 2021-10-25.
[101] Gas, P., and Company, E., 2021. Renewable energy and storage. Retrieved 2021-10-25.
[102] California Public Utilities Commission, 2019. Self-generation incentive program. Retrieved 2019-09-27.
[103] Self-Generation Incentive Program, 2017. Self-generation incentive program handbook. Retrieved 2019-09-27.
[104] California State Assembly, 2010. Assembly bill no. 2514. Accessed on 2019-9-30 from *http://www.leginfo.ca.gov/pub/09-10/bill/asm/ab*$_2$501 − 2550/*ab*$_2$514$_b$*ill*$_2$0100929$_c$*haptered.pdf*, .
[105] California Independent System Operator, 2016. What the duck curve tells us about managing a green grid. Retrieved 2019-09-30 from *https://www.caiso.com/Documents/FlexibleResourcesHelpRenewables*$_F$*astFacts.pdf*.
[106] Lacap, J., Park, J. W., and Beslow, L., 2021. "Development and demonstration of microgrid system utilizing second-life electric vehicle batteries". *Journal of Energy Storage,* ***41***, p. 102837.
[107] Maisch, M., 2019. Lithium-ion recycling rates far higher than some statistics suggest. Retrieved 2019-10-01 from *https://www.pv-magazine.com/2019/07/12/lithium-ion-recycling-rates-far-higher-than-some-statistics-suggest/*.
[108] Kochhar, A., 2018. The lithium-ion battery boom & the need for recycling. Retrieved 2019-10-01 from *https://li-cycle.com/2018/01/30/the-lithium-ion-battery-boom-the-need-for-recycling*.
[109] Gardiner, J., 2017. The rise of electric cars could leave us with a big battery waste problem. Retrieved 2019-10-01 from *https://www.theguardian.com/sustainable-business/2017/aug/10/electric-cars-big-battery-waste-problem-lithium-recycling*.
[110] McMahon, J., 2018. Innovation is making lithium-ion batteries harder to recycle. Retrieved 2019-10-01 from *https://www.forbes.com/sites/jeffmcmahon/2018/07/01/innovation-is-making-lithium-ion-batteries-harder-to-recycle/5edbe404e515*.
[111] Cusenza, M. A., Bobba, S., Ardente, F., Cellura, M., and Di Persio, F., 2019. "Energy and environmental assessment of a traction lithium-ion battery pack for plug-in hybrid electric vehicles". *Journal of cleaner production,* ***215***, pp. 634–649.
[112] Tesla, 2018. Powerpack tesla commercial battery. Tesla provided datasheet 2018-07-16.
[113] Technologies, S. N., 2019. Energy: A batteries second life. Retrieved 2019-10-07 from `http://www.spiersnewtechnologies.com/energy-storage`.
[114] RePurpose Energy, I., 2020. Battery packs. Retrieved 2021-10-26 from `https://www.repurpose.energy/battery-packs`.
[115] Lacap, J., 2017. Uc davis rmi winery microgrid project. Retrieved 2019-10-07 from

http://mae.engr.ucdavis.edu/jwpark/DavisSite/pages/BWF-microgrid.html.

[116] Rugh, J., Pesaran, A., and Smith, K., 2013. Electric vehicle battery thermal issues and thermal management techniques (presentation). Tech. rep., National Renewable Energy Lab.(NREL), Golden, CO (United States). Accessed online on 10/8/2019 from https://digital.library.unt.edu/ark:/67531/metadc831325.

[117] Pesaran, A. A., 2002. "Battery thermal models for hybrid vehicle simulations". *Journal of power sources,* ***110***(2), pp. 377–382.

[118] Broussely, M., Herreyre, S., Biensan, P., Kasztejna, P., Nechev, K., and Staniewicz, R., 2001. "Aging mechanism in li ion cells and calendar life predictions". *Journal of Power Sources,* ***97***, pp. 13–21.

[119] Aurbach, D., Zinigrad, E., Cohen, Y., and Teller, H., 2002. "A short review of failure mechanisms of lithium metal and lithiated graphite anodes in liquid electrolyte solutions". *Solid state ionics,* ***148***(3-4), pp. 405–416.

[120] Bloom, I., Cole, B., Sohn, J., Jones, S., Polzin, E., Battaglia, V., Henriksen, G., Motloch, C., Richardson, R., Unkelhaeuser, T., et al., 2001. "An accelerated calendar and cycle life study of li-ion cells". *Journal of Power Sources,* ***101***(2), pp. 238–247.

[121] Kassem, M., Bernard, J., Revel, R., Pelissier, S., Duclaud, F., and Delacourt, C., 2012. "Calendar aging of a graphite/lifepo4 cell". *Journal of Power Sources,* ***208***, pp. 296–305.

[122] Naumann, M., Schimpe, M., Keil, P., Hesse, H. C., and Jossen, A., 2018. "Analysis and modeling of calendar aging of a commercial lifepo4/graphite cell". *Journal of Energy Storage,* ***17***, pp. 153–169.

[123] Stiaszny, B., Ziegler, J. C., Krauß, E. E., Zhang, M., Schmidt, J. P., and Ivers-Tiffée, E., 2014. "Electrochemical characterization and post-mortem analysis of aged limn2o4–nmc/graphite lithium ion batteries part ii: Calendar aging". *Journal of Power Sources,* ***258***, pp. 61–75.

[124] Amine, K., Chen, C., Liu, J., Hammond, M., Jansen, A., Dees, D., Bloom, I., Vissers, D., and Henriksen, G., 2001. "Factors responsible for impedance rise in high power lithium ion batteries". *Journal of power sources,* ***97***, pp. 684–687.

[125] Waldmann, T., Gorse, S., Samtleben, T., Schneider, G., Knoblauch, V., and Wohlfahrt-Mehrens, M., 2014. "A mechanical aging mechanism in lithium-ion batteries". *Journal of The Electrochemical Society,* ***161***(10), pp. A1742–A1747.

[126] Waldmann, T., Wilka, M., Kasper, M., Fleischhammer, M., and Wohlfahrt-Mehrens, M., 2014. "Temperature dependent ageing mechanisms in lithium-ion batteries–a post-mortem study". *Journal of Power Sources,* ***262***, pp. 129–135.

[127] Purewal, J., Wang, J., Graetz, J., Soukiazian, S., Tataria, H., and Verbrugge, M. W., 2014. "Degradation of lithium ion batteries employing graphite negatives and nickel–cobalt–manganese oxide+ spinel manganese oxide positives: Part 2, chemical–mechanical degradation model". *Journal of power sources,* ***272***, pp. 1154–1161.

[128] Yoshida, T., Takahashi, M., Morikawa, S., Ihara, C., Katsukawa, H., Shiratsuchi, T., and Yamaki, J.-i., 2006. "Degradation mechanism and life prediction of lithium-ion batteries". *Journal of The Electrochemical Society,* ***153***(3), pp. A576–A582.

[129] Lee, J. T., Nitta, N., Benson, J., Magasinski, A., Fuller, T. F., and Yushin, G., 2013. "Comparative study of the solid electrolyte interphase on graphite in full li-ion battery cells using x-ray photoelectron spectroscopy, secondary ion mass spectrometry, and electron microscopy". *Carbon,* ***52***, pp. 388–397.

[130] Schuster, S. F., Bach, T., Fleder, E., Müller, J., Brand, M., Sextl, G., and Jossen, A., 2015. "Nonlinear aging characteristics of lithium-ion cells under different operational conditions".

Journal of Energy Storage, ***1***, pp. 44–53.

[131] Frisco, S., Kumar, A., Whitacre, J. F., and Litster, S., 2016. "Understanding li-ion battery anode degradation and pore morphological changes through nano-resolution x-ray computed tomography". *Journal of The Electrochemical Society,* ***163***(13), p. A2636.

[132] Broussely, M., Biensan, P., Bonhomme, F., Blanchard, P., Herreyre, S., Nechev, K., and Staniewicz, R., 2005. "Main aging mechanisms in li ion batteries". *Journal of power sources,* ***146***(1-2), pp. 90–96.

[133] Yang, X.-G., Leng, Y., Zhang, G., Ge, S., and Wang, C.-Y., 2017. "Modeling of lithium plating induced aging of lithium-ion batteries: Transition from linear to nonlinear aging". *Journal of Power Sources,* ***360***, pp. 28–40.

[134] Xu, B., Oudalov, A., Ulbig, A., Andersson, G., and Kirschen, D. S., 2016. "Modeling of lithium-ion battery degradation for cell life assessment". *IEEE Transactions on Smart Grid,* ***9***(2), pp. 1131–1140.

[135] Pesaran, A., Ban, C., Dillon, A., Gonder, J., Ireland, J., Keyser, M., Kim, G.-H., Lee, K.-J., Long, D., Neubauer, J., et al., 2012. Fy2011 annual report for nrel energy storage projects. Tech. rep., National Renewable Energy Lab.(NREL), Golden, CO (United States).

[136] Smith, K., Warleywine, M., Wood, E., Neubauer, J., and Pesaran, A., 2012. Comparison of plug-in hybrid electric vehicle battery life across geographies and drive-cycles. Tech. rep., National Renewable Energy Lab.(NREL), Golden, CO (United States).

[137] Waag, W., Fleischer, C., and Sauer, D. U., 2014. "Critical review of the methods for monitoring of lithium-ion batteries in electric and hybrid vehicles". *Journal of Power Sources,* ***258***, pp. 321–339.

[138] Yang, F., Wang, D., Zhao, Y., Tsui, K.-L., and Bae, S. J., 2018. "A study of the relationship between coulombic efficiency and capacity degradation of commercial lithium-ion batteries". *Energy,* ***145***, pp. 486–495.

[139] Smith, A., Burns, J., and Dahn, J., 2010. "A high precision study of the coulombic efficiency of li-ion batteries". *Electrochemical and Solid-State Letters,* ***13***(12), pp. A177–A179.

[140] Madani, S. S., Schaltz, E., and Knudsen Kær, S., 2019. "Effect of current rate and prior cycling on the coulombic efficiency of a lithium-ion battery". *Batteries,* ***5***(3), p. 57.

[141] Xie, J., Ma, J., and Bai, K., 2018. "Enhanced coulomb counting method for state-of-charge estimation of lithium-ion batteries based on peukert's law and coulombic efficiency". *Journal of Power Electronics,* ***18***(3), pp. 910–922.

[142] Bryant, M. D., 2014. "Modeling degradation using thermodynamic entropy". In Proceedings of the 2014 IEEE Conference on Prognostics and Health Management, Cheney, WA, USA, Citeseer, pp. 22–25.

[143] Maher, K., and Yazami, R., 2013. "Effect of overcharge on entropy and enthalpy of lithium-ion batteries". *Electrochimica Acta,* ***101***, pp. 71–78.

[144] Doh, C.-H., Ha, Y.-C., and Eom, S.-w., 2019. "Entropy measurement of a large format lithium ion battery and its application to calculate heat generation". *Electrochimica Acta,* ***309***, pp. 382–391.

[145] Wu, Y., and Jossen, A., 2018. "Entropy-induced temperature variation as a new indicator for state of health estimation of lithium-ion cells". *Electrochimica Acta,* ***276***, pp. 370–376.

[146] Sarasketa-Zabala, E., Aguesse, F., Villarreal, I., Rodriguez-Martinez, L., López, C. M., and Kubiak, P., 2015. "Understanding lithium inventory loss and sudden performance fade in cylindrical cells during cycling with deep-discharge steps". *The Journal of Physical Chemistry C,* ***119***(2), pp. 896–906.

[147] Weng, C., Cui, Y., Sun, J., and Peng, H., 2013. "On-board state of health monitoring of lithium-ion batteries using incremental capacity analysis with support vector regression". *Journal of Power Sources,* ***235***, pp. 36–44.

[148] Dubarry, M., Liaw, B. Y., Chen, M.-S., Chyan, S.-S., Han, K.-C., Sie, W.-T., and Wu, S.-H., 2011. "Identifying battery aging mechanisms in large format li ion cells". *Journal of Power Sources,* ***196***(7), pp. 3420–3425.

[149] Dubarry, M., Truchot, C., and Liaw, B. Y., 2012. "Synthesize battery degradation modes via a diagnostic and prognostic model". *Journal of power sources,* ***219***, pp. 204–216.

[150] Waldmann, T., Gorse, S., Samtleben, T., Schneider, G., Knoblauch, V., and Wohlfahrt-Mehrens, M., 2014. "A mechanical aging mechanism in lithium-ion batteries". *Journal of The Electrochemical Society,* ***161***(10), pp. A1742–A1747.

[151] Xie, Y., Li, J., and Yuan, C., 2014. "Multiphysics modeling of lithium ion battery capacity fading process with solid-electrolyte interphase growth by elementary reaction kinetics". *Journal of Power Sources,* ***248***, pp. 172–179.

[152] Liu, L., Park, J., Lin, X., Sastry, A. M., and Lu, W., 2014. "A thermal-electrochemical model that gives spatial-dependent growth of solid electrolyte interphase in a li-ion battery". *Journal of power sources,* ***268***, pp. 482–490.

[153] An, S. J., Li, J., Daniel, C., Mohanty, D., Nagpure, S., and Wood III, D. L., 2016. "The state of understanding of the lithium-ion-battery graphite solid electrolyte interphase (sei) and its relationship to formation cycling". *Carbon,* ***105***, pp. 52–76.

[154] Ploehn, H. J., Ramadass, P., and White, R. E., 2004. "Solvent diffusion model for aging of lithium-ion battery cells". *Journal of The Electrochemical Society,* ***151***(3), pp. A456–A462.

[155] Wu, B., Yufit, V., Merla, Y., Martinez-Botas, R. F., Brandon, N. P., and Offer, G. J., 2015. "Differential thermal voltammetry for tracking of degradation in lithium-ion batteries". *Journal of Power Sources,* ***273***, pp. 495–501.

[156] Gordon, I. J., Grugeon, S., Takenouti, H., Tribollet, B., Armand, M., Davoisne, C., Débart, A., and Laruelle, S., 2017. "Electrochemical impedance spectroscopy response study of a commercial graphite-based negative electrode for li-ion batteries as function of the cell state of charge and ageing". *Electrochimica Acta,* ***223***, pp. 63–73.

[157] Agubra, V. A., Fergus, J. W., Fu, R., and Choe, S.-Y., 2014. "Analysis of effects of the state of charge on the formation and growth of the deposit layer on graphite electrode of pouch type lithium ion polymer batteries". *Journal of power sources,* ***270***, pp. 213–220.

[158] Michalak, B., Sommer, H., Mannes, D., Kaestner, A., Brezesinski, T., and Janek, J., 2015. "Gas evolution in operating lithium-ion batteries studied in situ by neutron imaging". *Scientific reports,* ***5***, p. 15627.

[159] Bourlot, S., Blanchard, P., and Robert, S., 2011. "Investigation of aging mechanisms of high power li-ion cells used for hybrid electric vehicles". *Journal of Power Sources,* ***196***(16), pp. 6841–6846.

[160] Wang, Q., Sun, J., Yao, X., and Chen, C., 2006. "Thermal behavior of lithiated graphite with electrolyte in lithium-ion batteries". *Journal of The Electrochemical Society,* ***153***(2), pp. A329–A333.

[161] Zheng, Y., Qian, K., Luo, D., Li, Y., Lu, Q., Li, B., He, Y.-B., Wang, X., Li, J., and Kang, F., 2016. "Influence of over-discharge on the lifetime and performance of lifepo 4/graphite batteries". *RSC advances,* ***6***(36), pp. 30474–30483.

[162] Shin, J.-S., Han, C.-H., Jung, U.-H., Lee, S.-I., Kim, H.-J., and Kim, K., 2002. "Effect of li2co3 additive on gas generation in lithium-ion batteries". *Journal of power sources,* ***109***(1),

pp. 47–52.

[163] Lin, H.-P., Chua, D., Salomon, M., Shiao, H., Hendrickson, M., Plichta, E., and Slane, S., 2001. "Low-temperature behavior of li-ion cells". *Electrochemical and Solid-State Letters,* ***4***(6), pp. A71–A73.

[164] Dubarry, M., Truchot, C., Liaw, B. Y., Gering, K., Sazhin, S., Jamison, D., and Michelbacher, C., 2013. "Evaluation of commercial lithium-ion cells based on composite positive electrode for plug-in hybrid electric vehicle applications iii. effect of thermal excursions without prolonged thermal aging". *Journal of the Electrochemical Society,* ***160***(1), pp. A191–A199.

[165] Park, G., Gunawardhana, N., Nakamura, H., Lee, Y.-S., and Yoshio, M., 2012. "The study of electrochemical properties and lithium deposition of graphite at low temperature". *Journal of power sources,* ***199***, pp. 293–299.

[166] Tippmann, S., Walper, D., Balboa, L., Spier, B., and Bessler, W. G., 2014. "Low-temperature charging of lithium-ion cells part i: Electrochemical modeling and experimental investigation of degradation behavior". *Journal of Power Sources,* ***252***, pp. 305–316.

[167] Liu, Q., Du, C., Shen, B., Zuo, P., Cheng, X., Ma, Y., Yin, G., and Gao, Y., 2016. "Understanding undesirable anode lithium plating issues in lithium-ion batteries". *RSC advances,* ***6***(91), pp. 88683–88700.

[168] Same, A., Battaglia, V., Tang, H.-Y., and Park, J. W., 2012. "In situ neutron radiography analysis of graphite/nca lithium-ion battery during overcharge". *Journal of Applied Electrochemistry,* ***42***(1), pp. 1–9.

[169] Jansen, A. N., Dees, D. W., Abraham, D. P., Amine, K., and Henriksen, G. L., 2007. "Low-temperature study of lithium-ion cells using a liysn micro-reference electrode". *Journal of Power Sources,* ***174***(2), pp. 373–379.

[170] Petzl, M., and Danzer, M. A., 2014. "Nondestructive detection, characterization, and quantification of lithium plating in commercial lithium-ion batteries". *Journal of Power Sources,* ***254***, pp. 80–87.

[171] Lee, J. H., Lee, H. M., and Ahn, S., 2003. "Battery dimensional changes occurring during charge/discharge cycles—thin rectangular lithium ion and polymer cells". *Journal of power sources,* ***119***, pp. 833–837.

[172] Zhao, Y., Patel, Y., Hunt, I. A., Kareh, K. M., Holland, A. A., Korte, C., Dear, J. P., Yue, Y., and Offer, G. J., 2017. "Preventing lithium ion battery failure during high temperatures by externally applied compression". *Journal of Energy Storage,* ***13***, pp. 296–303.

[173] Ohzuku, T., Iwakoshi, Y., and Sawai, K., 1993. "Formation of lithium-graphite intercalation compounds in nonaqueous electrolytes and their application as a negative electrode for a lithium ion (shuttlecock) cell". *Journal of The Electrochemical Society,* ***140***(9), p. 2490.

[174] Lewerenz, M., Fuchs, G., Becker, L., and Sauer, D. U., 2018. "Irreversible calendar aging and quantification of the reversible capacity loss caused by anode overhang". *Journal of Energy Storage,* ***18***, pp. 149–159.

[175] Spotnitz, R., and Franklin, J., 2003. "Abuse behavior of high-power, lithium-ion cells". *Journal of power sources,* ***113***(1), pp. 81–100.

[176] Li, G., Xue, R., and Chen, L., 1996. "The influence of polytetrafluorethylene reduction on the capacity loss of the carbon anode for lithium ion batteries". *Solid State Ionics,* ***90***(1-4), pp. 221–225.

[177] Park, H.-K., Kong, B.-S., and Oh, E.-S., 2011. "Effect of high adhesive polyvinyl alcohol binder on the anodes of lithium ion batteries". *Electrochemistry Communications,* ***13***(10), pp. 1051–1053.

[178] Maleki, H., and Howard, J. N., 2006. "Effects of overdischarge on performance and thermal stability of a li-ion cell". *Journal of power sources,* ***160***(2), pp. 1395–1402.

[179] Hendricks, C., Williard, N., Mathew, S., and Pecht, M., 2015. "A failure modes, mechanisms, and effects analysis (fmmea) of lithium-ion batteries". *Journal of Power Sources,* ***297***, pp. 113–120.

[180] Song, H., Cao, Z., Chen, X., Lu, H., Jia, M., Zhang, Z., Lai, Y., Li, J., and Liu, Y., 2013. "Capacity fade of lifepo 4/graphite cell at elevated temperature". *Journal of Solid State Electrochemistry,* ***17***(3), pp. 599–605.

[181] Koltypin, M., Aurbach, D., Nazar, L., and Ellis, B., 2007. "On the stability of lifepo4 olivine cathodes under various conditions (electrolyte solutions, temperatures)". *Electrochemical and Solid-State Letters,* ***10***(2), pp. A40–A44.

[182] Waldmann, T., and Wohlfahrt-Mehrens, M., 2015. "In-operando measurement of temperature gradients in cylindrical lithium-ion cells during high-current discharge". *ECS Electrochemistry Letters,* ***4***(1), pp. A1–A3.

[183] Osswald, P. J., Erhard, S. V., Rheinfeld, A., Rieger, B., Hoster, H. E., and Jossen, A., 2016. "Temperature dependency of state of charge inhomogeneities and their equalization in cylindrical lithium-ion cells". *Journal of Power Sources,* ***329***, pp. 546–552.

[184] Yang, N., Zhang, X., Shang, B., and Li, G., 2016. "Unbalanced discharging and aging due to temperature differences among the cells in a lithium-ion battery pack with parallel combination". *Journal of Power Sources,* ***306***, pp. 733–741.

[185] Klein, M., Tong, S., and Park, J., 2016. "In-plane nonuniform temperature effects on the performance of a large-format lithium-ion pouch cell". *Applied Energy,* ***165***, pp. 639–647.

[186] Bruen, T., and Marco, J., 2016. "Modelling and experimental evaluation of parallel connected lithium ion cells for an electric vehicle battery system". *Journal of Power Sources,* ***310***, pp. 91–101.

[187] Baker, D. R., and Verbrugge, M. W., 1999. "Temperature and current distribution in thin-film batteries". *Journal of the Electrochemical Society,* ***146***(7), pp. 2413–2424.

[188] Zhang, X., 2011. "Thermal analysis of a cylindrical lithium-ion battery". *Electrochimica Acta,* ***56***(3), pp. 1246–1255.

[189] Veth, C., Dragicevic, D., and Merten, C., 2014. "Thermal characterizations of a large-format lithium ion cell focused on high current discharges". *Journal of Power Sources,* ***267***, pp. 760–769.

[190] Robinson, J. B., Darr, J. A., Eastwood, D. S., Hinds, G., Lee, P. D., Shearing, P. R., Taiwo, O. O., and Brett, D. J., 2014. "Non-uniform temperature distribution in li-ion batteries during discharge–a combined thermal imaging, x-ray micro-tomography and electrochemical impedance approach". *Journal of Power Sources,* ***252***, pp. 51–57.

[191] Osswald, P. J., Erhard, S. V., Noel, A., Keil, P., Kindermann, F. M., Hoster, H., and Jossen, A., 2016. "Current density distribution in cylindrical li-ion cells during impedance measurements". *Journal of Power Sources,* ***314***, pp. 93–101.

[192] Erhard, S. V., Osswald, P. J., Wilhelm, J., Rheinfeld, A., Kosch, S., and Jossen, A., 2015. "Simulation and measurement of local potentials of modified commercial cylindrical cells ii: Multi-dimensional modeling and validation". *Journal of The Electrochemical Society,* ***162***(14), pp. A2707–A2719.

[193] Osswald, P. J., Erhard, S. V., Wilhelm, J., Hoster, H. E., and Jossen, A., 2015. "Simulation and measurement of local potentials of modified commercial cylindrical cells i. cell preparation and measurements". *Journal of The Electrochemical Society,* ***162***(10), pp. A2099–A2105.

[194] Zhang, G., Shaffer, C. E., Wang, C.-Y., and Rahn, C. D., 2013. "Effects of non-uniform current distribution on energy density of li-ion cells". *Journal of The Electrochemical Society,* ***160***(11), pp. A2299–A2305.

[195] Zhang, G., Shaffer, C. E., Wang, C.-Y., and Rahn, C. D., 2013. "In-situ measurement of current distribution in a li-ion cell". *Journal of The Electrochemical Society,* ***160***(4), pp. A610–A615.

[196] Kim, G.-H., Smith, K., Lee, K.-J., Santhanagopalan, S., and Pesaran, A., 2011. "Multi-domain modeling of lithium-ion batteries encompassing multi-physics in varied length scales". *Journal of the Electrochemical Society,* ***158***(8), pp. A955–A969.

[197] Lee, K.-J., Smith, K., Pesaran, A., and Kim, G.-H., 2013. "Three dimensional thermal-, electrical-, and electrochemical-coupled model for cylindrical wound large format lithium-ion batteries". *Journal of Power Sources,* ***241***, pp. 20–32.

[198] Bernardi, D. M., and Go, J.-Y., 2011. "Analysis of pulse and relaxation behavior in lithium-ion batteries". *Journal of Power Sources,* ***196***(1), pp. 412–427.

[199] Xu, M., Zhang, Z., Wang, X., Jia, L., and Yang, L., 2014. "Two-dimensional electrochemical–thermal coupled modeling of cylindrical lifepo4 batteries". *Journal of Power Sources,* ***256***, pp. 233–243.

[200] Karimi, G., and Li, X., 2013. "Thermal management of lithium-ion batteries for electric vehicles". *International Journal of Energy Research,* ***37***(1), pp. 13–24.

[201]

[202] Tong, S., Lacap, J. H., and Park, J. W., 2016. "Battery state of charge estimation using a load-classifying neural network". *Journal of Energy Storage,* ***7***, pp. 236–243.

[203] Johansson, C., Bergkvist, M., Geysen, D., De Somer, O., Lavesson, N., and Vanhoudt, D., 2017. "Operational demand forecasting in district heating systems using ensembles of online machine learning algorithms". *Energy Procedia,* ***116***, pp. 208–216.

[204] Hernández, L., Baladrón, C., Aguiar, J. M., Carro, B., Sánchez-Esguevillas, A., and Lloret, J., 2014. "Artificial neural networks for short-term load forecasting in microgrids environment". *Energy,* ***75***, pp. 252–264.

[205] Elkind, E., 2014. "Reuse and repower: How to save money and clean the grid with second-life electric vehicle batteries".

[206] Sun, C., Sun, F., and Moura, S. J., 2015. "Data enabled predictive energy management of a pv-battery smart home nanogrid". In American Control Conference (ACC), 2015, IEEE, pp. 1023–1028.

[207] Saez-de Ibarra, A., Martinez-Laserna, E., Koch-Ciobotaru, C., Rodriguez, P., Stroe, D.-I., and Swierczynski, M., 2015. "Second life battery energy storage system for residential demand response service". In Industrial Technology (ICIT), 2015 IEEE International Conference on, IEEE, pp. 2941–2948.

[208] Jiao, N., and Evans, S., 2016. "Business models for sustainability: the case of second-life electric vehicle batteries". *Procedia CIRP,* ***40***, pp. 250–255.

[209] Casals, L. C., García, B. A., and Benítez, M. M. G., 2017. "Aging model for re-used electric vehicle batteries in second life stationary applications". In *Project Management and Engineering Research*. Springer, pp. 139–151.

[210] Casals, L. C., and Garca, B. A., 2016. "Communications concerns for reused electric vehicle batteries in smart grids". *IEEE Communications Magazine,* ***54***(9), pp. 120–125.

[211] Reid, G., and Julve, J., 2016. "Second life-batteries as flexible storage for renewables energies". *Hg. v. Bundesverband Eneuerbare Energien eV (BEE).*

[212] Casals, L. C., and García, B. A., 2016. "Assessing electric vehicles battery second life remanufacture and management". *Journal of Green Engineering,* ***6***(1), pp. 77–98.

[213] Li, H., Alsolami, M., Yang, S., Alsmadi, Y. M., and Wang, J., 2017. "Lifetime test design for second-use electric vehicle batteries in residential applications". *IEEE Transactions on Sustainable Energy,* ***8***(4), pp. 1736–1746.

[214] Leung, C., 2012. "Pv systems with second life li-ion battery technology". PhD thesis, Murdoch University.

[215] Tong, S., Fung, T., Klein, M. P., Weisbach, D. A., and Park, J. W., 2017. "Demonstration of reusing electric vehicle battery for solar energy storage and demand side management". *Journal of Energy Storage,* ***11***, pp. 200–210.

[216] Liao, Q., Mu, M., Zhao, S., Zhang, L., Jiang, T., Ye, J., Shen, X., and Zhou, G., 2017. "Performance assessment and classification of retired lithium ion battery from electric vehicles for energy storage". *International Journal of Hydrogen Energy,* ***42***(30), pp. 18817–18823.

[217] Telaretti, E., and Dusonchet, L., 2017. "Stationary battery systems in the main world markets: Part 2: Main trends and prospects". In Environment and Electrical Engineering and 2017 IEEE Industrial and Commercial Power Systems Europe (EEEIC/I&CPS Europe), 2017 IEEE International Conference on, IEEE, pp. 1–6.

[218] Deng, J., Shi, J., Liu, Y., and Tang, Y., 2016. "Application of a hybrid energy storage system in the fast charging station of electric vehicles". *IET Generation, Transmission & Distribution,* ***10***(4), pp. 1092–1097.

[219] Ma, T., Wu, S., Wang, F., Lacap, J., Lin, C., Liu, S., Wei, M., Hao, W., Wang, Y., and Park, J. W., 2020. "Degradation mechanism study and safety hazard analysis of overdischarge on commercialized lithium-ion batteries". *ACS Applied Materials & Interfaces,* ***12***(50), pp. 56086–56094.

[220] Marcicki, J., and Yang, X. G., 2014. "Model-based estimation of reversible heat generation in lithium-ion cells". *Journal of The Electrochemical Society,* ***161***(12), pp. A1794–A1800.

[221] Lanz, M., Lehmann, E., Imhof, R., Exnar, I., and Novák, P., 2001. "In situ neutron radiography of lithium-ion batteries during charge/discharge cycling". *Journal of power sources,* ***101***(2), pp. 177–181.

[222] Ivanov, R., Deschamps, A., and De Geuser, F., 2017. "A combined characterization of clusters in naturally aged al–cu–(li, mg) alloys using small-angle neutron and x-ray scattering and atom probe tomography". *Journal of Applied Crystallography,* ***50***(6), pp. 1725–1734.

[223] Santisteban, J. R., Edwards, L., Fizpatrick, M. E., Steuwer, A., and Withers, P. J., 2002. "Engineering applications of bragg-edge neutron transmission". *Applied Physics A,* ***74***(1), pp. s1433–s1436.

[224] Butler, L. G., Schillinger, B., Ham, K., Dobbins, T. A., Liu, P., and Vajo, J. J., 2011. "Neutron imaging of a commercial li-ion battery during discharge: Application of monochromatic imaging and polychromatic dynamic tomography". *Nuclear Instruments and Methods in Physics Research Section A: Accelerators, Spectrometers, Detectors and Associated Equipment,* ***651***(1), pp. 320–328.

[225] University of California, D., 2020. The mcclellan nuclear research center. Retrieved 2020-06-12 from `https://mnrc.ucdavis.edu/`.

[226] Atomics, G., 2020. Triga nuclear reactors. Retrieved 2020-06-12 from `http://www.ga.com/triga/`.

[227] Zheng, H., Li, J., Song, X., Liu, G., and Battaglia, V. S., 2012. "A comprehensive understanding of electrode thickness effects on the electrochemical performances of li-ion battery

cathodes". *Electrochimica Acta,* ***71***, pp. 258–265.

[228] Shi, W., Hu, X., Wang, J., Jiang, J., Zhang, Y., and Yip, T., 2016. "Analysis of thermal aging paths for large-format lifepo4/graphite battery". *Electrochimica acta,* ***196***, pp. 13–23.

[229] Müller, V., Scurtu, R.-G., Memm, M., Danzer, M. A., and Wohlfahrt-Mehrens, M., 2019. "Study of the influence of mechanical pressure on the performance and aging of lithium-ion battery cells". *Journal of Power Sources,* ***440***, p. 227148.

[230] Chang, W., Bommier, C., Mohr, R., and Steingart, D., 2021. "Impact of non-arrhenius temperature behavior on the fast-charging capabilities of licoo2–graphite lithium-ion batteries". *The Journal of Physical Chemistry C,* ***125***(3), pp. 1731–1741.

[231] Gogoana, R., Pinson, M. B., Bazant, M. Z., and Sarma, S. E., 2014. "Internal resistance matching for parallel-connected lithium-ion cells and impacts on battery pack cycle life". *Journal of Power Sources,* ***252***, pp. 8–13.

[232] Strobl, M., Kardjilov, N., Hilger, A., Kühne, G., Frei, G., and Manke, I., 2009. "High-resolution investigations of edge effects in neutron imaging". *Nuclear Instruments and Methods in Physics Research Section A: Accelerators, Spectrometers, Detectors and Associated Equipment,* ***604***(3), pp. 640–645.

[233] Tremsin, A., Morgano, M., Panzner, T., Lehmann, E., Filgers, U., Vallerga, J., McPhate, J., Siegmund, O., and Feller, W., 2015. "High resolution neutron imaging capabilities at boa beamline at paul scherrer institut". *Nuclear Instruments and Methods in Physics Research Section A: Accelerators, Spectrometers, Detectors and Associated Equipment,* ***784***, pp. 486–493.

[234] O'Haver, T., 2018. peakfit.m. Version 9.0.0.0, Retrieved 2019-4-19.

[235] Keil, J., Paul, N., Baran, V., Keil, P., Gilles, R., and Jossen, A., 2019. "Linear and non-linear aging of lithium-ion cells investigated by electrochemical analysis and in-situ neutron diffraction". *Journal of The Electrochemical Society,* ***166***(16), p. A3908.

[236] Dreyer, W., Jamnik, J., Guhlke, C., Huth, R., Moškon, J., and Gaberšček, M., 2010. "The thermodynamic origin of hysteresis in insertion batteries". *Nature materials,* ***9***(5), pp. 448–453.

[237] de Hoog, J., Timmermans, J.-M., Ioan-Stroe, D., Swierczynski, M., Jaguemont, J., Goutam, S., Omar, N., Van Mierlo, J., and Van Den Bossche, P., 2017. "Combined cycling and calendar capacity fade modeling of a nickel-manganese-cobalt oxide cell with real-life profile validation". *Applied Energy,* ***200***, pp. 47–61.

[238] Schmitt, J., Maheshwari, A., Heck, M., Lux, S., and Vetter, M., 2017. "Impedance change and capacity fade of lithium nickel manganese cobalt oxide-based batteries during calendar aging". *Journal of Power Sources,* ***353***, pp. 183–194.

[239] Christensen, J., 2010. "Modeling diffusion-induced stress in li-ion cells with porous electrodes". *Journal of the Electrochemical Society,* ***157***(3), p. A366.

[240] Geisbauer, C., Wöhrl, K., Koch, D., Wilhelm, G., Schneider, G., and Schweiger, H.-G., 2021. "Comparative study on the calendar aging behavior of six different lithium-ion cell chemistries in terms of parameter variation". *Energies,* ***14***(11), p. 3358.

[241] Gyenes, B., Stevens, D., Chevrier, V., and Dahn, J., 2014. "Understanding anomalous behavior in coulombic efficiency measurements on li-ion batteries". *Journal of The Electrochemical Society,* ***162***(3), p. A278.

[242] Lewerenz, M., Münnix, J., Schmalstieg, J., Käbitz, S., Knips, M., and Sauer, D. U., 2017. "Systematic aging of commercial lifepo4— graphite cylindrical cells including a theory explaining rise of capacity during aging". *Journal of power sources,* ***345***, pp. 254–263.

[243] Zhang, G., Wei, X., Han, G., Dai, H., Zhu, J., Wang, X., Tang, X., and Ye, J., 2021. "Lithium plating on the anode for lithium-ion batteries during long-term low temperature cycling". *Journal of Power Sources,* ***484***, p. 229312.

[244] Li, D., Danilov, D. L., Gao, L., Yang, Y., and Notten, P. H., 2016. "Degradation mechanisms of c6/lifepo4 batteries: experimental analyses of cycling-induced aging". *Electrochimica Acta,* ***210***, pp. 445–455.

[245] Lewerenz, M., Münnix, J., Schmalstieg, J., Käbitz, S., Knips, M., and Sauer, D. U., 2017. "Systematic aging of commercial lifepo4— graphite cylindrical cells including a theory explaining rise of capacity during aging". *Journal of power sources,* ***345***, pp. 254–263.

[246] Naumann, M., Spingler, F. B., and Jossen, A., 2020. "Analysis and modeling of cycle aging of a commercial lifepo4/graphite cell". *Journal of Power Sources,* ***451***, p. 227666.

[247] Dubarry, M., Truchot, C., and Liaw, B. Y., 2014. "Cell degradation in commercial lifepo4 cells with high-power and high-energy designs". *Journal of Power Sources,* ***258***, pp. 408–419.

[248] Logan, E., Hebecker, H., Eldesoky, A., Luscombe, A., Johnson, M. B., and Dahn, J., 2020. "Performance and degradation of lifepo4/graphite cells: The impact of water contamination and an evaluation of common electrolyte additives". *Journal of The Electrochemical Society,* ***167***(13), p. 130543.

[249] Dominko, R., Goupil, J., Bele, M., Gaberscek, M., Remskar, M., Hanzel, D., and Jamnik, J., 2005. "Impact of lifepo4/ c composites porosity on their electrochemical performance". *Journal of the Electrochemical Society,* ***152***(5), p. A858.

[250] Zhang, G., Shaffer, C. E., Wang, C.-Y., and Rahn, C. D., 2013. "Effects of non-uniform current distribution on energy density of li-ion cells". *Journal of The Electrochemical Society,* ***160***(11), pp. A2299–A2305.

[251] Ruiz, V. R., Kriston, A., Adanouj, I., Destro, M., Fontana, D., and Pfrang, A., 2018. "The effect of charging and discharging lithium iron phosphate-graphite cells at different temperatures on degradation". *JoVE (Journal of Visualized Experiments)*(137), p. e57501.

[252] Braco, E., San Martín, I., Berrueta, A., Sanchis, P., and Ursúa, A., 2020. "Experimental assessment of cycling ageing of lithium-ion second-life batteries from electric vehicles". *Journal of Energy Storage,* ***32***, p. 101695.